

Degenerate Bogdanov-Takens Bifurcations in Fusion Plasma Models

Daniël Veldman (3413659)

Master's thesis

Coach(es): dr. H.J. de Blank
prof. dr. M.J. Pekker
dr. P.A. Zegeling

Supervisor: prof. dr. Yu.A. Kuznetsov

Utrecht University
Mathematical sciences
Applied Analysis

Utrecht, October, 2015

Contents

I	Introduction	I
1.1	Motivation	1
1.2	Research questions	2
1.3	Outline	3
2	Bifurcation Theory	5
2.1	Concepts	5
2.1.1	Local bifurcations	6
2.1.2	Bifurcations of limit cycles	7
2.2	Different types of bifurcations	8
2.2.1	Codimension 1	8
2.2.2	Codimension 2	12
2.3	Degenerate BT bifurcations	15
2.3.1	The case $b_2 = 0, a_2 \neq 0$	15
2.3.2	The case $a_2 = 0, b_2 \neq 0$	16
2.3.3	The case $a_2 = b_2 = 0$	16
3	Numerical continuation of equilibria in large-scale systems	21
3.1	Continuation algorithm	21
3.1.1	Continuation and detection of singularities	21
3.1.2	Continuation of invariant subspaces (CIS)	22
3.1.3	Implementation in CL_MATCONTL	23
3.2	Bordered systems	25
3.3	Equilibrium and bifurcation curves	29
3.3.1	The equilibrium curve	29
3.3.2	The LP curve	30
3.3.3	The H curve	31
3.3.4	The BT curve	32
4	The PDE system	35
4.1	L–H transition models	35
4.2	Steady-state solutions	38

5	Discretization	41
5.1	Two discretization methods	41
5.1.1	Finite Difference Method	42
5.1.2	Finite Volume Method	43
5.1.3	Comparison	44
5.2	Grid distribution	45
6	Results	47
6.1	Equilibrium solutions	47
6.1.1	1-parameter continuation	47
6.1.2	2-parameter continuation	53
6.1.3	3-parameter continuation	57
6.1.4	Modifications of the model	60
6.2	Periodic solutions	61
6.2.1	Near the degenerate BT bifurcation at $a = -0.01$	61
6.2.2	Far away from the degenerate BT bifurcation at $a = -1$	65
7	Conclusion and outlook	71
7.1	Conclusion	71
7.2	Outlook	73
A	Approximate steady-state solutions	75
B	Discretization	77
B.1	Finite Difference Formulas	77
B.2	Finite Volume Formulas	78
B.3	Leading terms in the local error	78
B.4	Adaptive grid	79
C	Convergence of the spatial discretization	83
C.1	1-parameter continuation	83
C.2	2-parameter continuation	83
C.3	3-parameter continuation	83
	Bibliography	95

Chapter 1

Introduction

The introduction starts with a motivation for the research. After that the research objectives are stated and the outline of the thesis is presented.

1.1 Motivation

Fusion energy production is one of the possible solutions for the worlds energy problem. During a fusion reaction two atomic nuclei collide and form a new type of atomic nucleus. In this process a lot of energy is released. Fusion reactions occur in stars, also in the sun. Fusion energy production on earth requires:

- high temperatures,
- high densities and
- long confinement time.

On earth it is not possible to achieve the same densities as in the sun. For densities that can be achieved at the earth, temperatures need to be over 150,000,000 K, which is ten times higher than the temperature in the core of the sun. At these temperatures the gas becomes a plasma, which means the electrons are separated from the atomic nucleus.

An important indication of the performance of a fusion reactor is the confinement time. The confinement time is defined as the energy content of the plasma divided by the heating power. A long confinement time means that the energy losses are relatively small compared to the energy content of the plasma, which indicates a better performance of the reactor.

The most successful present-day fusion devices are TOKAMAKS. Experiments have shown two modes of operation in TOKAMAKS, which have been named L-mode (Low confinement) and H-mode (High confinement) [24]. In H-mode the turbulent transport of particles and heat is reduced near the edge of the plasma. However, the transport in the bulk of the plasma is the same for L-mode and H-mode. In H-mode the confinement time is typically twice as large as in L-mode. Therefore the H-mode is the preferred operating mode for future fusion energy production. It is therefore important to obtain a better understanding of dynamics related to the H-mode.

Transitions from L-mode to H-mode are observed when increasing the heating power. Three types of transitions have been observed:

- sharp transitions,
- oscillatory transitions and
- smooth transitions.

The sharp transitions are most commonly observed. When the heating power reached a certain threshold value, the profile suddenly changes from L-mode to H-mode. When decreasing the heating power the transition back to L-mode occurs at a lower threshold value (so hysteresis is present). The oscillatory transitions (also called ‘dithering’) have been observed more recently. Also smooth transitions have been observed for which the profile slowly evolves from an L-mode to an H-mode profile, upon a slow increase in heating power.

To obtain a better understanding of these transitions, simplified transport models have been developed. One of the first of these models was proposed by Itoh et al. in [17], and was later extended by Zohm in [27]. This model consisted of three Partial Differential Equations (PDEs) on a one-dimensional spatial domain. The model of Zohm formed also the basis of the work of Weymiens [25] and Paquay [22]. Their simulations showed that these type of models show indeed L-mode and H-mode type solutions and all three observed transitions between them. They also suggested that all three types of transitions could be explained by the presence of a degenerate Bogdanov-Takens (BT) bifurcation (of codimension 3 or 4).

BT bifurcations occur when an equilibrium has two zero eigenvalues of geometric multiplicity 1. At this critical situation there exists (generically) a smooth change of coordinates that brings the restriction to the center-manifold to the form

$$\begin{aligned}\dot{y}_1 &= y_2, \\ \dot{y}_2 &= a_2 y_1^2 + b_2 y_1 y_2 + O(\|y\|^3),\end{aligned}\tag{1.1}$$

where $a_2 b_2 \neq 0$. Based on the observations in [25], we limit ourselves to the following three possible degeneracies,

- $b_2 = 0, a_2 \neq 0$,
- $a_2 = 0, b_2 \neq 0$,
- $a_2 = b_2 = 0$.

In generic systems, the first two degeneracies are of codimension 3. The last one is of codimension 4.

1.2 Research questions

The main question in this thesis is

Does one of these degenerate BT bifurcations occur in the model proposed by Zohm?

This leads to the following sub-questions,

- Which dynamic behavior can be expected near a degenerate BT bifurcation?
- What is an accurate and efficient spatial discretization of the model proposed by Zohm?
- How can degenerate BT bifurcations be detected in this model?

1.3 Outline

The outline of the thesis is as follows. Chapter 2 summarizes some important results in bifurcation theory. Also the dynamics that can be expected near a degenerate BT bifurcation are discussed. Chapter 3 discusses the numerical techniques that are used to study (local) bifurcations in large-scale systems. These techniques have been implemented in `CL_MATCONTL`, which is an extension of `CL_MATCONT` aimed at large-scale systems. Some changes have been made compared to the version of `CL_MATCONTL` in [4]. Chapter 4 introduces the PDE model proposed by Zohm in [27] and gives some properties of the steady-state solutions. In Chapter 5 the spatial discretization for this model is constructed. This discretization is different from the previously developed discretization by Paquay in [22], which could not be used in the context of numerical continuation. Chapter 6 studies the resulting discretization by simulation and the continuation techniques from Chapter 3. The model proposed by Zohm [27] was not studied by numerical continuation before. The thesis ends with a conclusion and an outlook to further research.

Chapter 2

Bifurcation Theory

This chapter is an introduction to the bifurcation theory of a system of ODEs [19, 1]. The chapter is divided in three sections. Section 2.1 provides some general background on bifurcation theory. Section 2.2 will discuss particular bifurcations of codimension 1 and 2. Section 2.3 considers degenerate Bogdanov-Takens bifurcations of codimension 3 and 4.

2.1 Concepts

We consider a system

$$\dot{u} = f(u, \alpha), \quad (2.1)$$

where $u : \mathbb{R} \rightarrow \mathbb{R}^n$ and $\alpha \in \mathbb{R}^p$ and $f : \mathbb{R}^n \times \mathbb{R}^p \rightarrow \mathbb{R}^n$. We assume that f is a smooth function.

The parameter space \mathbb{R}^p will be divided into regions in which the phase portrait of (2.1) is topologically equivalent. In the simplest situations, these regions are separated by smooth hypersurfaces. This motivates the following definition.

Definition 2.1 (Bifurcation). A *bifurcation* of the system (2.1) occurs when a topologically non-equivalent phase portrait appears when the parameter α is varied. The value of $\alpha = \alpha_0$ at which the bifurcation occurs is called the *bifurcation value*.

So by studying the bifurcations of a particular system one obtains information about the phase portraits appearing in this system and their rearrangement. This provides insight in the (co)existence and stability of equilibria and periodic solutions in the system.

The hypersurfaces separating the regions with a topological equivalent phase portrait are called *bifurcation boundaries*. It turns out that each bifurcation boundary is characterized by specifying a phase object (equilibrium, cycle, ...) and some bifurcation conditions. Bifurcation boundaries can intersect or meet, so that bifurcation boundaries are also subdivided in different regions. The boundaries of these regions can be again smooth hypersurfaces of higher codimension. This leads to the following definition. [19]

Definition 2.2. The *codimension* of a bifurcation is the codimension in \mathbb{R}^p of the bifurcation boundary. Equivalently, the codimension is the number of bifurcation conditions that characterizes the bifurcation boundary.

Intuitively, the codimension of a bifurcation is the number of parameters that must be varied to encounter the bifurcation.

Typically, bifurcations involve a change of stability of an equilibrium or a limit cycle (periodic orbit). The bifurcations involving a change of the phase portrait near an equilibrium are called *local bifurcations*. All other bifurcations are called *global bifurcations*. Most global bifurcations involve limit cycles.

2.1.1 Local bifurcations

Bifurcations of an equilibrium u_0 at parameter α_0 are characterized by the eigenvalues $\lambda_1, \lambda_2, \dots, \lambda_n$ of the Jacobian matrix

$$A := f_u(u_0, \alpha_0). \quad (2.2)$$

Note that simple eigenvalues λ_i depend smoothly on the parameter α when f is smooth. We denote the number of eigenvalues with negative real part by n_s , the number of eigenvalues with zero real part by n_c and the number of eigenvalues with positive real part by n_u . Note that $n_s + n_c + n_u = n$.

Another well-known results is that the system (2.1) has a local stable manifold $W^s(u_0, \alpha_0)$ of dimension n_s , local center manifold $W^c(u_0, \alpha_0)$ of dimension n_c and local unstable manifold $W^u(u_0, \alpha_0)$ of dimension n_u . It can be shown that these manifolds are smooth and depend smoothly on the parameters α . We can consider the restriction of (2.1) to these manifolds. In particular the restriction to the center manifold

$$\dot{y}_c = g_c(y_c, \alpha), \quad y_c \in \mathbb{R}^{n_c}, \quad (2.3)$$

will be of interest. This is because the only ‘interesting’ dynamics occur at the center manifold, as is shown by the following lemma.

Lemma 2.1. Reduction principle [19]. *In a neighborhood of an equilibrium u_0 at $\alpha = \alpha_0$, (2.1) is topological equivalent to the system*

$$\begin{aligned} \dot{y}_c &= g_c(y_c, \alpha) \\ \dot{y}_s &= -y_s \\ \dot{y}_u &= +y_u \end{aligned}, \quad (2.4)$$

where $y_s \in \mathbb{R}^{n_s}$, $y_u \in \mathbb{R}^{n_u}$ and g_c is the RHS of the restriction to the center manifold (2.3).

Note that Lemma 2.1 for $n_c = 0$ implies the Hartman-Grobman Theorem [23], which asserts that any two phase portraits in a neighborhood of u_0 are topologically equivalent when they have the same number of stable and unstable eigenvalues respectively (when $n_c = 0$). This means that a bifurcation can only occur when $n_c > 0$, so when there is a center manifold (of dimension > 0). It should be noted that the center manifold $W^c(u, \alpha)$ and the restriction (2.3) are generally not unique. However, any two choices will be topologically equivalent.

Different types of bifurcations can be characterized by their restriction to the center manifold. This enables the introduction of the *normal form* of the bifurcation

$$\dot{y} = g(y, \beta), \quad y \in \mathbb{R}^{n_c}, \beta \in \mathbb{R}^k. \quad (2.5)$$

Here k is equal to the codimension of the bifurcation. The normal form can be considered as the simplest system with the properties that 1) the bifurcation occurs in the system at $\beta = 0$ and 2) the phase portraits appearing in a neighborhood of $\beta = 0$ are topologically equivalent to the phase portraits appearing in a generic system in which the same bifurcation occurs.

In particular, this means that under certain *nondegeneracy conditions*, there exists a parameter change $\beta(\alpha)$ such that the phase portrait of (2.3) at α and the phase portrait of (2.5) at $\beta = \beta(\alpha)$ are topologically equivalent (in a neighborhood of u_0 and α_0). When these conditions are satisfied, the bifurcation is called *non-degenerate*.

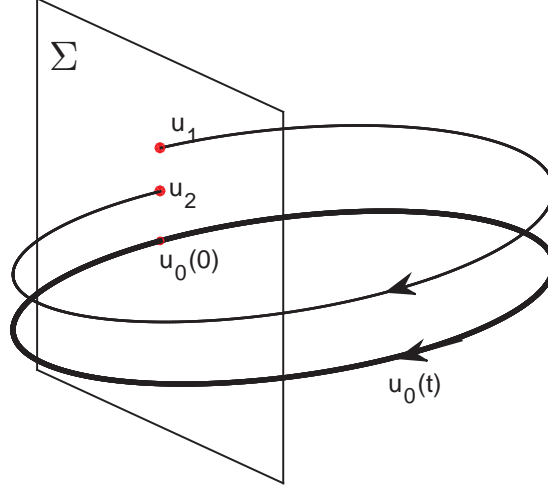


Figure 2.1: The definition of the Poincaré map near the periodic solution $u_0(t)$

The normal form of a bifurcation cannot be determined by considering only the linearization A . Also higher order terms have to be considered. Therefore the following multi-linear forms are introduced

$$B(p, q) = \sum_{i,j=1}^n \frac{\partial^2 f(u, \alpha_0)}{\partial u_i \partial u_j} \Big|_{u=u_0} p_i q_j, \quad (2.6)$$

$$C(p, q, r) = \sum_{i,j,k=1}^n \frac{\partial^3 f(u, \alpha_0)}{\partial u_i \partial u_j \partial u_k} \Big|_{u=u_0} p_i q_j r_k, \quad (2.7)$$

$$D(p, q, r, s) = \sum_{i,j,k,l=1}^n \frac{\partial^4 f(u, \alpha_0)}{\partial u_i \partial u_j \partial u_k \partial u_l} \Big|_{u=u_0} p_i q_j r_k s_l, \quad (2.8)$$

Further, we will denote the standard inner product of two vectors $p, q \in \mathbb{C}^n$ by $\langle p, q \rangle := \bar{p}^\top q$.

In Section 2.2 we will study the normal forms of different bifurcations and discuss how (2.6)–(2.8) can be used to determine the normal form of local bifurcations.

2.1.2 Bifurcations of limit cycles

Suppose that $u_0(t)$ is a periodic solution of (2.1) at parameter $\alpha = \alpha_0$. Note that because the system (2.1) is autonomous, also $u_0(t + t_0)$ is a periodic solution of (2.1) for all $t_0 \in \mathbb{R}$.

Now consider an $(n - 1)$ -dimensional plane Σ through $u_0(0)$ perpendicular to $\dot{u}_0(0)$. It can be shown that an orbit through $u_1 \in \Sigma$ close enough to $u_0(0)$ will again pass through Σ in a point u_2 near u_0 . This situation is illustrated in Figure 2.1. This gives us a map

$$P : \Sigma \rightarrow \Sigma, \quad u_1 \mapsto u_2. \quad (2.9)$$

It can be shown that u_0 is stable if and only if $u_0(0)$ is a stable fixed point of P . The local stability of $u_0(0)$ is determined by the eigenvalues of the linearization of P at $u_0(0)$. This motivates the introduction of the *Floquet multipliers*

$$\mu_1 = 1, \mu_2, \mu_3, \dots, \mu_n. \quad (2.10)$$

Here $\mu_2, \mu_3, \dots, \mu_n$ are the eigenvalues of the linearization of P at $u = u(0)$. In an autonomous system one Floquet multiplier is always one (this is related to the fact that $u_0(t + t_0)$ is also a periodic solution). Also observe that P will depend smoothly on the parameters α when f is smooth.

Local bifurcations of the cycle are determined by bifurcations of the Poincare map P . These bifurcations occur when a multiplier crosses the unit circle in the complex plane, so when $|\mu_i| = 1$, $i \neq 1$. More information on the bifurcation theory for discrete time system is can be found in (for example) [19]. It should be noted that not all global bifurcations are local bifurcations of the cycle. Example of different types of global bifurcations are homoclinic bifurcations in Section 2.2.1

2.2 Different types of bifurcations

In this section local and global bifurcations of codimension 1 and 2 are reviewed. Only the bifurcations occurring near the degenerate Bogdanov-Takens bifurcations in Section 2.3 will be discussed. A more complete discussion can be found in [19].

2.2.1 Codimension 1

We will now discuss some local and global bifurcations of codimension 1. We will discuss 2 local bifurcations and 3 global bifurcations.

First we will consider local bifurcations. Observe that $A \in \mathbb{R}^{n \times n}$ so that the eigenvalues λ_i are either real or come in complex pairs. So either a real eigenvalue or a complex pair will cross the imaginary axis. These two situation correspond to the only two possible local bifurcations of codimension 1.

Fold bifurcation (LP)

When one simple real eigenvalue $\lambda_i = 0$ and all other eigenvalues have nonzero real part, a Fold bifurcation occurs. Note that $n_c = 1$ in this situation, so the normal form is a one-dimensional system,

$$\dot{y} = \beta + ay^2. \quad (2.11)$$

The *quadratic normal form coefficient* $a \in \mathbb{R}$ is nonzero in the nondegenerate situation. Figure 2.2 shows the situation near the fold bifurcation. As can be seen the stable equilibrium and the unstable equilibrium collide and disappear at $\beta = 0$. Note that by scaling y it is always possible to get $a \in \{-1, 1\}$. The situation for $a = +1$ is shown in Figure 2.2. For the case $a = -1$, Figure 2.2 is mirrored in both axis. This follows from the observation that the system (2.11) is invariant under the transformation

$$(y, \beta, a) \mapsto (-y, -\beta, -a).$$

The Fold bifurcation is also called a Limit Point (LP) or Saddle-Node bifurcation.

In an n -dimensional system the coefficient a can be computed from the the eigenvector q and adjoint eigenvector p . These satisfy

$$Aq = 0, \quad A^\top p = 0, \quad (2.12)$$

and can be normalized such that $\langle q, q \rangle = \langle p, p \rangle = 1$. The normal form coefficient a can then be computed as

$$a = \frac{1}{2} \langle p, B(q, q) \rangle, \quad (2.13)$$

where the multilinear form B is defined in (2.6).

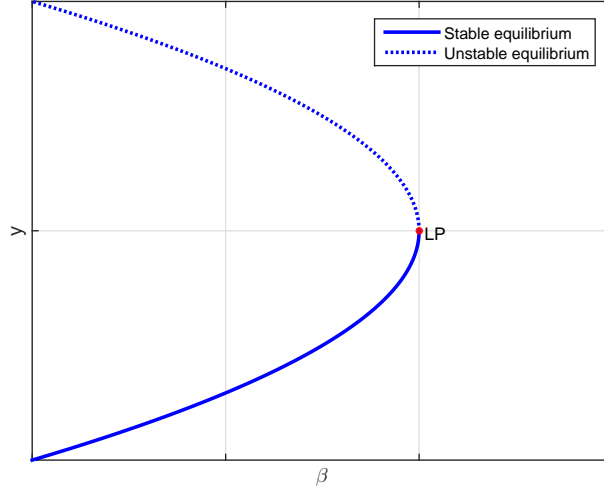


Figure 2.2: Parametric portrait for the normal form of the fold bifurcation for $a = 1$.
A stable (solid line) and an unstable (dashed line) equilibrium collide.

Hopf bifurcation (H)

When one (simple) complex pair $\lambda_{k,k+1} = \pm i\omega$ crosses the imaginary axis, a Hopf bifurcation occurs. In this case the center manifold is 2-dimensional. Now the normal form is a 2-dimensional system

$$\begin{aligned}\dot{y}_1 &= \beta y_1 - y_2 + l_1 y_1(y_1^2 + y_2^2), \\ \dot{y}_2 &= y_1 + \beta y_2 + l_1 y_2(y_1^2 + y_2^2).\end{aligned}\tag{2.14}$$

The coefficient l_1 is called the *first Lyapunov coefficient* and the Hopf bifurcation is nondegenerate when $l_1 \neq 0$. Again we can obtain $l_1 \in \{-1, 1\}$ by rescaling y , but the sign of l_1 cannot be changed as was possible for the Fold bifurcation.

Depending on the sign of l_1 , the Hopf bifurcation in (2.14) is either supercritical or subcritical. When $l_1 > 0$ the Hopf bifurcation is called *subcritical* and for $l_1 < 0$ the Hopf bifurcation is *supercritical*. Typical phase portraits around subcritical and supercritical Hopf bifurcation are shown in Figure 2.3a and Figure 2.3b.

The normal form coefficient l_1 can be computed from the eigenvectors

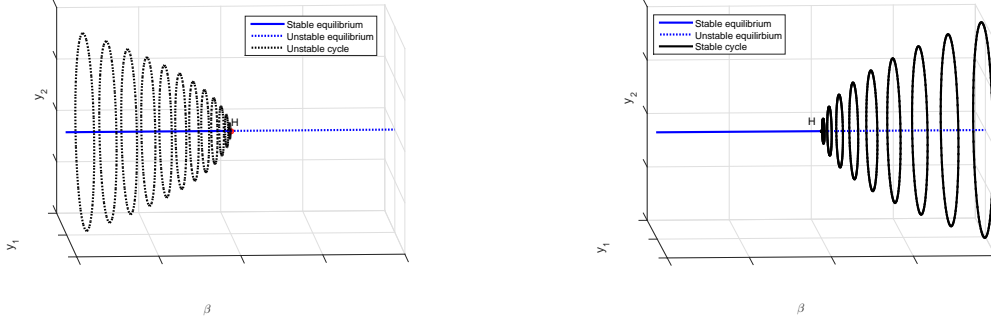
$$Aq = i\omega q, \quad A^\top p = -i\omega p,\tag{2.15}$$

which are normalized such that $\langle q, q \rangle = \langle p, q \rangle = 1$. The formula for l_1 is then

$$l_1 = \frac{1}{2} \text{Re} \left[\langle p, C(q, q, \bar{q}) - 2B(q, A^{-1}B(q, \bar{q})) + B(\bar{q}, (2i\omega I - A)^{-1}B(q, q)) \rangle \right].\tag{2.16}$$

Fold of Cycles (LPC)

The fold of cycles bifurcation occurs when a cycle has a simple multiplier $\mu_i = 1$, $i \neq 1$. This means that the Poincaré map P experiences a Fold bifurcation (in the sense of discrete time systems), so on



(a) Subcritical Hopf bifurcation ($l_1 > 0$). An unstable cycle shrinks to the stable equilibrium. (b) Supercritical Hopf bifurcation ($l_1 < 0$). A stable cycle shrinks to the unstable equilibrium.

Figure 2.3: Subcritical and supercritical Hopf bifurcation

the (1-dimensional) centermanifold of the fixed point a stable and an unstable fixed point collide and disappear. This implies that at a fold of cycles a stable and unstable cycle collide and disappear in the (2-dimensional) center manifold of the cycle. The Fold of cycles bifurcation is also called a Limit Point of Cycles (LPC) or a cyclic fold.

Period doubling (PD)

The period doubling bifurcation occurs when a cycle has a simple multiplier $\mu_i = -1$, $i = -1$. At a period doubling bifurcation a cycle of period 2 appears in the Poincare map. This implies that a branch of cycles of period approaching $2T$ in the system (2.1) appears. Also the original period T cycle remains, but has one multiplier with $|\mu_i| > 1$ more.

Homoclinic to hyperbolic saddle (HHS)

Consider an *hyperbolic* equilibrium u_0 of (2.1) (so $n_c = 0$). A homoclinic orbit of the system is defined by a solution $u(t)$ that starts and ends in u_0 ,

$$\lim_{t \rightarrow -\infty} u(t) = u_0 \quad \lim_{t \rightarrow +\infty} u(t) = u_0. \quad (2.17)$$

In other words, the stable and unstable manifold of u_0 have a non-empty intersection. Near a homoclinic orbit there exists a branch of limit cycles of arbitrarily large period. The homoclinic orbit can be considered as a cycle of ‘infinite’ period. The homoclinic bifurcation is illustrated in Figure 2.4.

There exists various types and degeneracies of this type of homoclinic orbit, see for example [11, 26]. These degeneracies can be either due to the eigenvalues at the equilibrium u_0 or a change in the global structure of orbits near the homoclinic orbit $u(t)$. Two degeneracies will be discussed in Section 2.2.2.

Homoclinic to saddle node (HSN)

Before the the homoclinic to saddle node node bifurcation can be discussed, the heteroclinic orbit must be introduced. Let u_- and u_+ be two different equilibria of (2.1). An *heteroclinic* orbit $u(t)$ connects u_- and u_+ in the sense that

$$\lim_{t \rightarrow -\infty} u(t) = u_- \quad \lim_{t \rightarrow +\infty} u(t) = u_+. \quad (2.18)$$

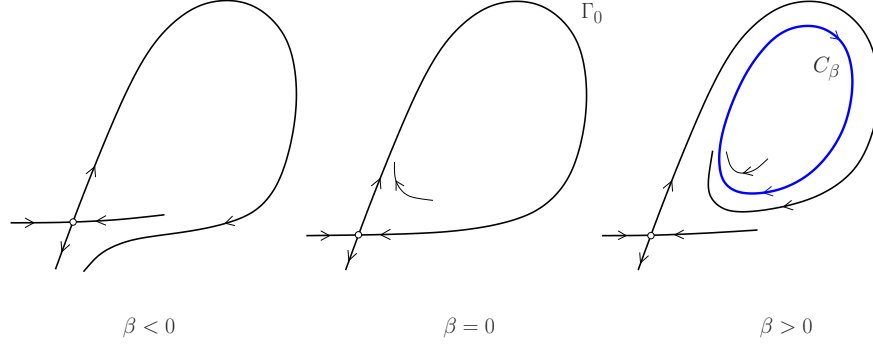


Figure 2.4: Phase portraits near a homoclinic to hyperbolic equilibrium bifurcation

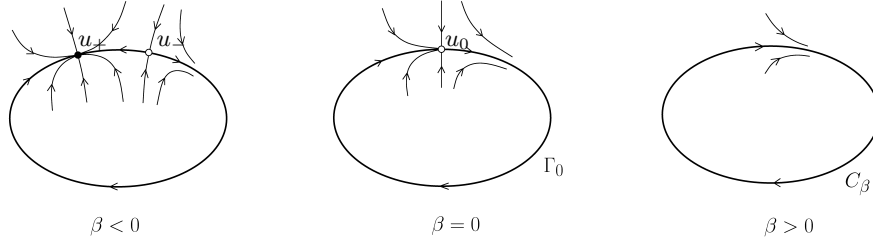


Figure 2.5: Phase portraits near a homoclinic to saddle node bifurcation

So an heteroclinic orbit is the intersection of the unstable and stable manifold of two different equilibria.

Close to the HSN bifurcation the equilibria u_- and u_+ are connected by two heteroclinic orbits, as indicated in Figure 2.5 for $\beta < 0$. The HSN bifurcation now occurs when the two equilibria u_- and u_+ collide and disappear at a fold bifurcation. After the collision a cycle remains. Note that at the HSN bifurcation the equilibrium has $n_c = 1$, in contrast to the HHS bifurcation where $n_c = 0$.

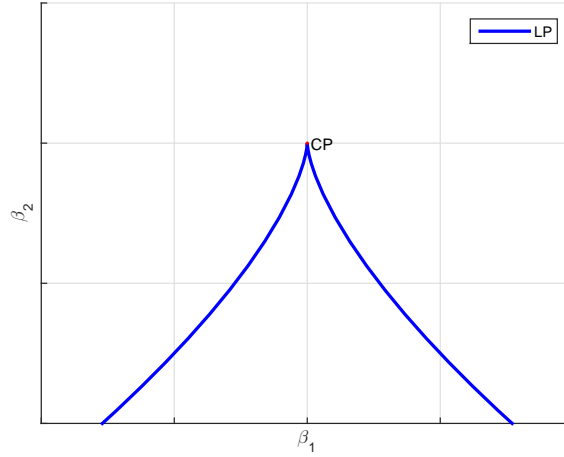


Figure 2.6: The parametric portrait of (2.19) for $c = 1$. The solid lines represent Fold bifurcations.

2.2.2 Codimension 2

In this section we will discuss 3 local and 2 global bifurcations of codimension 2. These are exactly the codimension-2 bifurcations occurring near the degenerate BT bifurcations discussed in Section 2.3.

Recall that the type of a local bifurcation is characterized by the restriction of (2.1) to $W^c(x_0, \alpha_0)$. This restriction will only change either when n_c changes or when the non-degeneracy conditions are violated. This results in 5 possible local bifurcations of codimension 2. We will discuss only 3 of them.

Cusp bifurcation (CP)

A cusp bifurcation (CP) occurs when a simple zero eigenvalue is present (so an LP bifurcation occurs) and $a = 0$ in (2.11). The Cusp bifurcation can thus be considered as a degenerate LP bifurcation. The normal form is

$$\dot{y} = \beta_1 + \beta_2 y + c y^3. \quad (2.19)$$

For a nondegenerate cusp bifurcation $c \neq 0$. Note that by rescaling y we can always obtain $c \in \{-1, 1\}$. The parametric portrait of (2.19) for $c = 1$ is shown in Figure 2.6. The case $c < 1$ can be obtained by time reversal. So at a Cusp bifurcation two branches of Fold bifurcations meet tangentially. The computational formula for the coefficient c in n -dimensional systems can be found in [15].

Generalized Hopf bifurcation (GH)

A generalized Hopf (GH) bifurcation is a degenerate case of the Hopf bifurcation. It occurs when a simple pair of purely imaginary eigenvalues is present but $l_1 = 0$ in (2.14). The normal form is

$$\begin{aligned} \dot{y}_1 &= \beta_1 y_1 - y_2 + \beta_2 y_1 (y_1^2 + y_2^2) + l_2 y_1 (y_1^2 + y_2^2)^2, \\ \dot{y}_2 &= y_1 + \beta_1 y_2 + \beta_2 y_2 (y_1^2 + y_2^2) + l_2 y_2 (y_1^2 + y_2^2)^2. \end{aligned} \quad (2.20)$$

The coefficient l_2 is called the *second Lyapunov coefficient* and is non-zero at a non-degenerate GH point. The parametric portrait of (2.20) is shown in Figure 2.7. As can be seen, a fold of cycles meets the Hopf

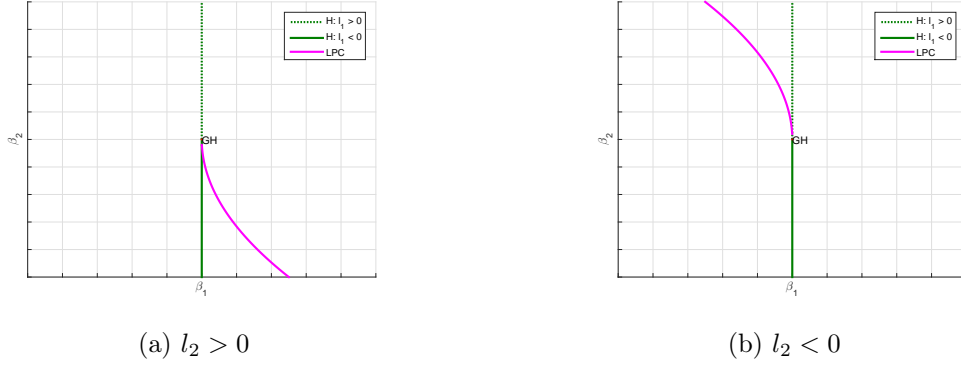


Figure 2.7: The parametric portrait of (2.20) for $l_2 > 0$ and $l_2 < 0$

curve at a GH bifurcation. The cases $l_2 > 0$ and $l_2 < 0$ are different. When $l_2 > 0$ the fold of cycles curve is tangent to the curve of supercritical Hopf bifurcations. When $l_2 < 0$ the fold of cycles curve is tangent to the curve of subcritical Hopf bifurcations. The computational formula for l_2 can be found in [14].

Bogdanov-Takens bifurcation (BT)

A Bogdanov-Takens bifurcation (BT) occurs when we have an zero eigenvalue of algebraic multiplicity 2 and geometric multiplicity 1, so the linearization A contains a Jordan Block of the form

$$\begin{pmatrix} 0 & 1 \\ 0 & 0 \end{pmatrix}. \quad (2.21)$$

The normal form is given by

$$\begin{aligned} \dot{y}_1 &= y_2, \\ \dot{y}_2 &= \beta_1 + \beta_2 y_2 + a_2 y_1^2 + b_2 y_1 y_2. \end{aligned} \quad (2.22)$$

Here $a_2 b_2 \neq 0$ at a nondegenerate BT bifurcation. In Section 2.3 we will investigate degenerate situations when $a_2 b_2 = 0$. The parametric portrait of (2.22) for $a_2 = b_2 = 1$ is shown in Figure 2.8. Near a BT point branches of LP, H and HHS bifurcations are present. Also note that the H curve continues as a neutral saddle curve (two real eigenvalues that satisfy $\lambda_i + \lambda_j = 0$) after the BT bifurcation. Note that the neutral saddle curve is not a bifurcation curve.

Now observe that by rescaling y_1, y_2 and time, we can always obtain $a_2, b_2 \in \{-1, 1\}$. So in principle there are four different situations $a_2 = \pm 1, b_2 = \pm 1$. Also note that the transformation $y \mapsto -y$ transforms (a_2, b_2) to $(-a_2, -b_2)$ and the transformation $(y_1, y_2, t) \mapsto (y_1, -y_2, -t)$ transforms (a_2, b_2) to $(-a_2, +b_2)$. So all four situations can be obtained from the case $a_2 = b_2 = 1$ by (a combination of) these transformations.

In an general n -dimensional system the normal form coefficients a_2 and b_2 are computed from the (generalized) eigenvectors

$$Aq_0 = 0, \quad Aq_1 = q_0, \quad A^\top p_1 = 0, \quad A^\top p_0 = p_1, \quad (2.23)$$

which are normalized such that $\langle p_0, q_0 \rangle = \langle p_1, q_1 \rangle = 1$ and $\langle p_0, q_1 \rangle = \langle p_1, q_0 \rangle = 0$. The normal form coefficients can then be computed as

$$a_2 = \frac{1}{2} \langle p_1, B(q_0, q_0) \rangle, \quad b_2 = \langle p_0, B(q_0, q_0) \rangle + \langle p_1, B(q_0, q_1) \rangle. \quad (2.24)$$

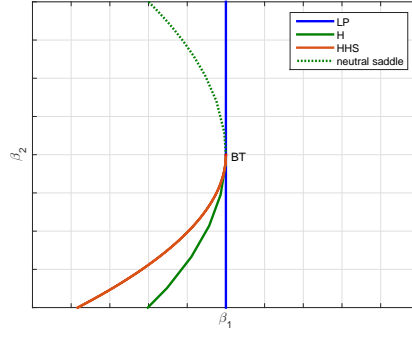


Figure 2.8: The parametric portrait of (2.22) for $a_2 = 1$ and $b_2 = -1$.

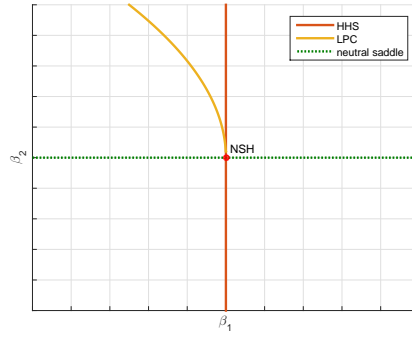


Figure 2.9: The parametric portrait near a neutral saddle homoclinic bifurcation.

Neutral saddle homoclinic (NSH)

The neutral saddle homoclinic bifurcation occurs when fold of cycles (LPC) and homoclinic (HHS) curves meet. The LPC curve stops at the NSH point and the HHS curve continues. At this point the equilibrium involved in the homoclinic bifurcation has two (real) eigenvalues λ_i, λ_j such that $\lambda_i + \lambda_j = 0$, so also a neutral saddle curve passes through the NSH point. This situation is illustrated in Figure 2.9.

Non-central homoclinic to saddle node (NCH)

The non-central homoclinic bifurcation occurs when Fold (LP) and homoclinic (HHS) curves meet. The equilibrium with the homoclinic orbit undergoes a fold bifurcation, so it collides with another equilibrium and disappears. The LP curve becomes a HSN curve at the NCH curve, as shown in Figure 2.10.

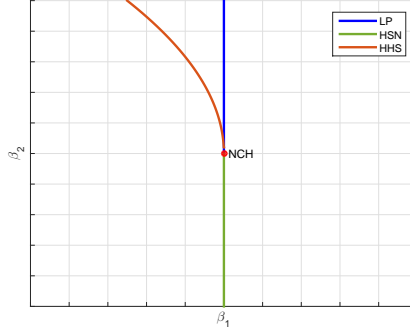


Figure 2.10: The parametric portrait near a non-central homoclinic bifurcation.

2.3 Degenerate BT bifurcations

We will now investigate situations where the nondegeneracy condition $a_2 b_2 \neq 0$ of (2.22) is no longer satisfied. In Section 2.3.1 and Section 2.3.2 the two codimension-3 situations $b_2 = 0, a_2 \neq 0$ and $a_2 = 0, b_2 \neq 0$ are considered. In Section 2.3.3 the codimension-4 situation $a_2 = b_2 = 0$ is addressed.

An important result is that when A has a Jordan block of the form (2.21) and $n_c = 2$, the restriction to the center manifold is formally smoothly equivalent to [20, 1]

$$\begin{aligned} \dot{y}_1 &= y_2, \\ \dot{y}_2 &= \sum_{k \geq 2} a_k y_1^k + b_k y_1^{k-1} y_2^k. \end{aligned} \quad (2.25)$$

Note that the normal form (2.22) appears when only terms for $k = 2$ are considered. We will need the higher order normal form coefficients a_3, b_3, a_4 and b_4 . These can be computed from the eigenvectors (2.23) and the multi-linear forms (2.6)–(2.8) [20]. Here we only give the formulas for a_3 and b_3 ,

$$a_3 = \frac{1}{6} \langle p_1, C(q_0, q_0, q_0) \rangle + \frac{1}{2} \langle p_1, B(h_{20}, q_0) \rangle + \frac{a_2}{2} \langle p, B(q_1, q_1) \rangle, \quad (2.26)$$

$$\begin{aligned} b_3 &= \frac{1}{2} \langle p_1, C(q_0, q_0, q_1) \rangle + 2B(h_{11}, q_0) + B(h_{20}, q_1) \rangle - \frac{b_2}{2} \langle p_1, B(q_1, q_1) \rangle \\ &\quad + \frac{1}{2} \langle p_0, C(q_0, q_0, q_0) \rangle + 3B(h_{20}, q_0) \rangle + a_2 \langle p_0, B(q_1, q_1) \rangle - 5a_2 \langle p_0, h_{11} \rangle. \end{aligned} \quad (2.27)$$

where q_0, q_1, p_0 and p_1 are as in (2.23), a_2 and b_2 are computed using (2.24), and h_{20} and h_{11} must satisfy

$$Ah_{20} = a_2 q_1 - B(q_0, q_0), \quad Ah_{11} = b_2 q_1 + h_{20} - B(q_0, q_1). \quad (2.28)$$

2.3.1 The case $b_2 = 0, a_2 \neq 0$

When $b_2 = 0$ we need to consider terms for $k > 2$ in (2.25); the normal form becomes [9]:

$$\begin{aligned} \dot{y}_1 &= y_2, \\ \dot{y}_2 &= \beta_1 + \beta_2 y_2 + \beta_3 y_1 y_2 + a_2 y_1^2 + b_4 y_1^3 y_2. \end{aligned} \quad (2.29)$$

To make a clear picture of the structure near $(\beta_1, \beta_2, \beta_3) = (0, 0, 0)$, it is convenient to use cylindrical coordinates

$$(\beta_1, \beta_2, \beta_3) = (r \sin(\theta), \beta_2, r \cos(\theta)) \quad (2.30)$$

Figure 2.11 shows the section for $r = \text{const}$ and $a_2, b_4 > 0$. Observe that the direction of the H-curve changes when moving through the degenerate BT point. Further there is an GH point from which an LPC curve starts. The LPC curve stops when it collides the HHS curve at the NSH point. Note that the neutral saddle curve also passes through the NSH point. More details can be found in [9].

For all other combinations of the signs a_2 and b_4 parametric portrait in Figure 2.11 remains valid. The transformation $y \mapsto -y$ gives transforms (a_2, b_4) to $(-a_2, -b_4)$ and the transformation $(y_1, y_2, t) \mapsto (y_1, -y_2, -t)$ transforms (a_2, b_4) to $(-a_2, +b_4)$.

2.3.2 The case $a_2 = 0, b_2 \neq 0$

In this case the normal form becomes [10]:

$$\begin{aligned}\dot{y}_1 &= y_2, \\ \dot{y}_2 &= \beta_1 + \beta_2 y_1 + \beta_3 y_2 + a_3 y_1^3 + b_2 y_1 y_2 + b'_3 y_1^2 y_2,\end{aligned}\tag{2.31}$$

where

$$b'_3 = b_3 - \frac{3b_2}{5a_3}.$$

The bifurcation structure again becomes more clear in cylindrical coordinates,

$$(\beta_1, \beta_2, \beta_3) = (\beta_1, r \cos(\theta), r \sin(\theta)).\tag{2.32}$$

Because we can change the sign of b_2 by applying the transformation $y \mapsto -y$, we can assume without loss of generality that $b_2 > 0$. Now there are three possible situations, depending on the values of a_3, b_2 and b'_3 ,

- $a_3 > 0$,
- $a_3 < 0$ and $b_2^2 + 8a_3 < 0$,
- $a_3 < 0$ and $b_2^2 + 8a_3 > 0$.

Figure 2.12 shows the transitions for the second situation ($a_3 < 0$ and $b_2^2 + 8a_3 < 0$). As can be seen this situation involves CP, GH, NSH and NCH bifurcations. Also note that the H-curve connects from $\theta = +180^\circ$ to $\theta = -180^\circ$. When passing through this type of degenerate Bogdanov-Takens bifurcation, the BT point moves to the other side of the CP point. All three cases are discussed in detail in [10].

2.3.3 The case $a_2 = b_2 = 0$

The normal form for this codimension-4 situation is [18]:

$$\begin{aligned}\dot{y}_1 &= y_2, \\ \dot{y}_2 &= \beta_1 + \beta_2 y_1 + \beta_3 y_2 + \beta_4 y_1 y_2 + a_3 y_1^3 + b_3 y_1^2 y_2.\end{aligned}\tag{2.33}$$

It will be convenient to use again cylindrical coordinates,

$$(\beta_1, \beta_2, \beta_3, \beta_4) = (\beta_1, r \cos(\theta), r \sin(\theta), \beta_4).\tag{2.34}$$

Note that we can scale y such that $a_3, b_3 \in \{-1, 1\}$ and that the transformation $(y_1, y_2, t) \mapsto (+y_1, -y_2, -t)$ transforms (a_3, b_3) to $(a_3, -b_3)$. This means that there are two situations, either $a_3 > 0$ or $a_3 < 0$. The

case $a_3 < 0$ is the physical most relevant one, because it involves coexisting stable equilibria. This case is also extensively studied in [18]. The other case has not been studied in literature (to our best knowledge).

We will further only consider the case $a_3, b_3 < 0$. Figure 2.13, Figure 2.14 and Figure 2.15 show the different sections in the (β_1, θ) -space for $r, \beta_4 \ll 1$ constant. The diagram for $\beta_4 = 0$ is symmetric around the β_2 -axis because of the symmetry

$$(y_1, y_2, \beta_1, \beta_2, \beta_3, \beta_4) \mapsto (-y_1, -y_2, -\beta_1, +\beta_2, +\beta_3, -\beta_4).$$

This symmetry also explains why the diagram for $\beta_4 < 0$ can be mirrored around the θ -axis to obtain the diagram for $\beta_4 > 0$. When $|\beta_4|$ is increased the symmetry around the $\beta_1 = 0$ is destroyed. Depending on the value of β_4 , there are 12 (topologically) different sections [18].

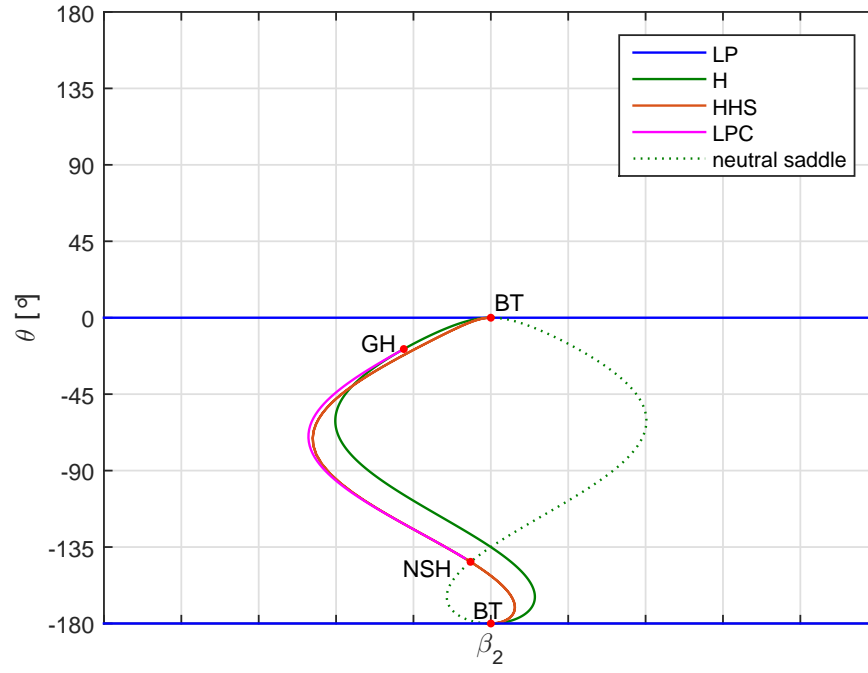


Figure 2.11: The parametric portrait of the system (2.29) for $a_2 = b_4 = 1$.

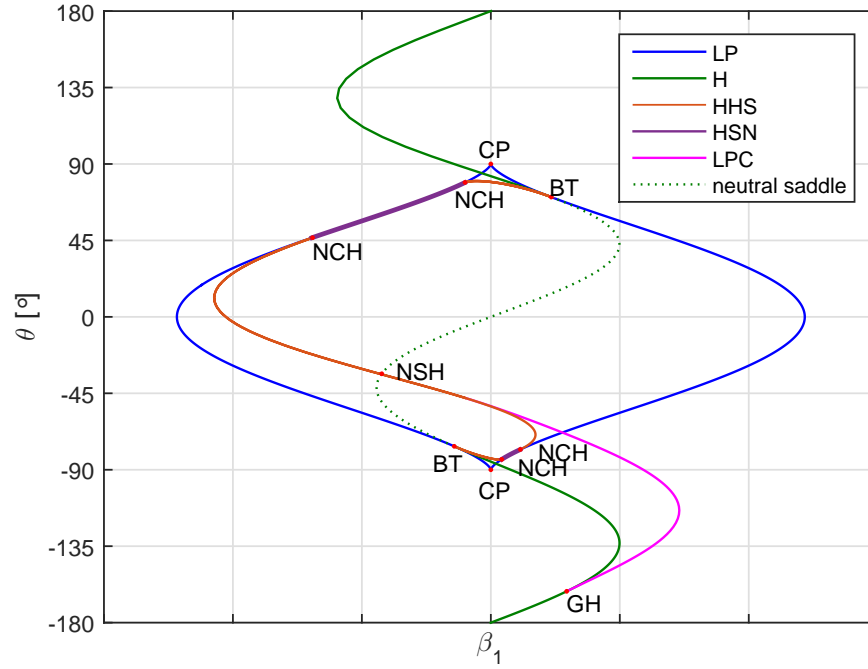


Figure 2.12: Parametric portrait of the system (2.31) for $a_3 = 1$, $b_2 = 1$ and $b'_3 = 1$

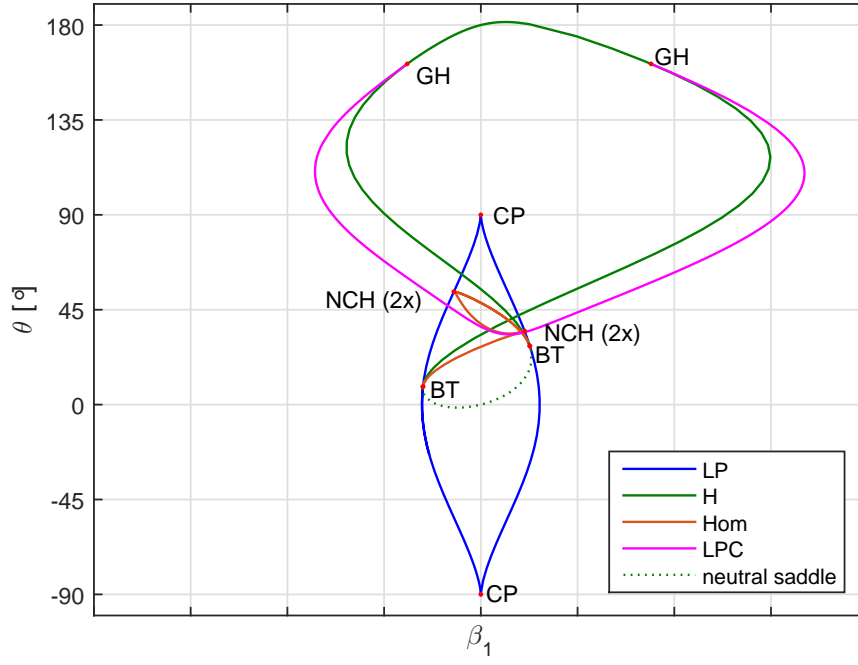


Figure 2.13: Parametric portrait of the system (2.33) for $a_3 = b_2 = -1$ and $\beta_4 < 0$.

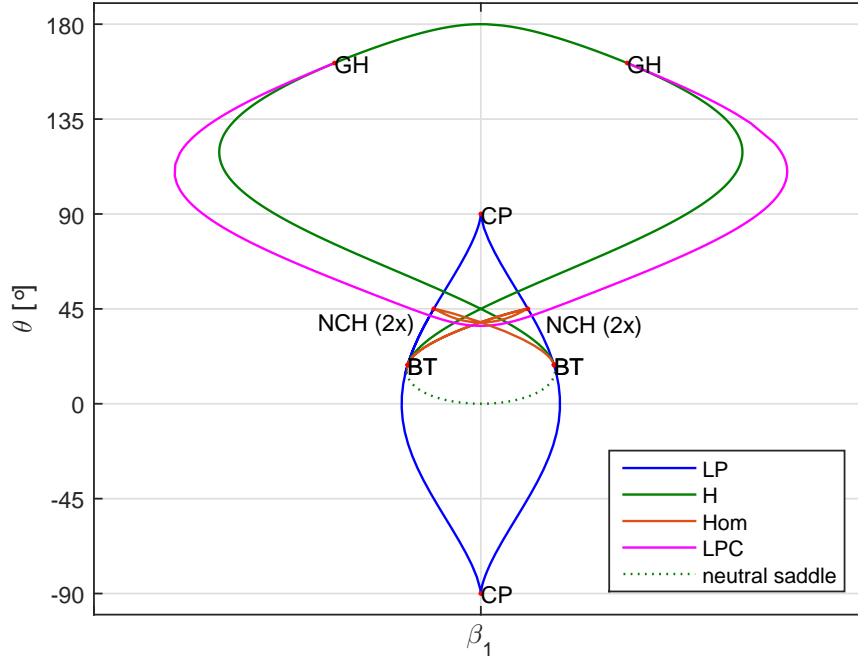


Figure 2.14: Parametric portrait of the system (2.33) for $a_3 = b_2 = -1$ and $\beta_4 = 0$.

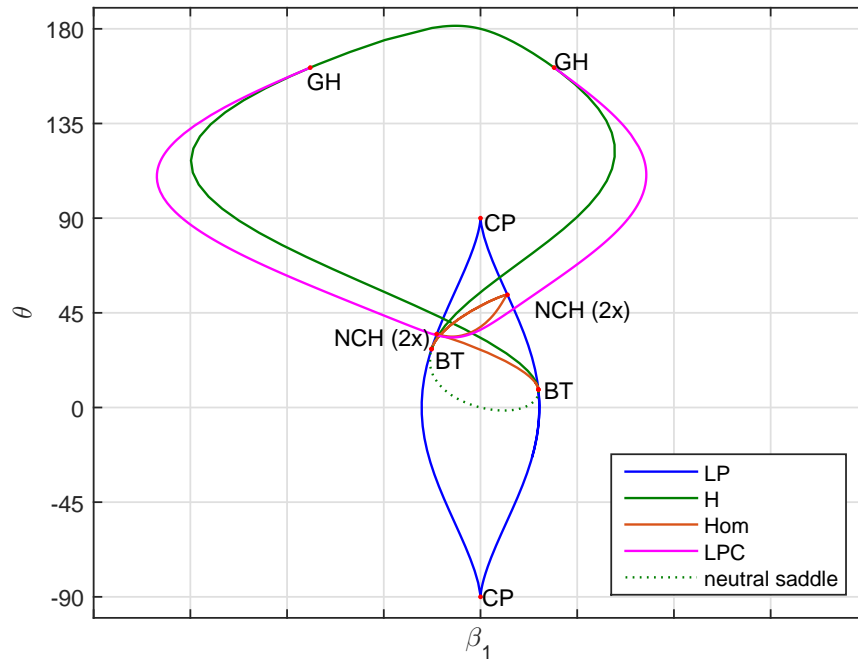


Figure 2.15: Parametric portrait of the system (2.33) for $a_3 = b_2 = -1$ and $\beta_4 > 0$.

Chapter 3

Numerical continuation of equilibria in large-scale systems

This chapter summarizes the techniques that are used for the numerical continuation of a curve of (bifurcations of) equilibria of the system (2.1). In particular the focus will be on how these techniques are implemented in CL_MATCONTL [4]. The continuation of BT bifurcations is not supported in the ‘normal’ version of CL_MATCONT or in the version of CL_MATCONTL in [4], but has been added to current version of CL_MATCONTL. Also the computation of the LP and H curves has been slightly changed compared to the version of CL_MATCONTL in [4]. In particular, we propose a new method to compute the Jacobian matrix along the H, LP and BT curves using subspace reduction techniques. Also the detection of the bifurcations along these curves has been changed slightly.

Section 3.1 will discuss the continuation procedure for a given curve type. Section 3.2 discusses bordering techniques, which are used for an efficient implementation of the different bifurcation curves. This section forms the basis of the new computation of the Jacobian Matrix along the LP, H, and BT curves. Section 3.3 discusses the implementation in the current version of CL_MATCONTL.

3.1 Continuation algorithm

This section discusses the continuation algorithm for a curve of (bifurcations of) equilibria in large-scale systems. Section 3.1.1 discusses the basics of the continuation algorithm and detection of singularities. In Section 3.1.2 the Continuation of Invariant Subspaces (CIS) algorithm is discussed, which results in a more efficient implementation for large-scale systems. Section 3.1.3 discusses the implementation of these techniques in CL_MATCONTL.

3.1.1 Continuation and detection of singularities

Every curve is characterized by a defining system,

$$F(X) = 0, \quad F : \mathbb{R}^{N+1} \rightarrow \mathbb{R}^N. \quad (3.1)$$

The defining system F is different for the equilibrium, LP, H and BT curves and will be discussed in Section 3.3.

A solution X_0 of (3.1) is called a *regular* solution when $F_X(X_0)$ has full rank. An application of the Implicit Function Theorem [8] now gives the following result.

Theorem 3.1. [2] *Let X_0 be a regular solution of (3.1). Then there exists a unique one-dimensional continuum of solutions $X(s)$ with $X(0) = X_0$ near X_0 .*

The most natural way to compute a branch of solutions is by Keller's method [2]. This method uses the direction vector $\dot{X}_0 = \left. \frac{dX(s)}{ds} \right|_{s=0}$. Another point X_1 on the branch of solutions is computed as the solution of the system

$$\begin{cases} F(X_1) = 0, \\ \dot{X}_0^\top X_1 = h, \end{cases} \quad (3.2)$$

where h is the stepsize. By applying the chain rule for differentiation to (3.1) it is easy to see that $F_X(X_0)\dot{X}_0 = 0$. This observation leads to the following result.

Theorem 3.2. [2] *The Jacobian of Keller's equations (3.2) is nonsingular at a regular solution.*

The above result is important because it makes it possible to use Newton iteration to solve the system (3.2). The new tangent vector \dot{X}_1 at X_1 can now be computed by solving the linear system

$$\begin{bmatrix} F_X(X_1) \\ \dot{X}_0^\top \end{bmatrix} [\dot{X}_1] = \begin{bmatrix} 0 \\ 1 \end{bmatrix} \quad (3.3)$$

A branch of solutions $X(s_k)$ ($k = 1, 2, \dots$) can now be traced by repeating the steps above.

A singularity (=bifurcation) along a branch of solutions $X(s)$ is detected using *testfunctions* $\psi_j(s)$ ($j = 1, 2, \dots, N_{test}$). Based on the values $\psi_j(s_k)$ and $\psi_j(s_{k+1})$ a singularity can be detected. This is typically done by detecting a change in sign of $\psi_j(s_k)$ and $\psi_j(s_{k+1})$. The exact procedure is described in Section 3.3.

The user can also define his own *userfunctions* $\phi_i(s)$. The solutions $X(s)$ for which a userfunction $\phi_i(s) = 0$ are also computed by CL_MATCONT. A user function can be used to find an equilibrium at a particular parameter value.

3.1.2 Continuation of invariant subspaces (CIS)

Now we focus on the situation where the dimension n of the system (2.1) is large. The bifurcations in these systems are typically related to a relatively low number of eigenvalues of $A = f_u$. For large systems it is efficient to consider the reduction of A to the subspace corresponding to these eigenvalues.

In particular, the spectrum $\Lambda(s) = \{\lambda_1(s), \lambda_2(s), \dots, \lambda_n(s)\}$ of the matrix $A(s)$ is partitioned as

$$\Lambda(s) = \Lambda_1(s) \cup \Lambda_2(s) \quad (3.4)$$

where $\Lambda_1(s)$ contains all the unstable eigenvalues and the $n_{ss} \ll n$ rightmost stable eigenvalues. The following result shows that there exists a smooth basis $Q_1(s)$ for the subspace corresponding to $\Lambda_1(s)$, when $\Lambda_1(s)$ and $\Lambda_2(s)$ are disjoint.

Theorem 3.3. Smooth Schur factorization [3] [26]. *Suppose $A(s)$ depends smoothly on s and that $\Lambda_1(s)$ and $\Lambda_2(s)$ are disjoint. Then there exists a smooth Schur decomposition*

$$A(s) = \begin{bmatrix} Q_1(s) & Q_2(s) \end{bmatrix} \begin{bmatrix} T_{11}(s) & T_{12}(s) \\ 0 & T_{22}(s) \end{bmatrix} \begin{bmatrix} Q_1(s) & Q_2(s) \end{bmatrix}^\top, \quad (3.5)$$

where $Q_1(s)$ is a basis for the subspace corresponding to $\Lambda_1(s)$.

The restriction of $A(s)$ to the subspace corresponding to $\Lambda_1(s)$ is denoted by

$$C(s) = T_{11}(s) = Q_1(s)^\top A(s) Q_1(s) \in \mathbb{R}^{m \times m}. \quad (3.6)$$

The CIS-algorithm [3] computes $Q_1(s_1)$ for given $A(s_1)$, $A(s_0)$, $Q_1(s_0)$ and $Q_2(s_0)$. This is done by solving the following Ricatti equation for Y ,

$$\hat{T}_{22}(s_1)Y - Y\hat{T}_{11}(s_1) + E_{21}(s_1) - Y\hat{T}_{12}(s_1)Y = 0, \quad (3.7)$$

where

$$\begin{bmatrix} \hat{T}_{11}(s_1) & \hat{T}_{12}(s_1) \\ E_{21}(s_1) & \hat{T}_{22}(s_1) \end{bmatrix} = [Q_1(s_0) \quad Q_2(s_0)] A(s_1) [Q_1(s_0) \quad Q_2(s_0)]^\top. \quad (3.8)$$

The matrix $Q_1(s_1)$ can be computed from the solution Y as

$$Q_1(s_1) = [Q_1(s_0) \quad Q_2(s_0)] \begin{bmatrix} I \\ Y \end{bmatrix} (I + Y^\top Y)^{-1/2} \quad (3.9)$$

Note that the computation above also requires the (relatively large) matrix $Q_2(s_0)$. By further modification of the algorithm this can be avoided [3].

It should also be noted that the definition of $\Lambda_1(s)$ implies that the number of elements in $\Lambda_1(s)$ can change along the curve. This happens when the number of unstable eigenvalues changes. It is also possible that eigenvalues move from $\Lambda_1(s)$ to $\Lambda_2(s)$. This situation is called *overlap*. This situation is detected by computing the rightmost eigenvalues of $\Lambda_2(s)$ at every step. There are different types of overlaps [3]. When the number of eigenvalues in $\Lambda_1(s)$ changes or when an overlap occurs, the CIS algorithm must be reinitialized.

3.1.3 Implementation in CL_MATCONTL

CL_MATCONTL is the continuation package specially aimed at large systems. The basis of the code of CL_MATCONTL is formed by CL_MATCONT [7]. At the moment CL_MATCONTL only supports local bifurcations.

The main algorithm for the continuation used in CL_MATCONTL is visualized in Figure 3.1. The main issue is the choice of the stepsize h in (3.2). When the stepsize is too large different problems can arise. Most of these problems can be solved by reducing the stepsize. Note that the stepsize is also reduced when more than one singularity is detected in one step. This condition is not used in the ‘standard’ version CL_MATCONT.

Also note that the stepsize is *not* reduced when the location of singularities or userfunctions fails. The location can only be improved by increasing the number iterations used for the location. However, increasing the number of iterations might not work when the testfunction/userfunction behaves badly at the singularity.

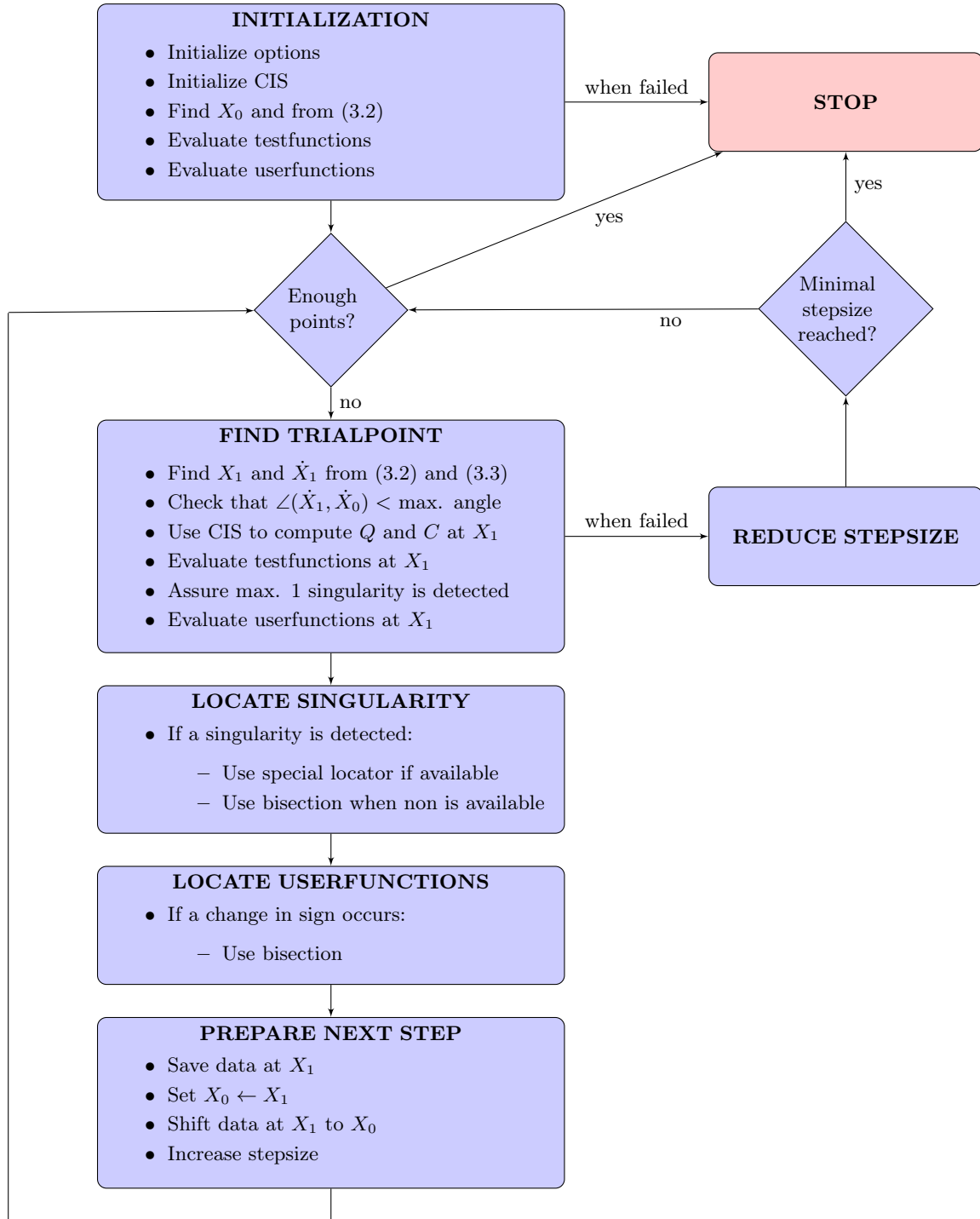


Figure 3.1: The structure of the continuer

3.2 Bordered systems

Bifurcations of equilibria are typically characterized by a rank deficit of a (parameter dependent) matrix $M \in \mathbb{R}^{n \times n}$. These rank deficiencies can be located efficiently using bordered systems. This are system of the form

$$\begin{bmatrix} M & W_{\text{bor}} \\ V_{\text{bor}}^\top & 0_k \end{bmatrix} \begin{bmatrix} V \\ G \end{bmatrix} = \begin{bmatrix} 0_{n \times k} \\ I_k \end{bmatrix}, \quad (3.10)$$

where $V_{\text{bor}}, W_{\text{bor}} \in \mathbb{R}^{n \times k}$. Here k will be small, typically $k = 1$ or $k = 2$. Now we have the following result.

Lemma 3.1. Bordering lemma [13]. *Suppose that the matrix on the left of (3.10) is non-singular, then M has rank deficit r if and only if the solution G has rank deficit r .*

To apply this result the borders V_{bor} and W_{bor} must be selected such that the matrix on the left of (3.10) is non-singular. This can be done using the following result.

Lemma 3.2. Construction of bordered matrices [13]. *Suppose that M in (3.10) has rank deficit k . If the columns of $W_{\text{bor}} \in \mathbb{R}^{n \times k}$ span a subspace transversal to $\mathcal{R}(A)$ and the columns of $V_{\text{bor}} \in \mathbb{R}^{n \times k}$ span a subspace transversal to $\mathcal{R}(A^\top)$, then the bordered matrix is non-singular.*

Elements of G are often included in the defining system (3.1) of a curve of bifurcations. In this situation the matrix $M = M(X)$ depends on the vector $X \in \mathbb{R}^N$. In order to solve the system (3.1) by Newton iteration, the Jacobian F_X is needed. This means that also the derivatives G_X must be computed (efficiently). This is done by the following result.

Lemma 3.3. [13] *Let $V = V(X)$, $G = G(X)$, $W = W(X)$ and $\tilde{G} = \tilde{G}(X)$ be the solutions to*

$$\begin{bmatrix} M(X) & W_{\text{bor}} \\ V_{\text{bor}}^\top & 0_k \end{bmatrix} \begin{bmatrix} V(X) \\ \tilde{G}(X) \end{bmatrix} = \begin{bmatrix} 0_{n \times k} \\ I_k \end{bmatrix}, \quad \begin{bmatrix} M(X)^\top & V_{\text{bor}} \\ W_{\text{bor}}^\top & 0_k \end{bmatrix} \begin{bmatrix} W(X) \\ \tilde{G}(X) \end{bmatrix} = \begin{bmatrix} 0_{n \times k} \\ I_k \end{bmatrix}, \quad (3.11)$$

(and assume that the matrices on the left are nonsingular). Then $G = \tilde{G}^\top$ and

$$G_X = -W^\top A_X V \quad (3.12)$$

Proof. Denote

$$N = N(X) = \begin{bmatrix} M(X) & W_{\text{bor}} \\ V_{\text{bor}}^\top & 0_k \end{bmatrix}$$

and observe that

$$G = \begin{bmatrix} 0_{k \times n} & I_k \end{bmatrix} N^{-1} \begin{bmatrix} 0_{n \times k} \\ I_k \end{bmatrix}, \quad \tilde{G} = \begin{bmatrix} 0_{k \times n} & I_k \end{bmatrix} (N^\top)^{-1} \begin{bmatrix} 0_{n \times k} \\ I_k \end{bmatrix}.$$

Because $(N^{-1})^\top = (N^\top)^{-1}$ it follows that $G = \tilde{G}^\top$.

Differentiating the system for $V(X)$ and $G(X)$ to X gives

$$M_X V + M V_X + W_{\text{bor}} G_X = 0, \quad V_{\text{bor}}^\top V_X = 0.$$

Multiplying the first equation from the left with W^\top results in

$$W^\top M_X V + W^\top M V_X + G_X = 0,$$

where it was used that $W_{\text{bor}}^\top W = I_k$. Also the system for W and \tilde{G} gives that $W^\top A = \tilde{G}^\top V_{\text{bor}}^\top$. Since we also know that $V_{\text{bor}}^\top V_X = 0$ it now follows that

$$W^\top A V_X = \tilde{G}^\top V_{\text{bor}}^\top V_X = 0.$$

The result now follows. \square

In CL_MATCONTL these bordering techniques are also applied in the context of the subspace reduction obtained from the CIS algorithm. Recall that $Q_1(s)$ is a basis for the *right* subspace corresponding to the m most critical eigenvalues. This means that rank deficiencies in M will also occur in the projection of M on the subspace Q_1 . The bordering techniques can also be applied for the reduced matrix $Q_1^\top M Q_1$, so by computing

$$\begin{bmatrix} Q_1^\top M Q_1 & \hat{w}_{\text{bor}} \\ \hat{v}_{\text{bor}}^\top & 0_k \end{bmatrix} \begin{bmatrix} \hat{v} \\ G \end{bmatrix} = \begin{bmatrix} 0_{m \times k} \\ I_k \end{bmatrix}, \quad (3.13)$$

with $\hat{v}_{\text{bor}}, \hat{w}_{\text{bor}} \in \mathbb{R}^{m \times k}$. The major difficulty that remains is how to compute G_X without using Q_{1X} . The following lemma results in a different approach for this problem than the one used in [4].

Lemma 3.4. *Bordering for subspace reduction Consider all matrices as in (3.13) and assume that the matrix on the left is nonsingular. Also assume that $\mathcal{R}(Q_1)$ is an invariant under M . Now consider*

$$\begin{bmatrix} M^\top & Q_1 \hat{v}_{\text{bor}} \\ \hat{v}_{\text{bor}}^\top Q_1^\top & 0_k \end{bmatrix} \begin{bmatrix} \hat{W} \\ \tilde{G} \end{bmatrix} = \begin{bmatrix} 0_{n \times k} \\ I_k \end{bmatrix} \quad (3.14)$$

Then the matrix on the left of (3.14) is also non-singular and $G = \tilde{G}^\top$. Also at a point X_0 for which $G(X_0) = 0$ it holds that

$$G_X(X_0) = -\hat{W} M_X Q_1 \hat{v}. \quad (3.15)$$

Proof. To see that the matrix on the left of (3.14) is non-singular, observe that it is equivalent to show that its transpose is non-singular. Now assume (for a contradiction) that there exist $V_0 \in \mathbb{R}^n$ and $G_0 \in \mathbb{R}^k$ such that

$$\begin{bmatrix} M & Q_1 \hat{w}_{\text{bor}} \\ \hat{v}_{\text{bor}}^\top Q_1^\top & 0_k \end{bmatrix} \begin{bmatrix} V_0 \\ G_0 \end{bmatrix} = \begin{bmatrix} 0_{n \times k} \\ 0_k \end{bmatrix}.$$

It follows in particular that $M V_0 = -Q_1 \hat{w}_{\text{bor}} G_0 \in \mathcal{R}(Q_1)$. Since $\mathcal{R}(Q_1)$ is an invariant subspace of M , it also follows that there exists a $\hat{v}_0 \in \mathbb{R}^m$ s.t. $M V_0 = M Q_1 \hat{v}_0$ (note that V_0 is not necessarily in $\mathcal{R}(Q_1)$). Now it is easy to see that

$$\begin{bmatrix} Q_1^\top M Q_1 & \hat{w}_{\text{bor}} \\ \hat{v}_{\text{bor}}^\top & 0_k \end{bmatrix} \begin{bmatrix} \hat{v}_0 \\ G_0 \end{bmatrix} = \begin{bmatrix} 0_{m \times k} \\ 0_k \end{bmatrix}.$$

This contradicts the assumption that the matrix on the left of (3.13) is non-singular.

Now denote $V := Q_1 \hat{v}$. Now it is easy to see that (3.13) implies that

$$\begin{bmatrix} M & Q_1 \hat{w}_{\text{bor}} \\ \hat{v}_{\text{bor}}^\top Q_1^\top & 0_k \end{bmatrix} \begin{bmatrix} V \\ G \end{bmatrix} = \begin{bmatrix} 0_{n \times k} \\ I_k \end{bmatrix}. \quad (3.16)$$

Note that the matrix on the left of this equation is the transpose of the matrix on the left of (3.13). Now the fact that $G = \tilde{G}^\top$ follows similarly as in the proof of Lemma 3.3.

For the last step, note that differentiating the first line of the system (3.16) leads to

$$M_X V + M V_X + Q_1 \hat{w}_{\text{bor}} G_X + Q_{1X} \hat{w}_{\text{bor}} G = 0 \quad (3.17)$$

The last term vanishes because $G(X_0) = 0$. Multiplying the equation from the right by W^\top gives

$$W^\top M_X V + W^\top M V_X + G_X = 0 \quad (3.18)$$

So it remains to show that $W^\top M V_X = 0$ when $G = 0$. This follows from (3.14), which gives that $M^\top W = 0$ for $G = 0$. \square

We will use the approximation for G_X in (3.15) also when $G \neq 0$. Since we are typically finding a zero of G by Newton iteration, the approximation becomes more accurate when the critical point is approached. In the implementation in CL_MATCONT, this new computation of G_X resulted in a significantly better convergence in the Newton iterations along the LP, H and BT curves.

We also need a slight modification for the continuation of the BT curve. Note that this result is only valid for $k = 1$.

Lemma 3.5 (Bordering for BT with subspace reduction). *Introduce $\hat{v}_1, \hat{v}_2 \in \mathbb{R}^m$ by*

$$\begin{bmatrix} Q_1^\top M Q_1 & \hat{w}_{\text{bor}} \\ \hat{v}_{\text{bor}}^\top & 0 \end{bmatrix} \begin{bmatrix} \hat{v}_1 \\ g_1 \end{bmatrix} = \begin{bmatrix} 0_{m \times 1} \\ 1 \end{bmatrix}, \quad \begin{bmatrix} Q_1^\top M Q_1 & \hat{w}_{\text{bor}} \\ \hat{v}_{\text{bor}}^\top & 0 \end{bmatrix} \begin{bmatrix} \hat{v}_2 \\ g_2 \end{bmatrix} = \begin{bmatrix} \hat{v}_1 \\ 0 \end{bmatrix}, \quad (3.19)$$

and assume that the borders $\hat{v}_{\text{bor}}, \hat{w}_{\text{bor}} \in \mathbb{R}^m$ are chosen such that the matrix on the right of (3.19) is nonsingular. Also assume that $\mathcal{R}(Q_1)$ is invariant under M . Now introduce $W_1, W_2 \in \mathbb{R}^n$ by

$$\begin{bmatrix} M^\top & Q_1 \hat{v}_{\text{bor}} \\ \hat{v}_{\text{bor}}^\top Q_1^\top & 0 \end{bmatrix} \begin{bmatrix} W_1 \\ \tilde{g}_1 \end{bmatrix} = \begin{bmatrix} 0_{n \times 1} \\ 1 \end{bmatrix}, \quad \begin{bmatrix} M^\top & Q_1 \hat{v}_{\text{bor}} \\ \hat{v}_{\text{bor}}^\top Q_1^\top & 0 \end{bmatrix} \begin{bmatrix} W_2 \\ \tilde{g}_2 \end{bmatrix} = \begin{bmatrix} W_1 \\ 0 \end{bmatrix}. \quad (3.20)$$

Then the matrix on the right of (3.20) is nonsingular and $g_1 = \tilde{g}_1$ and $g_2 = \tilde{g}_2$. Also when $g_1(X_0) = g_2(X_0) = 0$ it holds that

$$g_{1X}(X_0) = -W_1^\top M_X Q_1 \hat{v}_1, \quad g_{2X}(X_0) = -W_2^\top M_X Q_1 \hat{v}_1 - W_1^\top M_X Q_1 \hat{v}_2. \quad (3.21)$$

Proof. Note that the first equation in (3.19) is of the form of (3.13) and that the first equation in (3.20) is of the form (3.14). This means that we can apply Lemma 3.4 to get that the matrix on the left of (3.20) is nonsingular and that $g_1 = \tilde{g}_1$.

Now introduce $V_1 := Q_1 \hat{v}_1$ and $V_2 := Q_1 \hat{v}_2$. Because $\mathcal{R}(Q_1)$ is invariant under M it follows that

$$\begin{bmatrix} M & Q_1 \hat{v}_{\text{bor}} \\ \hat{w}_{\text{bor}}^\top Q_1^\top & 0 \end{bmatrix} \begin{bmatrix} V_1 \\ g_1 \end{bmatrix} = \begin{bmatrix} 0 \\ 1 \end{bmatrix}, \quad \begin{bmatrix} M & Q_1 \hat{v}_{\text{bor}} \\ \hat{w}_{\text{bor}}^\top Q_1^\top & 0 \end{bmatrix} \begin{bmatrix} V_2 \\ g_2 \end{bmatrix} = \begin{bmatrix} V_1 \\ 0 \end{bmatrix}. \quad (3.22)$$

Denote the matrix on the left by N . Now the equations for g_1 in (3.22) and (3.20) give

$$\begin{bmatrix} V_1 \\ 0 \end{bmatrix} = N^{-1} \begin{bmatrix} 0 \\ 1 \end{bmatrix} - g_1 \begin{bmatrix} 0 \\ 1 \end{bmatrix}, \quad \begin{bmatrix} W_1 \\ 0 \end{bmatrix} = N^{-\top} \begin{bmatrix} 0 \\ 1 \end{bmatrix} - g_1 \begin{bmatrix} 0 \\ 1 \end{bmatrix} \quad (3.23)$$

Now the equation for g_2 in (3.22) and the first equation in (3.23) result in

$$g_2 = [0 \quad 1] N^{-1} \begin{bmatrix} V_1 \\ 0 \end{bmatrix} = [0 \quad 1] N^{-2} \begin{bmatrix} 0 \\ 1 \end{bmatrix} - g_1 [0 \quad 1] N^{-1} \begin{bmatrix} 0 \\ 1 \end{bmatrix}.$$

Also, the equation for \tilde{g}_2 in (3.20) and the second equation in (3.23) give

$$\tilde{g}_2 = \begin{bmatrix} 0 & 1 \end{bmatrix} N^{-\top} \begin{bmatrix} W_1 \\ 0 \end{bmatrix} = \begin{bmatrix} 0 & 1 \end{bmatrix} N^{-2\top} \begin{bmatrix} 0 \\ 1 \end{bmatrix} - g_1 \begin{bmatrix} 0 & 1 \end{bmatrix} N^{-\top} \begin{bmatrix} 0 \\ 1 \end{bmatrix}.$$

By taking the transpose of the equation for \tilde{g}_2 it is now easy to see that $g_2 = \tilde{g}_2$.

Now we will proof (3.21). The formula for g_{1X} follows from Lemma 3.4. For the formula for g_{2X} note that (3.20) gives that $M^\top W_2 + Q_1 \hat{v}_{\text{bor}} g_2 = W_1$. Taking the transpose and differentiating w.r.t. X gives

$$W_2^\top M_X + W_{2X}^\top M + g_2 \hat{v}_{\text{bor}}^\top Q_{1X}^\top + g_{2X} \hat{v}_{\text{bor}}^\top Q_1^\top = W_{1X}^\top.$$

Multiplying from the right with V_1 results in:

$$g_{2X} = -W_2^\top M_X V_1 + W_{1X}^\top V_1. \quad (3.24)$$

Here, the second term vanishes because $MV_1 = 0$ when $g_1 = 0$, the third term vanishes because $g_2 = 0$ and the fourth term gives g_{2X} because $\hat{v}_{\text{bor}}^\top Q_1^\top V_1 = 1$.

Equation (3.20) also gives that $M^\top W_1 + Q_1 \hat{v}_{\text{bor}} g_1$. Taking the transpose and differentiating w.r.t. to X results in

$$W_{1X}^\top M + W_1^\top M_X + g_{1X} \hat{v}_{\text{bor}}^\top Q_1^\top + g_1 \hat{v}_{\text{bor}}^\top Q_{1X}^\top$$

Multiplying from the right with V_2 and using that $\hat{v}_{\text{bor}}^\top Q_1^\top V_2 = 0$ and $g_1 = 0$ gives

$$W_{1X}^\top M V_2 + W_1^\top M_X V_2 = 0. \quad (3.25)$$

For $g_2 = 0$ (3.22) gives that $V_1 = M V_2$, so that

$$W_{1X}^\top V_1 = W_{1X}^\top M V_2. \quad (3.26)$$

Using (3.26) and (3.25) in (3.24) gives

$$g_{2X} = -W_2^\top M_X V_1 - W_1^\top M_X V_2.$$

□

3.3 Equilibrium and bifurcation curves

In this section, the implementation of the curves currently supported by CL_MATCONTL are discussed. The defining systems of these curves are often defined using bordered systems, which have been discussed in Section 3.2. We will discuss equilibrium, LP, H and BT curves.

3.3.1 The equilibrium curve

The vector X and the defining system $F(X)$ for the equilibrium curve are

$$X = (u, \alpha) \in \mathbb{R}^n \times \mathbb{R}, \quad F(X) = f(u, \alpha). \quad (3.27)$$

For this curve the Jacobian matrix is simply equal to

$$F_X = \begin{bmatrix} A & f_\alpha \end{bmatrix}, \quad (3.28)$$

where $A = f_u$. The test functions are based on the matrix C as in (3.6) and the eigenvalues in $\Lambda_1 = \{\lambda_1, \lambda_2, \dots, \lambda_m\}$. The following four test functions are used along the equilibrium curve

$$\psi_1 = \lambda_{\min}(-1)^{n_u} \text{sign}(\delta), \quad \psi_2 = \lambda_{\min}(-1)^{n_u}, \quad \psi_3 = \mu_{\min}(-1)^{N_u}, \quad \psi_4 = n_u,$$

where δ is the result of the factorization

$$\begin{bmatrix} A & f_\alpha \\ \dot{u}^\top & \dot{\alpha} \end{bmatrix} = \begin{bmatrix} I & 0 \\ w^\top & 1 \end{bmatrix} \begin{bmatrix} A & b \\ 0 & \delta \end{bmatrix},$$

and

$$\begin{aligned} \lambda_{\min} &= \min_{\lambda_i \in \Lambda_1} |\lambda_i|, & n_u &= \#\{\lambda_i \in \Lambda_1 : \text{Re}(\lambda_i) > 0\}, \\ \mu_{\min} &= \min_{\lambda_i, \lambda_j \in \Lambda_1} |\lambda_i + \lambda_j|, & N_u &= \#\{\lambda_i + \lambda_j : \text{Re}(\lambda_i + \lambda_j) > 0, \lambda_i, \lambda_j \in \Lambda_1\}. \end{aligned}$$

There are (generically) three singularities that can occur along an equilibrium curve, a limit point (LP), Hopf (H) and Branching Point (BP) bifurcation. These can be detected using the above test functions as follows:

BP $\psi_1(s_k)\psi_1(s_{k+1}) < 0$,

LP $\psi_1(s_k)\psi_1(s_{k+1}) > 0$ and $\psi_2(s_k), \psi_2(s_{k+1}) < 0$,

H $\psi_3(s_k)\psi_3(s_{k+1}) < 0$ and $\psi_4(s_k) \neq \psi_4(s_{k+1})$.

Here the test function ψ_4 is different from the one used [4]. This implementation seems to more robust when the complex pair related to the Hopf bifurcation becomes real near the Hopf bifurcation (because this changes N_u but not n_u).

3.3.2 The LP curve

For the fold curve defining system $F(X)$ is defined using the bordering technique,

$$X = (u, \alpha) \in \mathbb{R}^n \times \mathbb{R}^2, \quad F(X) = \begin{pmatrix} f(u, \alpha) \\ g(u, \alpha) \end{pmatrix} \quad (3.29)$$

where $g = g(u, \alpha)$ is computed as the solution to

$$\begin{bmatrix} C & \hat{w}_{\text{bor}} \\ \hat{v}_{\text{bor}}^\top & 0 \end{bmatrix} \begin{bmatrix} v \\ g \end{bmatrix} = \begin{bmatrix} 0 \\ 1 \end{bmatrix}. \quad (3.30)$$

The borders must be selected such that the matrix in the LHS of (3.30) is nonsingular. To apply Newton iteration the Jacobian matrix is computed as

$$F_X = \begin{bmatrix} A & f_\alpha \\ g_u & g_\alpha \end{bmatrix}, \quad (3.31)$$

where g_u and g_α follow from Lemma 3.4 with $M = A$ as

$$g_u = -W^\top A_u Q \hat{v}, \quad g_\alpha = -W^\top A_\alpha Q \hat{v}. \quad (3.32)$$

and W is computed using Lemma 3.4 with $M = A$ as

$$\begin{bmatrix} A^\top & Q \hat{v}_{\text{bor}} \\ \hat{w}_{\text{bor}}^\top Q^\top & 0 \end{bmatrix} \begin{bmatrix} W \\ g \end{bmatrix} = \begin{bmatrix} 0 \\ 1 \end{bmatrix}. \quad (3.33)$$

At the LP curve also the normal form coefficient a is computed as

$$a_{LP} = \frac{1}{2} W^\top B(Q_1 \hat{v}, Q_1 \hat{v}). \quad (3.34)$$

In the computation of the testfunctions we do not want to consider the eigenvalue that is zero along the LP curve. Therefore introduce:

$$\Lambda'_1 = \{\lambda \in \Lambda_1 : \text{Re}(\lambda) \neq 0\}. \quad (3.35)$$

The testfunctions now computed as

$$\psi_1 = \hat{w}^\top \hat{v}, \quad \psi_2 = a_{LP}, \quad \psi_3 = \mu_{\min}(-1)^{N_u}, \quad \psi_4 = n'_u,$$

where

$$n'_u = \#\{\lambda \in \Lambda'_1 | \text{Re}(\lambda_i) > 0\}$$

$$\mu_{\min} = \min_{\lambda_i, \lambda_j \in \Lambda'_1} |\lambda_i + \lambda_j|, \quad N_u = \#\{\lambda_i + \lambda_j : \text{Re}(\lambda_i + \lambda_j) > 0, \lambda_i, \lambda_j \in \Lambda'_1\}.$$

The three singularities that generically occur are the Bogdanov-Takens (BT), Zero-Hopf (ZH) and Cusp (CP) bifurcation. These are detected as follows:

BT $\psi_1(s_k)\psi_1(s_{k+1}) < 0$,

CP $\psi_2(s_k)\psi_2(s_{k+1}) < 0$,

ZH $\psi_1(s_k)\psi_1(s_{k+1}) > 0$ and $\psi_3(s_k)\psi_3(s_{k+1}) < 0$ and $\psi_4(s_k) \neq \psi_4(s_{k+1})$.

The detection of the Zero-Hopf bifurcation was modified similarly as for the Hopf bifurcation on the equilibrium curve.

3.3.3 The H curve

For the defining system of the Hopf curve an additional parameter κ is introduced. The defining system is

$$X = (u, \alpha, \kappa) \in \mathbb{R}^n \times \mathbb{R}^2 \times \mathbb{R}, \quad F(X) = \begin{pmatrix} f(u, \alpha) \\ g_{i_1 j_1}(u, \alpha, \kappa) \\ g_{i_2 j_2}(u, \alpha, \kappa) \end{pmatrix}, \quad (3.36)$$

where the g_{ij} , $i, j \in \{1, 2\}$ are solutions of

$$\begin{bmatrix} C^2 + \kappa I_m & \hat{w}_{1, \text{bor}} & \hat{w}_{1, \text{bor}} \\ \hat{v}_{1, \text{bor}}^\top & 0 & 0 \\ \hat{v}_{2, \text{bor}}^\top & 0 & 0 \end{bmatrix} \begin{bmatrix} \hat{v}_1 & \hat{v}_2 \\ g_{11} & g_{12} \\ g_{21} & g_{22} \end{bmatrix} = \begin{bmatrix} 0 & 0 \\ 1 & 0 \\ 0 & 1 \end{bmatrix}. \quad (3.37)$$

The borders are again selected such that the matrix is non-singular. The coefficients i_1, j_1, i_2 and j_2 are selected such that the condition number of the matrix on the left of (3.37) is the smallest. The Jacobian becomes

$$F_X = \begin{bmatrix} A & f_\alpha & 0 \\ g_{i_1 j_1, u} & g_{i_1 j_1, \alpha} & g_{i_1 j_1, \kappa} \\ g_{i_2 j_2, u} & g_{i_2 j_2, \alpha} & g_{i_2 j_2, \kappa} \end{bmatrix} \quad (3.38)$$

The derivatives of $g_{i_1 j_1}$ and $g_{i_2 j_2}$ are again computed using Lemma 3.4 with $M = A^2 + \kappa I$. This gives

$$g_{ij, u} = -W_i^\top (A A_u + A_u A) Q \hat{v}_j, \quad g_{ij, \alpha} = -W_i^\top (A A_\alpha + A_\alpha A) Q \hat{v}_j, \quad g_{ij, \kappa} = -W_i^\top Q \hat{v}_j \quad (3.39)$$

where W_i is computed by solving

$$\begin{bmatrix} (A^2 + \kappa I_n)^\top & Q \hat{v}_{1, \text{bor}} & Q \hat{v}_{1, \text{bor}} \\ \hat{w}_{1, \text{bor}}^\top Q^\top & 0 & 0 \\ \hat{w}_{2, \text{bor}}^\top Q^\top & 0 & 0 \end{bmatrix} \begin{bmatrix} W_1 & W_2 \\ g_{11} & g_{21} \\ g_{12} & g_{22} \end{bmatrix} = \begin{bmatrix} 0 & 0 \\ 1 & 0 \\ 0 & 1 \end{bmatrix}. \quad (3.40)$$

The vectors q_0 and p_0 needed for the first Lyapunov coefficient l_1 in (2.16) can also be computed from (3.40) as

$$q_0 = Q(\alpha_1 \hat{v}_1 + \alpha_2 \hat{v}_2), \quad p_0 = \beta_1 W_1 + \beta_2 W_2, \quad (3.41)$$

where

$$\alpha_1 = \hat{v}_1^\top C \hat{v}_2 - i\omega \hat{v}_1^\top \hat{v}_2, \quad \alpha_2 = -\hat{v}_1^\top C \hat{v}_1 + i\omega \hat{v}_1^\top \hat{v}_1, \quad (3.42)$$

$$\beta_1 = W_1^\top A^\top W_2 + i\omega W_1^\top W_2, \quad \beta_2 = -W_1^\top A^\top W_1 - i\omega W_1^\top W_1. \quad (3.43)$$

The testfunctions are

$$\psi_1 = \kappa, \quad \psi_2 = l_1, \quad \psi_3 = \lambda'_{\min}(-1)^{n'_u}, \quad \psi_4 = \mu_{\min}(-1)^{N_u}, \quad \psi_5 = n'_u,$$

where

$$\lambda'_{\min} = \min_{\lambda_i \in \Lambda'_1} |\lambda_i| \quad n'_u = \#\{\lambda \in \Lambda'_1 | \text{Re}(\lambda_i) > 0\}$$

$$\mu_{\min} = \min_{\lambda_i, \lambda_j \in \Lambda'_1} |\lambda_i + \lambda_j|, \quad N_u = \#\{\lambda_i + \lambda_j : \text{Re}(\lambda_i + \lambda_j) > 0, \lambda_i, \lambda_j \in \Lambda'_1\},$$

and Λ'_1 is defined as in (3.35). The three singularities that generically occur are the Bogdanov-Takens (BT), Double Hopf (DH) and Generalized Hopf (GH) bifurcation. These are detected as:

BT $\psi_1(s_k)\psi_1(s_{k+1}) < 0$,

GH $\psi_2(s_k)\psi_2(s_{k+1}) < 0$ and $\psi_3(s_k)\psi_3(s_{k+1}) > 0$,

ZH $\psi_1(s_k)\psi_1(s_{k+1}) > 0$ and $\psi_3(s_k)\psi_3(s_{k+1}) < 0$,

DH $\psi_4(s_k)\psi_4(s_{k+1}) < 0$ and $\psi_5(s_k) \neq \psi_5(s_{k+1})$.

The detection of the Double Hopf point was again modified similar as for the Hopf bifurcation on the equilibrium curve.

3.3.4 The BT curve

The defining system for the continuation of the Bogdanov-Takens bifurcation was originally not implemented in CL_MATCONT. The idea for the implementation comes from [13]. The continuation of BT bifurcations is also not implemented in ‘standard’ version CL_MATCONT [6], but was implemented in CONTENT [12]. The approach we describe is an extension of these implementation because we use subspace reduction.

The defining system for the BT curve becomes

$$X = (u, \alpha) \in \mathbb{R}^n \times \mathbb{R}^3, \quad F(X) = \begin{pmatrix} f(u, \alpha) \\ g_1(u, \alpha) \\ g_2(u, \alpha) \end{pmatrix} \quad (3.44)$$

where g_1 is the solution of

$$\begin{bmatrix} C & \hat{w}_{\text{bor}} \\ \hat{v}_{\text{bor}}^\top & 0 \end{bmatrix} \begin{bmatrix} \hat{v}_1 \\ g_1 \end{bmatrix} = \begin{bmatrix} 0 \\ 1 \end{bmatrix}, \quad (3.45)$$

and g_2 is the solution of

$$\begin{bmatrix} C & \hat{w}_{\text{bor}} \\ \hat{v}_{\text{bor}}^\top & 0 \end{bmatrix} \begin{bmatrix} \hat{v}_2 \\ g_2 \end{bmatrix} = \begin{bmatrix} \hat{v}_1 \\ 0 \end{bmatrix}. \quad (3.46)$$

The Jacobian matrix of the system is

$$F_X = \begin{bmatrix} A & f_\alpha \\ g_{1,x} & g_{1,\alpha} \\ g_{2,x} & g_{2,\alpha} \end{bmatrix} \quad (3.47)$$

The derivatives of g_1 and g_2 are computed from Lemma 3.5 as

$$g_{1,x} = -W_1^\top A_x Q \hat{v}_1, \quad g_{2,x} = -W_2^\top A_x Q \hat{v}_1 - W_1^\top A_x Q \hat{v}_2, \quad (3.48)$$

$$g_{1,\alpha} = -W_1^\top A_\alpha Q \hat{v}_1, \quad g_{2,\alpha} = -W_2^\top A_\alpha Q \hat{v}_1 - W_1^\top A_\alpha Q \hat{v}_2. \quad (3.49)$$

where W_1 and W_2 are computed as

$$\begin{bmatrix} A^\top & Q \hat{v}_{\text{bor}} \\ \hat{w}_{\text{bor}}^\top Q^\top & 0 \end{bmatrix} \begin{bmatrix} W_1 \\ g_1 \end{bmatrix} = \begin{bmatrix} 0 \\ 1 \end{bmatrix}, \quad (3.50)$$

$$\begin{bmatrix} A^\top & Q \hat{v}_{\text{bor}} \\ \hat{w}_{\text{bor}}^\top Q^\top & 0 \end{bmatrix} \begin{bmatrix} W_2 \\ g_2 \end{bmatrix} = \begin{bmatrix} W_1 \\ 0 \end{bmatrix}. \quad (3.51)$$

The following testfunctions are used

$$\psi_1 = a_2 \quad \psi_2 = b_2 \quad \psi_3 = \lambda'_{\min}(-1)^{n'_u} \quad \psi_4 = \mu_{\min}(-1)^{N_u}, \quad \psi_5 = n'_u,$$

where λ'_{\min} , n'_u , and N'_u are defined similar as for the H curve. There are four possible codimension-3 degeneracies [12]. These involve the codimension-3 degeneracies in Section 2.3. Also the situation that A has a 3×3 Jordan block ('triple zero') and case that an additional complex pair crosses the imaginary axis are detected. The degeneracies are detected as

$$\mathbf{BTa2} \quad \psi_1(s_k)\psi_1(s_{k+1}) < 0 \text{ and } \psi_3(s_k)\psi_3(s_{k+1}) > 0 \text{ and } \psi_4(s_k)\psi_4(s_{k+1}) > 0,$$

$$\mathbf{BTb2} \quad \psi_2(s_k)\psi_2(s_{k+1}) < 0 \text{ and } \psi_3(s_k)\psi_3(s_{k+1}) > 0 \text{ and } \psi_4(s_k)\psi_4(s_{k+1}) > 0,$$

$$\mathbf{BT3} \quad \psi_3(s_k)\psi_3(s_{k+1}) < 0.$$

$$\mathbf{BTH} \quad \psi_4(s_k)\psi_4(s_{k+1}) < 0 \text{ and } \psi_5(s_k) \neq \psi_5(s_{k+1}).$$

The normal form coefficients a_2 and b_2 are computed by setting

$$q_0 = Q_1 \hat{v}_1, \quad q_1 = Q_1 \hat{v}_2, \quad p_1 = W_1, \quad p_0 = W_2,$$

and using the normalization procedure in [20, Appendix A].

Also the computation of the normal form coefficient a_3 , b_3 , a_4 and b_4 has been implemented using the formulas like (2.26) and (2.27) from [20].

Chapter 4

The PDE system

This chapter studies the PDE model of the fusion plasma proposed by Zohm [27]. In Section 4.1, the model is introduced with a (short) physical motivation. In Section 4.2, the steady-state solutions of the systems are studied, which leads to analytic criteria for the fold and cusp bifurcations. A more extensive analytic approach can be found in [5].

4.1 L–H transition models

In this section we introduce a simplified PDE-model in one spatial dimension that shows L-mode and H-mode behavior. The model was originally proposed by Zohm [27] and was studied in [22] and [25].

The most successful fusion devices are TOKAMAKS. In this concept the plasma is confined by means of a magnetic field. The magnetic field is configured in such a way that the magnetic field lines lie on nested tori, as indicated in Figure 4.1. Particles can move freely on along the different torus shaped surfaces, but the transport between the different surfaces is very limited. Therefore physical quantities like density and temperature can be considered constant on each surface. This motivates that the model contains only the radial distance as spatial dimension. At the outside of the tori magnetic field lines are diverted into an exhaust. This leads to the presence of a scrape-off layer.

The general form of the LH transition models is

$$\frac{\partial n}{\partial t} = -\frac{\partial \Gamma}{\partial x} \quad \Gamma = -D(Z) \frac{\partial n}{\partial x}, \quad (4.1)$$

$$\frac{\partial U}{\partial t} = -\frac{\partial q}{\partial x} \quad q = -\chi(Z)n \frac{\partial T}{\partial x} + \frac{\Gamma T}{\gamma - 1}, \quad (4.2)$$

$$\varepsilon \frac{\partial Z}{\partial t} = \mu \frac{\partial^2 Z}{\partial x^2} + c_n \frac{T}{n^2} \frac{\partial n}{\partial x} + \frac{c_T}{n} \frac{\partial T}{\partial x} + G(Z). \quad (4.3)$$

The spatial coordinate x represents radial coordinate in the (torus shaped) volume occupied by the plasma. Geometric effects originating from the curvature of the torus shaped surfaces have been neglected, because their effect near the plasma edge is small. In particular, the gradient operator is approximated by $\frac{\partial}{\partial x}$ and the radial coordinate x is chosen such that the plasma edge is located at $x = 0$ and the plasma core at $x = +\infty$.

The variables in the model represent the particle density n , the internal energy U , and the radial electric field or poloidal rotation Z . The temperature T is related to internal energy U by

$$T = (\gamma - 1) \frac{U}{n}, \quad (4.4)$$

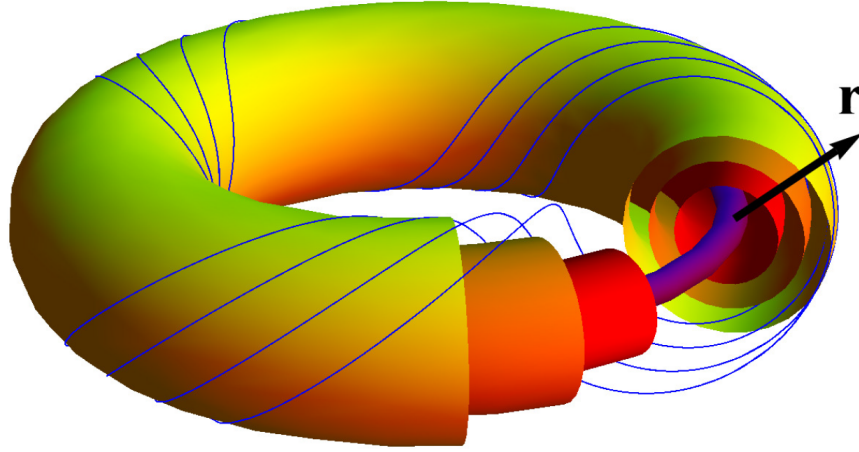


Figure 4.1: Torus shaped surfaces in the TOKAMAK concept

where γ represents the adiabatic index.

Equation (4.1) describes the transport of particles (between the different torus shaped surfaces). The particle flux Γ is related to the density gradient by a diffusivity D . Note that the diffusivity depends on the radial electric field Z . This models that the transport of particles is mainly driven by turbulence.

Equation (4.2) describes the transport of energy. In the heat flux q transport by conduction and advection are considered. Here $\chi(Z)$ represents the (heat) conductivity of the plasma, which is also dependent on Z . In particular it will be used that

$$\chi(Z) = \frac{1}{(\gamma - 1)\zeta} D(Z), \quad (4.5)$$

where ζ is some proportionality factor.

Equation (4.3) describes the evaluation of the radial electric field. Ampere's law relates the time derivative of Z to radial currents. The first term of the RHS of (4.3) incorporates viscous effects caused by the $E \times B$ flows. The second and third terms account for currents caused by differences between ion and electron behavior. The term $G(Z)$ incorporates the effects of many other physical mechanisms [25, Appendix 6.A]. The third order Taylor expansion of G will always be of the form

$$G(Z) = a - b(Z - Z_S) - (Z - Z_S)^3. \quad (4.6)$$

The function $G(Z)$ is plotted in Figure 4.2a.

For the diffusivity function $D(Z)$ we use the function proposed by [27]

$$D(Z) = D_0 + D_1 \tanh(Z). \quad (4.7)$$

For physical meaningful results the values of D_0 and D_1 should be chosen such that $D(Z) > 0$ for all Z . The function $D(Z)$ is plotted in Figure 4.2b.

It should be noted that more realistic models use a diffusivity that will (also) depend on $\partial Z / \partial x$. The model (4.1)–(4.3) has been studied for other choices of $D(Z)$ by time simulations in [25] [22].

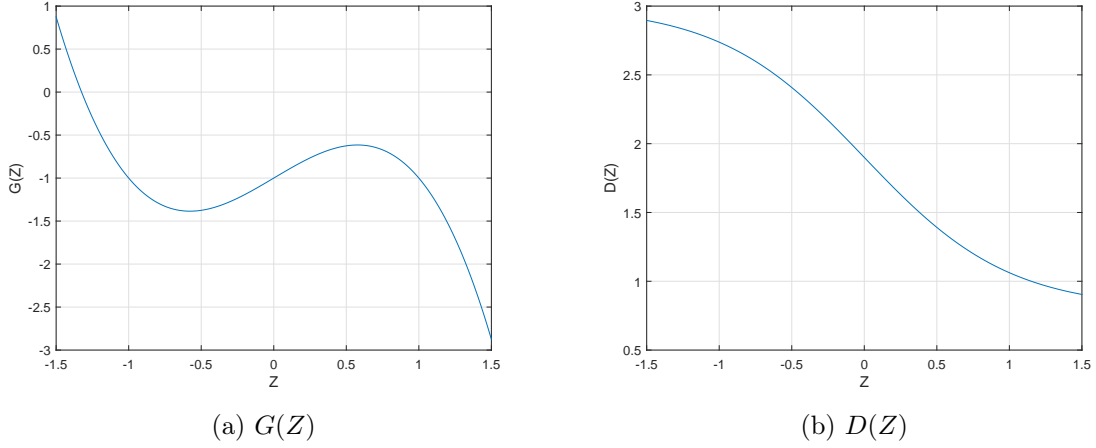


Figure 4.2: The functions $G(Z)$ and $D(Z)$ at the standard parameter values.

The boundary conditions at the plasma core ($x = \infty$) are

$$\Gamma|_{x=\infty} = \Gamma_\infty, \quad q|_{x=\infty} = q_\infty, \quad \left. \frac{\partial Z}{\partial x} \right|_{x=\infty} = 0. \quad (4.8)$$

The fluxes Γ_∞ and q_∞ account for the particles and heat added to the plasma. In reality, particles and heat will be added to a volume of the plasma. Because we are only interested in the behavior near the boundary, this effect is neglected.

The boundary conditions at the edge of the plasma $x = 0$ are

$$\left. \frac{\partial n}{\partial x} \right|_{x=0} = \frac{n}{\lambda_n}, \quad \left. \frac{\partial T}{\partial x} \right|_{x=0} = \frac{T}{\lambda_T}, \quad \left. \frac{\partial^2 Z}{\partial x^2} \right|_{x=0} = 0. \quad (4.9)$$

The boundary conditions for n and T model the scrape-off layer at the edge of the plasma. The boundary condition for Z was originally proposed by Zohm in [27], but different boundary conditions for Z have also been studied in [25] and [22].

Table 4.1 shows the standard parameter values. Unless otherwise stated the results in this thesis will be presented for these parameter values. Note that particles and heat will flow from the plasma core to the plasma edge (in the situation where the fusion reactor delivers power), resulting in negative values for the particle flux Γ_∞ and heat flux q_∞ .

Table 4.1: Standard parameter values

Parameter	Value
γ	$\frac{5}{3}$
ε	0.05
μ	0.05
c_n	1.1
c_T	0.9
ζ	1.1
a	-1
b	-1
Z_S	0
Γ_∞	-0.8
q_∞	-1
λ_n	1.25
λ_T	1.5
D_0	1.9
D_1	-1.1

4.2 Steady-state solutions

In this section we will study the steady states of the model introduced in the previous section. The steady-state solutions of (4.1) – (4.3) are denoted by \tilde{n} , \tilde{U} , \tilde{T} and \tilde{Z} . Note that these will only depend on x .

The steady states \tilde{n} and \tilde{T} can be expressed in terms of \tilde{Z} as,

$$\tilde{n}(x) = n_0 - \Gamma_\infty \int_0^x \frac{dx'}{D(\tilde{Z}(x'))}, \quad (4.10)$$

$$\tilde{T}(x) = T_\infty + (T_0 - T_\infty) \left(\frac{n(x)}{n_0} \right)^{-\zeta}, \quad (4.11)$$

where

$$n_0 = -\frac{\Gamma_\infty \lambda_n}{D(Z_0)} \quad T_\infty = (\gamma - 1) \frac{q_\infty}{\Gamma_\infty} \quad T_0 = \frac{T_\infty}{1 + \lambda_n/(\lambda_T \zeta)},$$

and $Z_0 = Z(x = 0)$. It should be noted that the derivation of (4.11) relies strongly on the form the conductivity in (4.5). By using (4.10) and (4.11), equation (4.3) can be rewritten as for the steady-state solution \tilde{Z} as

$$-\mu \frac{\partial^2 \tilde{Z}(x)}{\partial x^2} = -\frac{T_\infty \Gamma_\infty}{\tilde{n}(x)^2 D(\tilde{Z}(x))} \left(c_n + c_g \left(\frac{\tilde{n}(x)}{n_0} \right)^{-\zeta} \right) + G(\tilde{Z}(x)), \quad (4.12)$$

where

$$c_g = \frac{\zeta c_T - c_n}{1 + \zeta \lambda_T / \lambda_n}.$$

Appendix A provides a method to construct an approximate solution of (4.12).

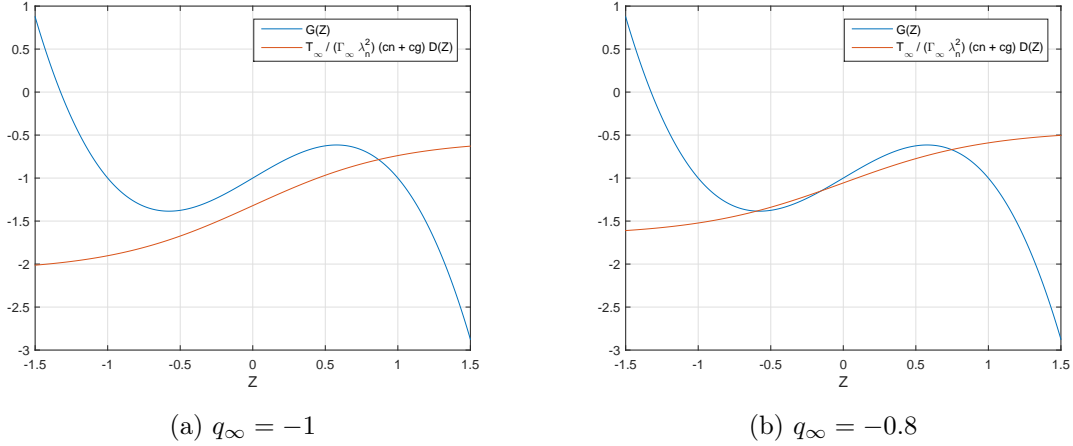


Figure 4.3: Equation (4.13) typically has one or three solutions for Z_0

Evaluating this equation at $x = 0$ and using the boundary condition for Z in (4.9), we find the following equation for $Z_0 := \tilde{Z}(x = 0)$,

$$-\frac{T_\infty}{\Gamma_\infty \lambda_n^2} (c_n + c_g) D(Z_0) + G(Z_0) = 0. \quad (4.13)$$

Here, also the definition of n_0 below (4.11) was used. Equation (4.13) typically has one or three solutions, as is illustrated by Figure 4.3

Next, we consider the (4.12) for $x \rightarrow \infty$. Note that the form of $D(Z)$ in (4.7) allows to determine constants D_{\min} and D_{\max} such that for all $Z \in \mathbb{R}$,

$$0 < D_{\min} \leq D(Z) \leq D_{\max}. \quad (4.14)$$

Using this in (4.10) it follows that

$$\tilde{n}(x) \geq n_0 - \frac{\Gamma_\infty}{D_{\max}} x. \quad (4.15)$$

It is now easy to see that the first term on the RHS of (4.12) will converge to zero for $x \rightarrow \infty$. Further observe that the boundary condition for Z in (4.8) also implies that

$$\left. \frac{\partial^2 Z}{\partial x^2} \right|_{x=\infty} = 0. \quad (4.16)$$

When we also use this observation in (4.12), we find that $Z_\infty := \tilde{Z}(x \rightarrow \infty)$ must satisfy

$$G(Z_\infty) = 0. \quad (4.17)$$

We now expect the following result (which comes without proof).

Lemma 4.1. *For every solution Z_0 of (4.13) and every solution Z_∞ of (4.17), (4.12) with \tilde{n} as in (4.10) has a (unique?) solution \tilde{Z} satisfying*

$$\tilde{Z}(x = 0) = Z_0, \quad \tilde{Z}(x \rightarrow \infty) = Z_\infty. \quad (4.18)$$

$G(Z)$ has only one (real) root, precisely when

$$b < -\left(\frac{|a|}{2}\right)^{\frac{2}{3}}. \quad (4.19)$$

When $G(Z)$ has only one (real) root, Lemma 4.1 asserts that the roots Z_0 of (4.13) correspond steady-state solutions. This means that when (4.19) holds, a fold occurs bifurcation when (4.13) has a double root, so when there exists a value of Z_0 such that

$$-\frac{T_\infty}{\Gamma_\infty \lambda_n^2}(c_n + c_g)D(Z_0) + G(Z_0) = 0, \quad \frac{d}{dZ} \left(\frac{G}{D} \right) \Big|_{Z=Z_0} = 0. \quad (4.20)$$

The cusp bifurcation is characterized by a triple zero of (4.13), so by

$$-\frac{T_\infty}{\Gamma_\infty \lambda_n^2}(c_n + c_g)D(Z_0) + G(Z_0) = 0, \quad \frac{d}{dZ} \left(\frac{G}{D} \right) \Big|_{Z=Z_0} = 0, \quad \frac{d^2}{dZ^2} \left(\frac{G}{D} \right) \Big|_{Z=Z_0} = 0. \quad (4.21)$$

Chapter 5

Discretization

In this chapter, the spatial discretization of the PDE system introduced in Chapter 4 is developed. The discretization will be made on a non-uniform grid. In Section 5.1 two different discretization methods (finite difference and finite volume) are compared. Section 5.2 deals with the distribution of the grid points.

The spatial discretization of the system in Chapter 4 formed an important part of the work by Paquay in [22]. He started from (rather fine) uniform grid. When large values of the gradients $\partial n/\partial x$, $\partial T/\partial x$ or $\partial Z/\partial x$ were found during time integration, additional gridpoints were introduced. The introduction of new gridpoints makes this approach not suitable for numerical continuation. We therefore develop a new discretization method in this chapter.

5.1 Two discretization methods

To obtain a discretization of (4.1)–(4.3) the spatial domain $[0, \infty)$ is truncated to a finite domain $[0, L]$. On this domain a grid consisting of $N + 1$ points is introduced as

$$\Theta := \{0 = x_0 < x_1 < x_2 < \dots < x_{N-1} < x_N = L\}. \quad (5.1)$$

Also the grid spacing h_i and maximal grid spacing h are introduced as

$$h_i = x_i - x_{i-1}, \quad h = \max h_i \quad 1 \leq i \leq N \quad (5.2)$$

Figure 5.1 shows a typical steady-state profile, computed for the discretization on a uniform grid developed by [22]. Intuitively, it is clear that near the boundary $x = 0$ more grid points are needed than in the rest of the profile. Therefore a non-uniform grid will be used. Different methods are available to approximate a (system of) PDEs by a system of ODEs. Most well known methods are the Finite Difference Method (FDM) and the Finite Volume Method (FVM) [16]. Both methods have been used to obtain a discretization of the system (4.1) – (4.3). In Section 5.1.3 both methods are compared.

For both methods approximations of the 1st and 2nd order spatial derivatives in the grid points $x = x_i$ are needed. We use three-point formulas as in [21] [13],

$$\left. \frac{\partial n}{\partial x} \right|_{x=x_i} \approx \frac{\partial n_i}{\partial x} = \varphi_i^{-1} n_{i-1} + \varphi_i^0 n_i + \varphi_i^1 n_{i+1}, \quad (5.3)$$

$$\left. \frac{\partial^2 n}{\partial x^2} \right|_{x=x_i} \approx \frac{\partial^2 n_i}{\partial x^2} = \psi_i^{-1} n_{i-1} + \psi_i^0 n_i + \psi_i^1 n_{i+1}, \quad (5.4)$$

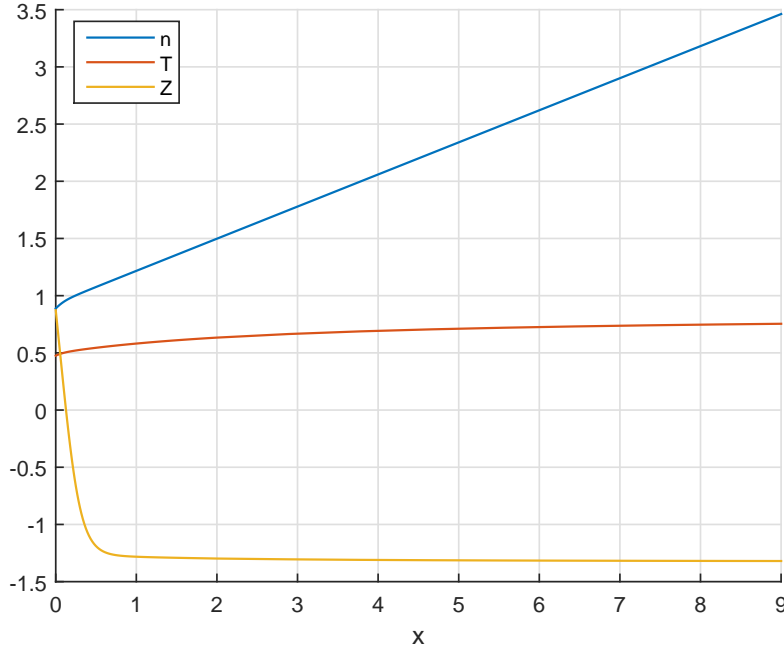


Figure 5.1: Typical steady-state solution of the PDE system at the standard parameter values

where

$$\begin{aligned}\varphi_i^{-1} &= \frac{2h_i + h_{i+1}}{3h_i(h_i + h_{i+1})}, & \varphi_i^0 &= \frac{h_{i+1} - h_i}{3h_i h_{i+1}}, & \varphi_i^1 &= \frac{h_i + 2h_{i+1}}{3h_i(h_i + h_{i+1})}, \\ \psi_i^{-1} &= \frac{2}{h_i(h_i + h_{i+1})}, & \psi_i^0 &= -\frac{2}{h_i h_{i+1}}, & \psi_i^1 &= \frac{2}{h_i(h_i + h_{i+1})}.\end{aligned}$$

The same formulas can also be used for U and Z .

5.1.1 Finite Difference Method

For the finite difference method formulas the unknowns are the pointwise values of the function. In particular there are $3(N - 1)$ unknowns are

$$n_i = n(x_i), \quad U_i = U(x_i), \quad Z_i = Z(x_i), \quad 1 \leq i \leq N - 1. \quad (5.5)$$

Note also that T_i can be computed using (4.4) as

$$T_i := (\gamma - 1) \frac{U_i}{n_i},$$

and that the values in $x_0 = 0$ and $x_N = L$ will be computed from the other unknowns using the boundary conditions. To obtain a discretization of (4.1) note that

$$\frac{\partial n}{\partial t} = \frac{\partial}{\partial x} \left(D(Z) \frac{\partial n}{\partial x} \right) = D(Z) \frac{\partial^2 n}{\partial x^2} + \frac{\partial D}{\partial Z} \frac{\partial Z}{\partial x} \frac{\partial n}{\partial x} \quad (5.6)$$

When (5.6) is evaluated at $x = x_i$ the LHS becomes $\partial n_i / \partial t$. At the RHS the derivative $\partial D / \partial Z$ can be computed symbolically from (4.7) and that the derivatives of n and Z can be approximated by the formulas (5.3) and (5.4). So the resulting discretization of (4.1) becomes

$$\frac{\partial n_i}{\partial t} = D(Z_i) \frac{\partial^2 n_i}{\partial x^2} + \left. \frac{\partial D}{\partial Z} \right|_{Z=Z_i} \frac{\partial Z_i}{\partial x} \frac{\partial n_i}{\partial x}. \quad (5.7)$$

Formulas for the discretization of (4.2) and (4.3) can be found in Appendix B.1.

5.1.2 Finite Volume Method

The finite volume method is especially designed for equations of the form

$$\frac{\partial u}{\partial t} = - \frac{\partial f}{\partial x}. \quad (5.8)$$

The conservative properties of (5.8) are not preserved when the FDM is used. The FVM preserves these properties. Note that (4.1) and (4.2) are of this form, but that (4.3) is not of this form. Therefore, the FVM is not used for Z . The $3N - 1$ unknowns in this discretization are now

$$\bar{n}_i = \int_{x_{i-1}}^{x_i} n(x') dx', \quad \bar{U}_i = \int_{x_{i-1}}^{x_i} U(x') dx', \quad 1 \leq i \leq N \quad (5.9)$$

$$Z_i = Z(x_i) \quad 1 \leq i \leq N - 1 \quad (5.10)$$

To obtain a discretization of (4.1), we integrate from x_{i-1} to x_i and obtain

$$\frac{\partial \bar{n}_i}{\partial t} = - \frac{\Gamma_i - \Gamma_{i-1}}{h_i} \quad (5.11)$$

where $\Gamma_i = \Gamma|_{x=x_i}$. Note that in order to compute Γ_i an approximation of $\partial n / \partial x$ is needed in terms of $\bar{n}(i)$, so (5.3) cannot be used directly here. To solve this problem we introduce

$$n^{tot}(x) := \int_0^x n(x') dx' \quad U^{tot}(x) := \int_0^x U(x') dx'.$$

Note that n^{tot} and U^{tot} can be computed in the gridpoints x_i as

$$n_i^{tot} = \int_0^{x_i} n(x') dx' = \sum_{j=1}^i \bar{n}_j, \quad U_i^{tot} = \int_0^{x_i} U(x') dx' = \sum_{j=1}^i \bar{U}_j.$$

Now observe that Γ_i can be computed as

$$\Gamma_i := -D(Z_i) \frac{\partial^2 n_i^{tot}}{\partial x^2}, \quad (5.12)$$

where the second derivative of n_i^{tot} can be computed using (5.3). Note that also the pointwise value $Z|_{x=x_i}$ is needed, which would not be available when also cell averages for Z would have been defined. Formulas for the discretization of (4.2) and (4.3) can be found in Appendix B.2.

Table 5.1: The value of q_∞ at the Hopf bifurcation using FDM and FVM on various Θ_N^m -grids

m	N	FDM	FVM
1	50	-2.387528	-1.679282
	100	-1.558038	-1.121807
2	30	-0.9119245	-0.9011258
	50	-0.8519563	-0.8474858
	100	-0.8266519	-0.8252153
3	30	-0.8230483	-0.8190848
	50	-0.8193174	no convergence
	100	-0.8183742	no convergence
4	30	no convergence	no convergence

5.1.3 Comparison

It turns out that when a the steady state in Figure 5.1 is continued in q_∞ , two Hopf-bifurcations are found. The location of the first H-bifurcation is used to measure the accuracy of the discretization. Table 5.1 shows the position of Hopf-bifurcation for different grids. Here we use very basic grids of the form

$$\Theta_N^m := \left\{ x_i \mid x_i = L \left(\frac{i}{N} \right)^m, i = 0, \dots, N \right\}. \quad (5.13)$$

Note that for $m = 1$ the grid is uniformly distributed ($h_i = h = \text{const}$) and that for $m > 1$ the grid points will accumulate near $x = 0$.

The results in Table 5.1 show that the FVM is more accurate than the FDM on the uniform grid ($m = 1$). For the quadratic grid ($m = 2$) there is almost no difference between the results for the FVM and the FDM. For the cubic grid ($m = 3$) some problems occur during the continuation. These problems probably originate from the very small grid spacing near $x = 0$. The FDM does not encounter such difficulties for $m = 3$. For $m = 4$ both methods show numerical instabilities.

Also note that for all grids in Table 5.1 the value of q_∞ increases when the number of gridpoints N is increased, suggesting that higher values of q_∞ will be more accurate. This suggest that accuracy on the quadratic and cubic grid is much better than on the uniform grid. Also note that the difference in accuracy between the FDM and the FVM is relatively small compared to this. So the distribution of the grid points is more important than the used discretization method.

Also observe that the for the FDM $\partial n_i / \partial t$, $\partial U_i / \partial t$ and $\partial Z_i / \partial t$ depends only on the values of n , U and Z in x_{i-1} , x_i and x_{i+1} , while for the FVM these depend on n , U and Z in all x_j for $j \leq i + 1$. This means that the Jacobian matrix A ($A = f_u$ with f as in (2.1)) will have a clear band structure when the FDM is used. For the FVM the Jacobian matrix A will be a (less sparse) lower triangular matrix.

Although the FVM is slightly more accurate, the FDM seems numerically more stable. Since the grid distribution seems to be more important than the discretization method, this seems to be an important consideration. Also a sparser structure of Jacobian matrix A can be beneficial for large N . Because of these considerations the FDM will be used.

5.2 Grid distribution

In the previous section, a discretization method on a nonuniform grid Θ has been developed. In this section, the distribution of the gridpoints x_i will be addressed.

The error in the approximations (5.3) and (5.4) also creates an error in the formulas like (5.7). Intuitively, we want to minimize the error in the spatial discretization. To make this idea more clear, introduce $R_n^{(1)}(i)$ and $R_n^{(2)}(i)$ by

$$\left. \frac{\partial n}{\partial x} \right|_{x=x_i} = \frac{\partial n_i}{\partial x} + R_n^{(1)}(i), \quad \left. \frac{\partial^2 n}{\partial x^2} \right|_{x=x_i} = \frac{\partial^2 n_i}{\partial x^2} + R_n^{(2)}(i). \quad (5.14)$$

Similarly $R_U^{(1)}(i)$, $R_U^{(2)}(i)$, $R_Z^{(1)}(i)$ and $R_Z^{(2)}(i)$ can be introduced for U and Z . The local error in the discretization is a combination of these. For example the error in (5.7) can be expressed in $R_n^{(1)}(i)$, $R_n^{(2)}(i)$ and $R_Z^{(1)}(i)$ as

$$D(Z_i)R_n^{(2)}(i) + \left. \frac{\partial D}{\partial Z} \right|_{Z=Z_i} \left(\frac{\partial Z_i}{\partial x} R_n^{(1)}(i) + R_Z^{(1)}(i) \frac{\partial n_i}{\partial x} + R_Z^{(1)}(i) R_n^{(1)}(i) \right).$$

For the other two equations the same principle applies, but equations become very long. Ideally, the grid should be distributed in such a way that these error are minimized. However, it practically not feasible to do this. An alternative approach would be to minimize the leading terms in the errors $R_{n,U,Z}^{(1,2)}(i)$. In Appendix B.3, it is shown that the leading terms in the error are,

$$R_n^{(1)}(i) = \left. \frac{1}{18} \frac{\partial^3 n}{\partial x^3} \right|_{x=\tilde{x}_i} (h_i^2 + h_i h_{i+1} + h_{i+1}^2) + \left. \frac{1}{3} \frac{\partial^2 n}{\partial x^2} \right|_{x=\tilde{x}_i} (h_{i+1} - h_i) + O(h^3) + O((h_{i+1} - h_i)^2), \quad (5.15)$$

$$R_n^{(2)}(i) = \left. \frac{1}{36} \frac{\partial^4 n}{\partial x^4} \right|_{x=\tilde{x}_i} (h_i^2 + h_i h_{i+1} + h_{i+1}^2) + \left. \frac{1}{3} \frac{\partial^3 n}{\partial x^3} \right|_{x=\tilde{x}_i} (h_{i+1} - h_i) + O(h^3) + O((h_{i+1} - h_i)^2). \quad (5.16)$$

Thus the leading terms of $R_{n,U,Z}^{(1,2)}(i)$ depend on the second, third and fourth derivative of the steady-state profile. Figure 5.2 shows these derivatives for the steady-state profile at the standard parameter values. A feasible approach is now to distribute the grid based on some of the terms above. Some results of this approach are given in Appendix B.4. The approach is not used because the results were worse than for the quadratic grid Θ_N^2 .

In the end the best results were obtained with the standard grids in (5.13). Some variations on the standard grid have been used, but these did not show any substantial improvements. For example, it has been tried to use different grids in the boundary layer and the rest of the domain. Table 5.2 shows the results for some different grids. As can be seen the results for the uniform and quadratic grids improve strongly compared to the results in Table 5.1, while the improvement for the cubic grid the improvement is minor. Therefore the standard Θ_N^3 seems to be the best solution.

A possible explanation is given by the form of the local error. Note that the for the quadratic grid it holds that $h_{i+1} - h_i = 2L/N^2$ is the same for all i . For the cubic grid $h_{i+1} - h_i$ will be small near the boundary. When now considering (5.15)–(5.16) the results seem to suggest that the terms involving $h_{i+1} - h_i$ are important near the boundary.

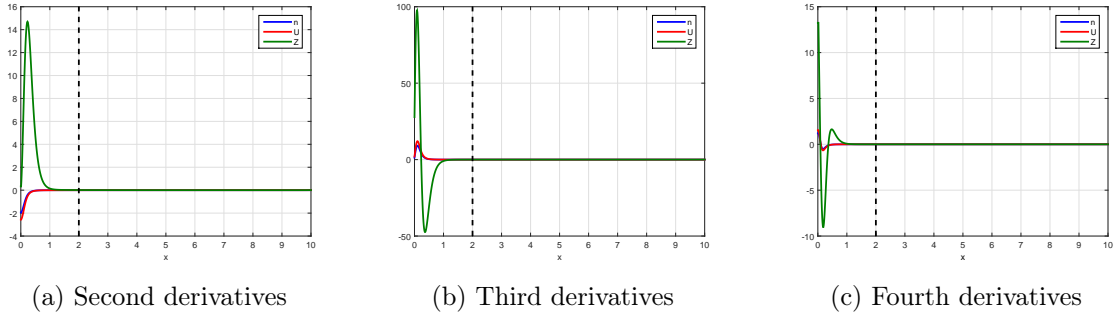


Figure 5.2: Spatial derivatives of a steady state profile.

The cubic grid results in a very small grid spacing near $x = 0$. This causes some numerical instability, especially because the Jacobian matrix is computed using finite differences. It is therefore assured that the difference used to compute the Jacobian matrix will not be larger than the minimal grid spacing. All results in Chapter 6 computed using the FDM on this Θ_N^3 grid (with a possibly an increase in gridspacing near the boundary).

Table 5.2: Determining the best grid distribution on $[0, L_1]$ (with a 10 point uniform grid on $[L_1, L]$)

m_1	N	q_∞ at Hopf
1	30	-1.553919
	50	-1.161700
	100	-0.9630136
2	30	-0.8582992
	50	-0.8264825
	100	-0.8180011
3	30	-0.8204428
	50	-0.8166205
	100	-0.8160030

Chapter 6

Results

In this section, simulation and numerical continuation are used to study the dynamics of the L-H transition models. The chapter is divided in two parts. In Section 6.1, only equilibria of the system are considered. In Section 6.2, the periodic solutions are also included. Recall that unless otherwise stated the parameters are chosen as in Table 4.1.

6.1 Equilibrium solutions

The continuation of local bifurcations was done using CL_MATCONT [4], which is especially aimed at large equilibrium systems. The code of CL_MATCONT was slightly changed, as discussed in Section 3.

6.1.1 1-parameter continuation

First, the equilibrium solutions are continued in the parameter q_∞ . Four different slices have been observed.

Figure 6.1 shows the slice for $b = 0$. The profiles corresponding the steady states at (a) and (b) are shown in Figure 6.2. The profile in Figure 6.2a can be considered as an L-mode profile and the profile in Figure 6.2b can be considered a H-mode profile. This can be understood as follows. Figure 6.1 shows that the value of Z_0 increases when the heat flux $-q_\infty$ is increased. Since $D(Z)$ is decreasing in Z (see Figure 4.2b), a higher value of Z_0 will result in a lower value of $D(Z_0)$. When we now consider the formula for n_0 below (4.11), this means that n_0 will increase when $-q_\infty$ increases. Now consider the confinement time

$$\frac{U}{-q_\infty} = \frac{\int_0^L nT \, dx}{-q_\infty(\gamma - 1)}. \quad (6.1)$$

Note that (4.11) shows that the T/q_∞ will be (approximately) constant along the curve. But because of the increase in n_0 the density n will increase along the whole interval $[0, L]$, resulting in a longer confinement time for a higher value of $-q_\infty$. Note that the computed curve in Figure 6.1 also means that the model will show smooth transitions between L-mode and H-mode when the heat flux q_∞ is slowly increased.

Figure 6.3 shows the section for $b = -0.5$. The corresponding steady-state profiles are displayed in Figure 6.4. When slowly increasing the heat flux $-q_\infty$, the equilibrium becomes unstable at the Hopf-bifurcation. Between the two Hopf-bifurcations periodic solutions will be observed, which correspond

to the dithering observed in experiments. Note that the unstable equilibria will have two unstable eigenvalues. Also the computation of the first Lyapunov coefficient shows that Hopf bifurcation is subcritical, which means that an unstable cycle is generated. The bifurcations of these limit cycles will be studied further in Section 6.2.

Figure 6.5 shows the slice for $b = -1$. Now there are values of q_∞ for which there are three coexisting equilibrium solutions. The three coexisting equilibrium solution at $-q_\infty = 0.75$ are shown in Figure 6.6. When we now follow the curve of equilibria in Figure 6.5 from $-q_\infty = 0.5$, the equilibrium first becomes unstable at the Hopf bifurcation. Between the Hopf and the fold bifurcation there are two unstable eigenvalues. At the fold bifurcation one unstable eigenvalue crosses the imaginary axis, so between the two fold bifurcations there is only one unstable eigenvalue. At the second fold bifurcation there are again two unstable eigenvalues. The section in Figure 6.5 leads to sharp transitions from L-mode to H-mode. Indeed when increasing $-q_\infty$ slowly the solution will jump from L-mode to H-mode at the Hopf bifurcation. When now decreasing $-q_\infty$ again, the solution will jump back at the other Hopf bifurcation. This also explains the hysteresis that was observed.

Figure 6.7 shows the slice for $b = -2$. In this slice there are also multiple steady-state solutions for the same value of q_∞ . Note that one of the Hopf bifurcations has disappeared, but that the two LP bifurcations are still present. This could indicate the presence of the BT bifurcation between $b = -1$ and $b = -2$. Another important observation is that there are now multiple steady-state solutions for the same value of Z_0 . This behavior is possible because there is now more than one possible value for Z_∞ . This is caused by the fact $G(Z)$ has now multiple real roots (the criterion (4.19) implies that for $a = -1$, b must be smaller than $-1.8899 \dots$ to have this). This is illustrated by the profiles in Figure 6.8. Only the profile in Figure 6.8a is physically relevant.

For all results it was established that the spatial discretization was fully converged. In this section only the results for $N = 100$ grid points are presented. Results for $N = 15$, $N = 30$ and $N = 50$ grid points can be found in Appendix C.1.

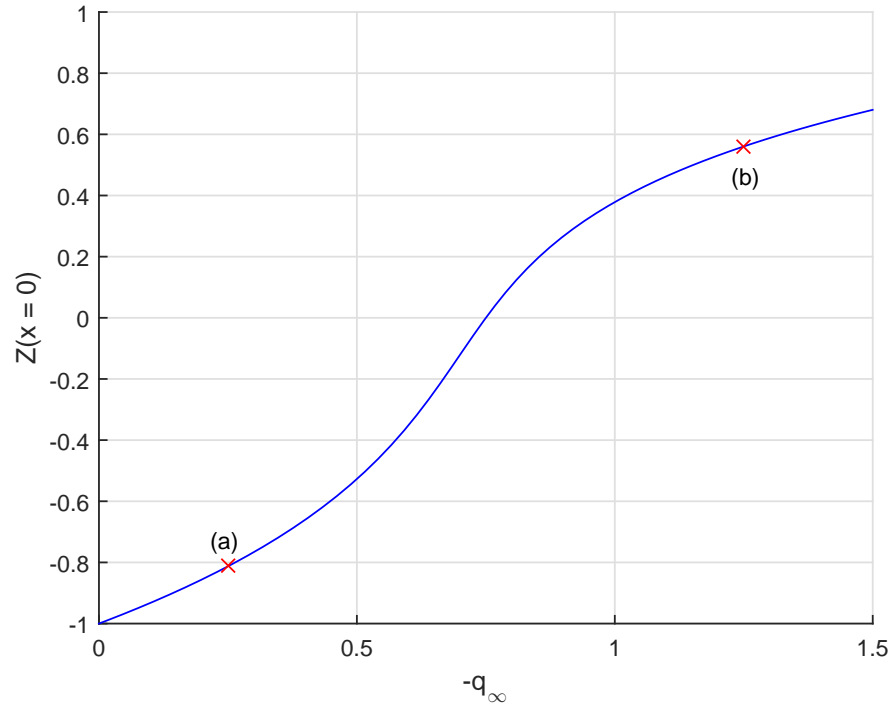
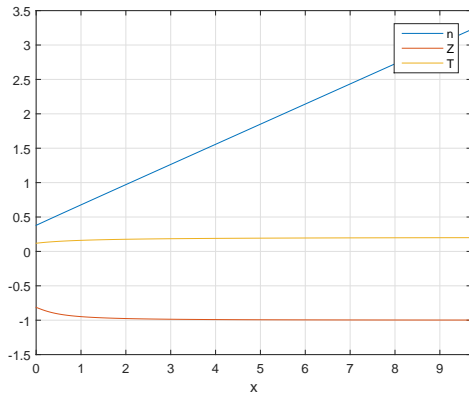
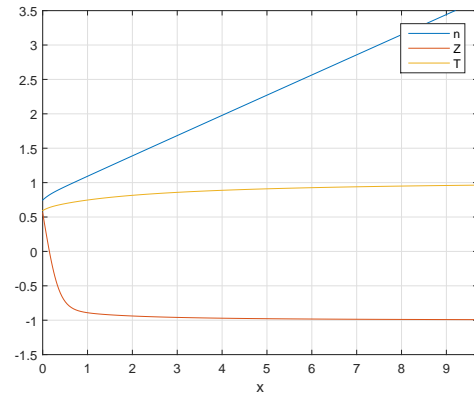


Figure 6.1: Equilibrium continuation in q_∞ at $b = 0$



(a) L-mode profile



(b) H-mode profile

Figure 6.2: Steady-state profiles corresponding the points (a) and (b) in Figure 6.1.

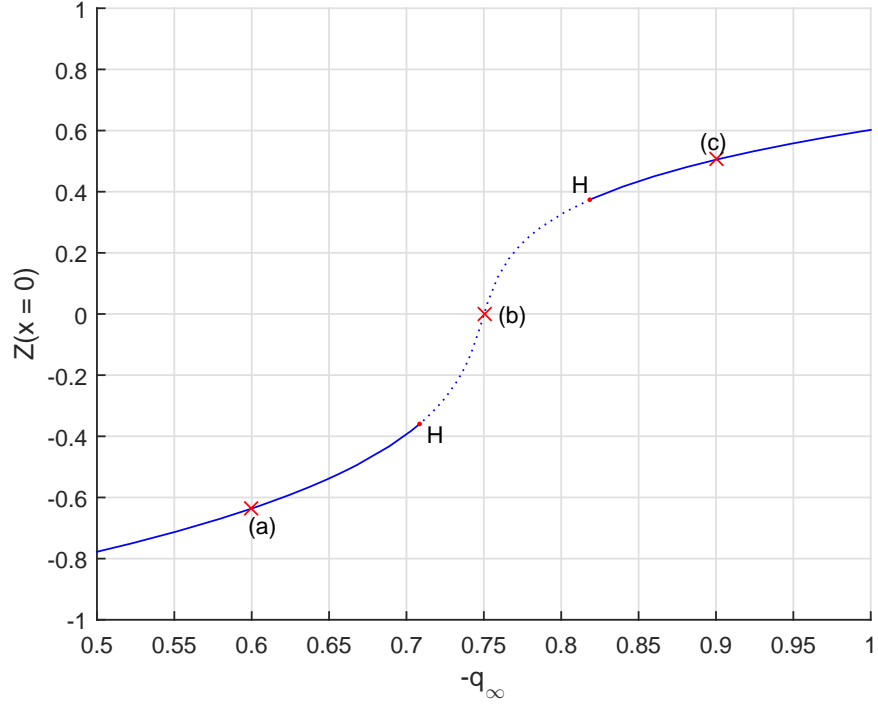
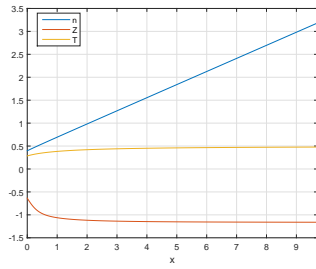
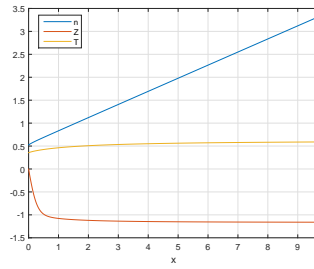


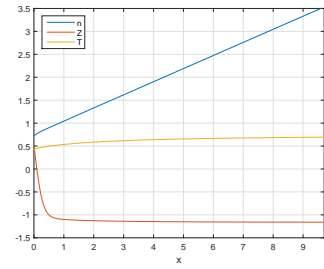
Figure 6.3: Equilibrium continuation in q_∞ at $b = -0.5$



(a) L-mode profile



(b) Unstable profile



(c) H-mode profile

Figure 6.4: Steady-state profiles corresponding the points (a), (b) and (c) in Figure 6.3.

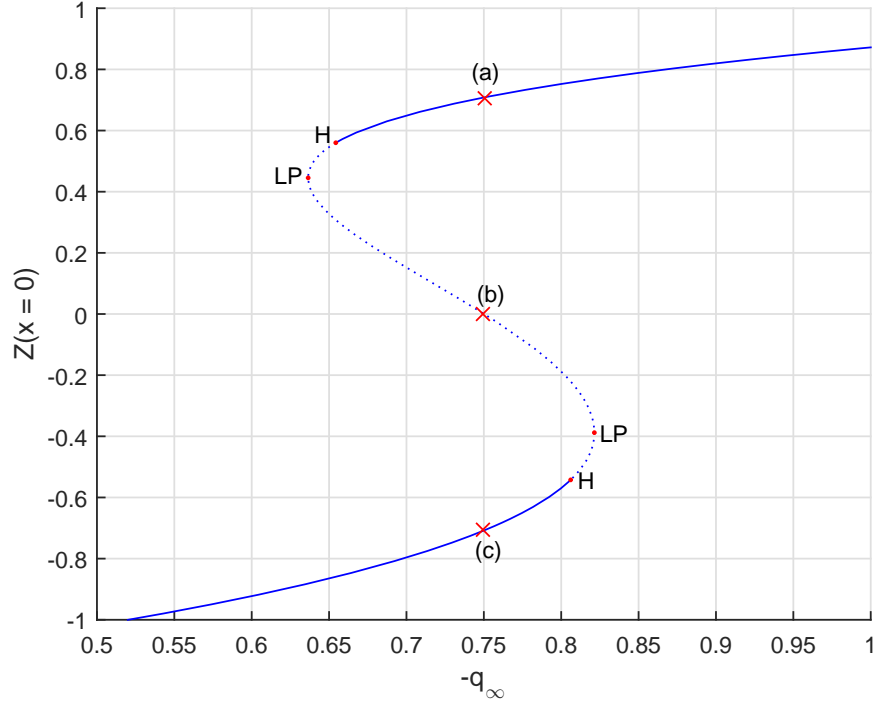
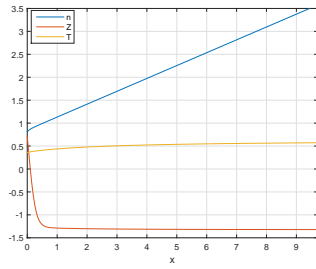
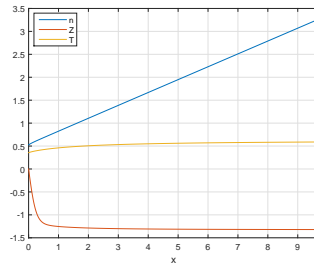


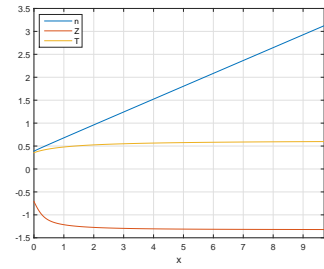
Figure 6.5: Equilibrium continuation in q_∞ at $b = -1$



(a) H-mode profile



(b) Unstable profile



(c) L-mode profile

Figure 6.6: Steady-state profiles corresponding the points (a), (b) and (c) in Figure 6.5.

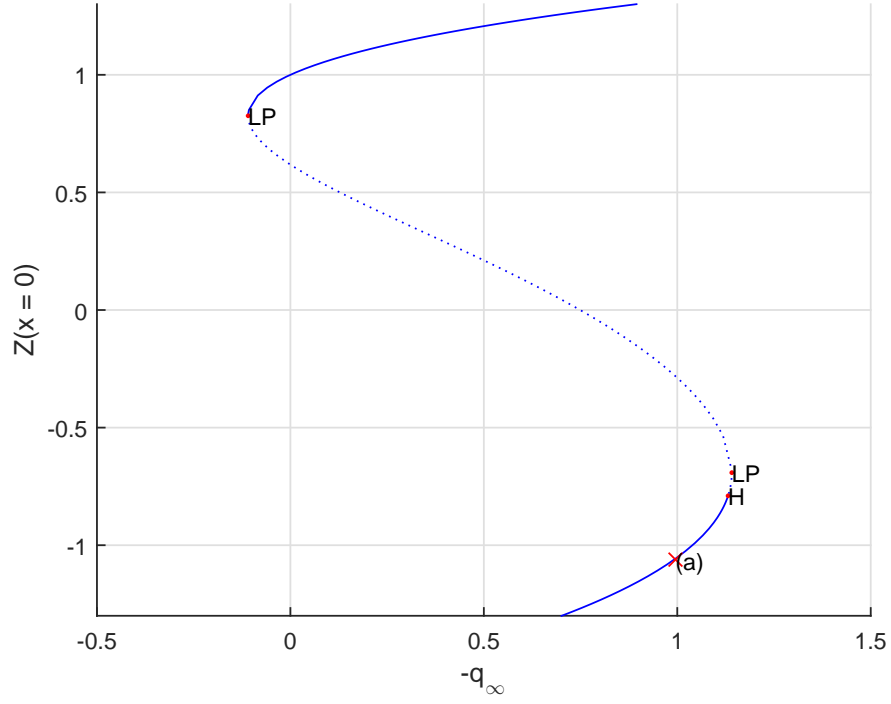
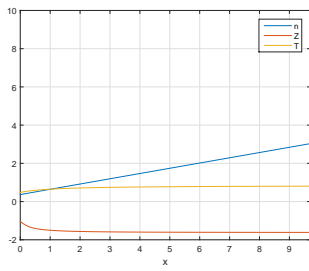
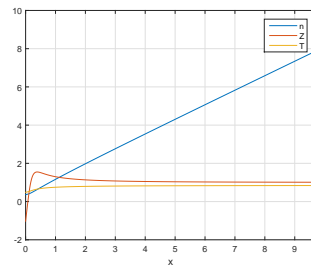


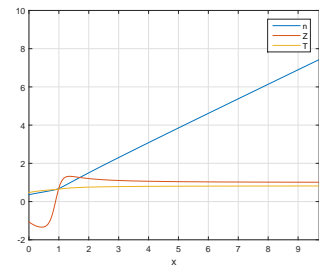
Figure 6.7: Equilibrium continuation in q_∞ at $b = -2$



(a) Physical profile



(b) Nonphysical profile 1



(c) Nonphysical profile 2

Figure 6.8: Different steady-state profiles all corresponding the point (a) in Figure 6.7.

6.1.2 2-parameter continuation

In this section, the fold and Hopf bifurcations detected in the previous section will be continued in two parameters. The continuation parameters are q_∞ and b . While changing the value of the parameter a , three different slices have been found. Again convergence of the spatial discretization was established. Results in this section have been computed for $N = 50$ gridpoints. Results for $N = 30$ and $N = 15$ can be found in Appendix C.2.

Figure 6.9 shows the computed fold and Hopf curves for $a = -1$. This was also the value of a used in the previous section. Note that this figure is in agreement with the slices in Figure 6.1, Figure 6.3, Figure 6.5 and Figure 6.7. Indeed one Hopf bifurcation collides with the fold bifurcation at a BT bifurcation. Note also that the intersection of the Hopf curve with itself is not a Double Hopf bifurcation because both Hopf bifurcations occur at different equilibria. Also observe that there is a GH bifurcation near the BT bifurcation. Recall from Section 2.2.2 that the GH bifurcation occurs when the First Lyapunov coefficient l_1 vanishes. Figure 6.10 shows l_1 along the Hopf curve. Note that the magnitude of l_1 increases strongly near the BT bifurcation (which is natural), and that l_1 is positive near the BT bifurcation. This is also in agreement with the normal form coefficients a_2 and b_2 that are computed at the BT point, which satisfy $a_2 b_2 > 0$ (for a Hopf bifurcation near a BT point it should hold that $\text{sign}(l_1) = \text{sign}(a_2 b_2)$).

Another important observation is that there are no GH points inside the Hopf-loop in Figure 6.9. For all parametric portraits computed near the codimension-4 bifurcation studied in [18] there are two GH points inside in the Hopf-loop. This means that the parametric portrait in Figure 6.9 cannot be topologically equivalent to any of the possible parametric portraits near the codimension-4 BT bifurcation. Also note that the two codimension-3 situations do not show the Hopf-loop. Therefore these results seem to suggest that the slice at $a = -1$ is 'far away' from any of the degenerate BT bifurcations.

Indeed, when the value of a is increased to $a = -0.01$, the slice in Figure 6.11 appears. As Figure 6.11b shows, there are now two GH points inside the Hopf-loop. The Hopf bifurcations to the left of these points are subcritical ($l_1 > 0$) and the Hopf points to the right are supercritical ($l_1 < 0$). This situation resembles the parametric portraits in [18]. This would suggest that we are now close to the codimension-4 situation.

The third slice at $a = -0.005$ is shown in Figure 6.12. First of all note that the Hopf-loop has disappeared. Also the BT bifurcation has moved to the other side of the CP bifurcation. This indicates that somewhere between $a = -0.01$ and $a = -0.005$ the BT and CP coincide, which means that a degenerate BT bifurcation has occurred. When considering the normal form coefficients of the BT in Figure 6.11 and Figure 6.12 it can be seen that the product $a_2 b_2$ is positive in both situations. Note that a codimension-3 degenerate situation would change the sign of $a_2 b_2$, so that either two codimension-3 degeneracies or one codimension-4 degeneracy must have occurred. In the next section, it will be investigated which of the two situations has occurred.

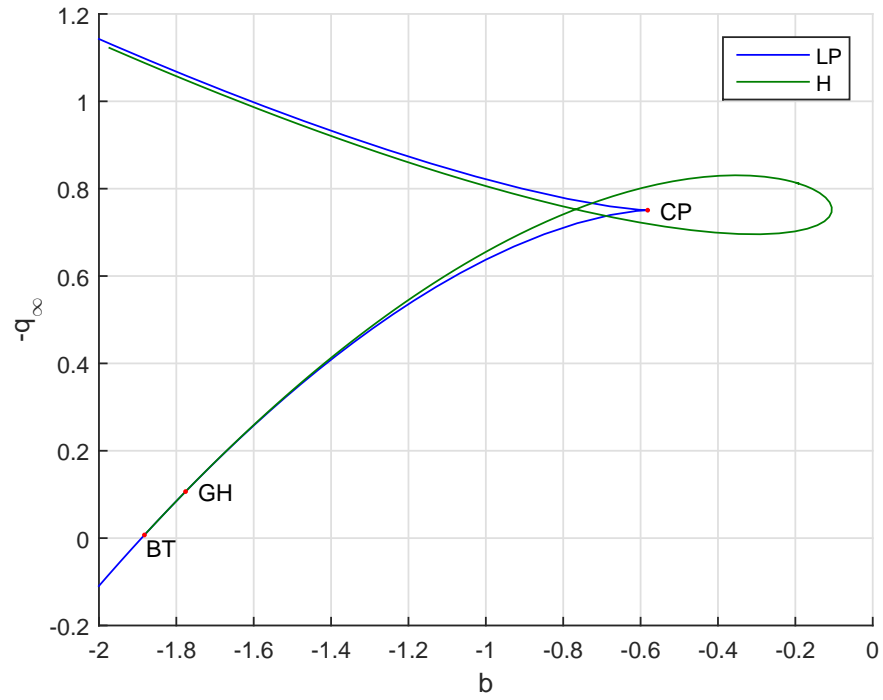


Figure 6.9: The fold and Hopf bifurcation curves in the $(b, -q_\infty)$ -plane at $a = -1$.

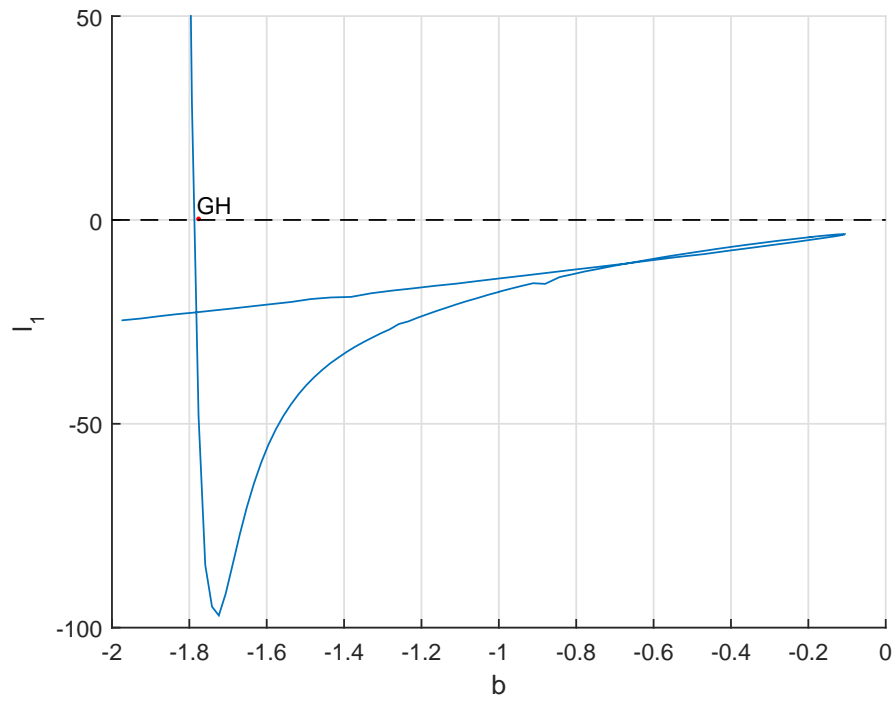
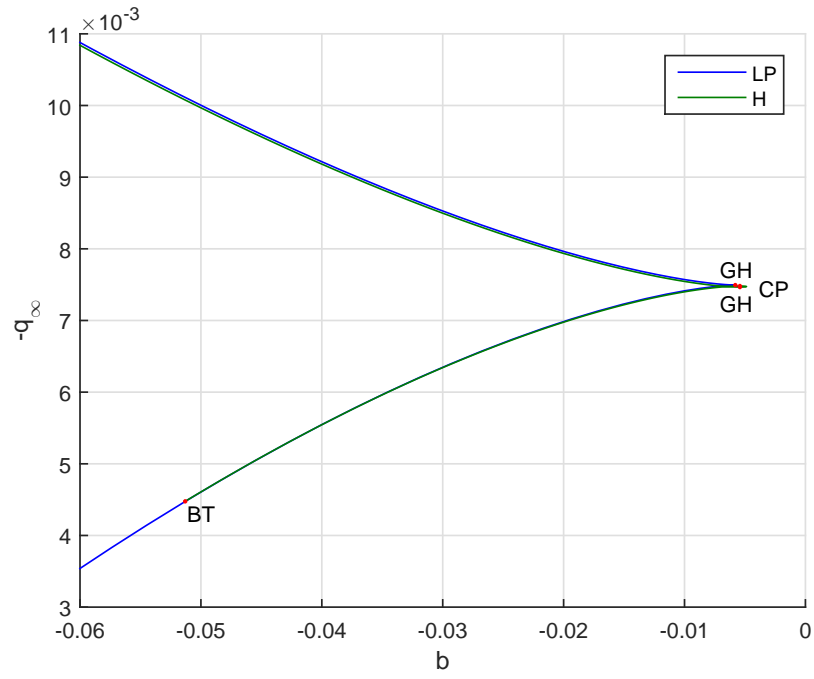
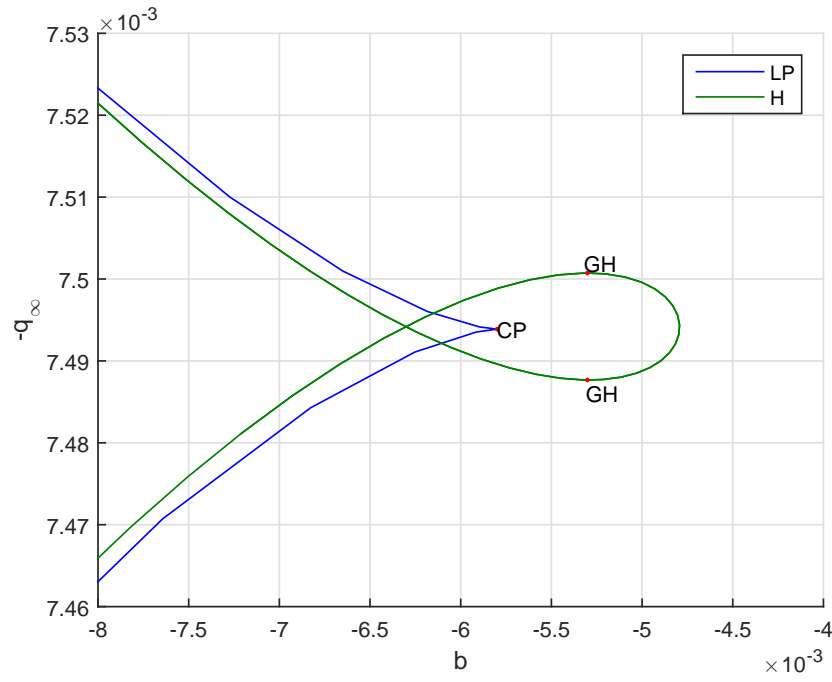


Figure 6.10: The first Lyapunov coefficient along the Hopf curve in Figure 6.9.



(a) Overview



(b) Detailed view

Figure 6.11: The fold and Hopf bifurcation curves in the $(b, -q_\infty)$ -plane at $a = -0.01$.

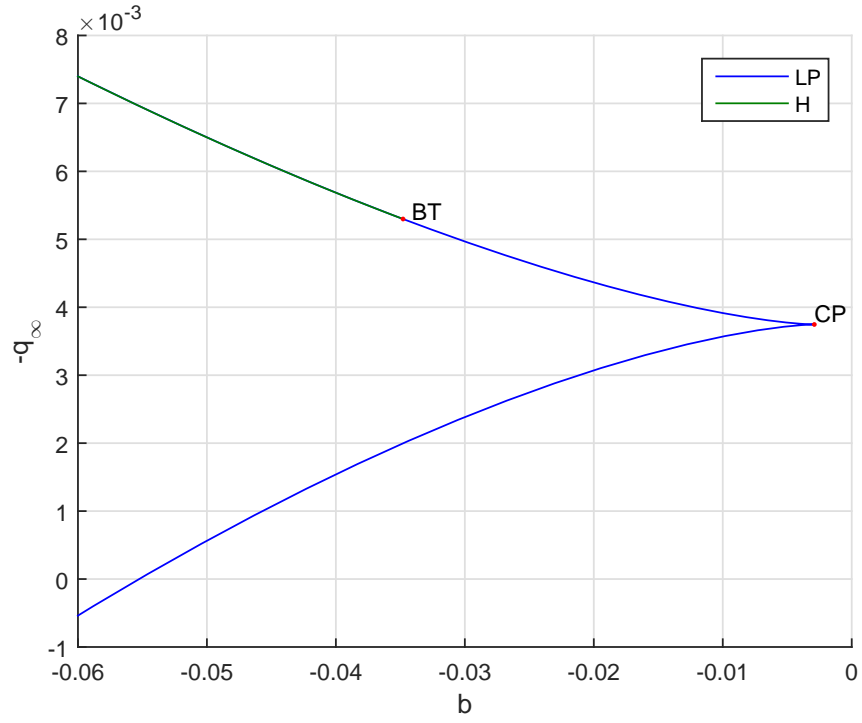


Figure 6.12: The fold and Hopf bifurcation curves in the $(b, -q_\infty)$ -plane at $a = -0.005$.

6.1.3 3-parameter continuation

In this section, the BT bifurcation is continued in the three parameters: q_∞ , b , and a . Along the curve the normal form coefficients a_2 and b_2 are monitored. If one of these coefficients vanishes, a degenerate BT bifurcation of codimension 3 is found. When both coefficients vanish simultaneously the codimension-4 situation occurs. Note that this event is nongeneric in a 3-parameter continuation.

First, the BT point in Figure 6.11a is continued in q_∞ , b , and a . Figure 6.13 shows the computed curve in the (q_∞, b, a) -space and Figure 6.14 shows the projection of this curve on the (a, b) -plane. The normal form coefficients a_2 and b_2 are computed along the curve. These are shown in Figure 6.15. As can be seen both coefficients vanish simultaneously (apparently). The curve has been computed for $N = 15$, $N = 30$ and $N = 50$. Here only the results for $N = 50$ are presented, the other curves can be found in Appendix C.3. For all curves the coefficients a_2 and b_2 vanish apparently simultaneously. Also the normal form coefficients a_3 and b_3 can be computed. These are both negative for all values of N , which is precisely the situation considered in [18].

Since the simultaneous vanishing of both coefficients is nongeneric, the first idea might be that this is caused by a nongeneric choice of the other parameters in Table 4.1. To investigate this hypothesis all 15 remaining parameters have been varied. All parameters values, except the values of D_0 and Z_S , have been increased by 30 % of their default value. The value of D_0 was decreased by 30 %. The value of Z_S was set to 1 (instead of the original value of 0). In all situations the continuation in q_∞ , b , and a resulted in an apparently simultaneous vanishing of both normal form coefficients. All curves have been computed for $N = 15$, $N = 30$ and $N = 50$. (The resulting curves are not explicitly included in the thesis).

We investigate this situation further by computing the two different parts of the coefficient b_2 : $\langle p_0, B(q_0, q_0) \rangle$ and $\langle p_1, B(q_0, q_1) \rangle$ (see (2.24)). These are shown in Figure 6.16. As can be seen both parts also vanish simultaneously (apparently). This is a further indication that the quadratic part $B(\cdot, \cdot)$ is nongeneric for the considered model. In other words, the quadratic part of the model contains some hidden symmetry.

Summarizing the results in this section, it can be concluded that the codimension-4 situation where a_2 and b_2 vanish simultaneously is the only degenerate BT bifurcation that occurs in the model proposed by Zohm in [27]. This situation remains present under variations of the other parameters. The (codimension-3) situations where one of the normal form coefficients a_2 or b_2 vanishes while the other is nonzero have not been observed. This indicates a (hidden) symmetry in the quadratic part of the model.

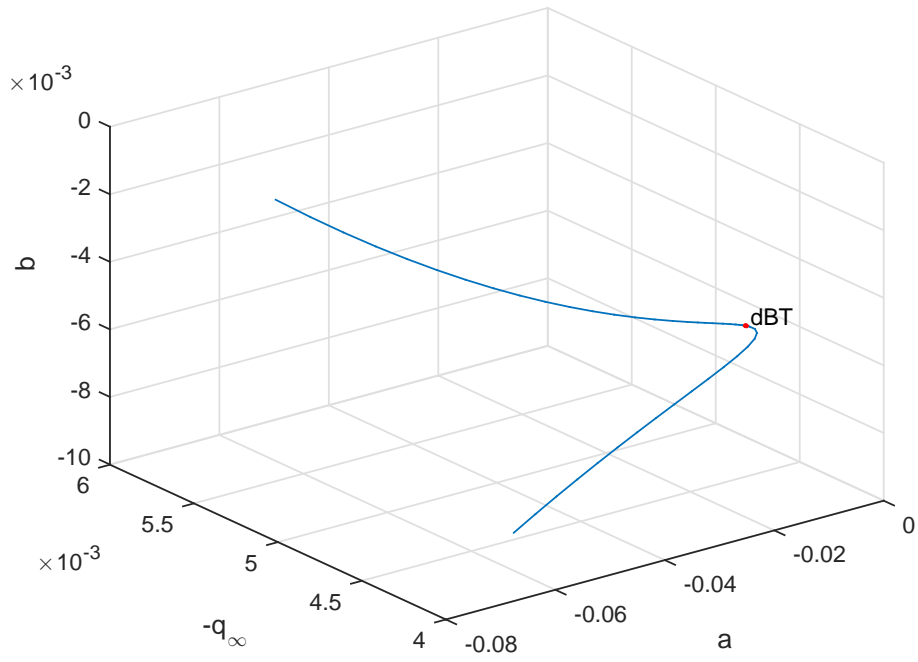


Figure 6.13: The computed curve of BT bifurcations in 3-dimensional the parameter space.

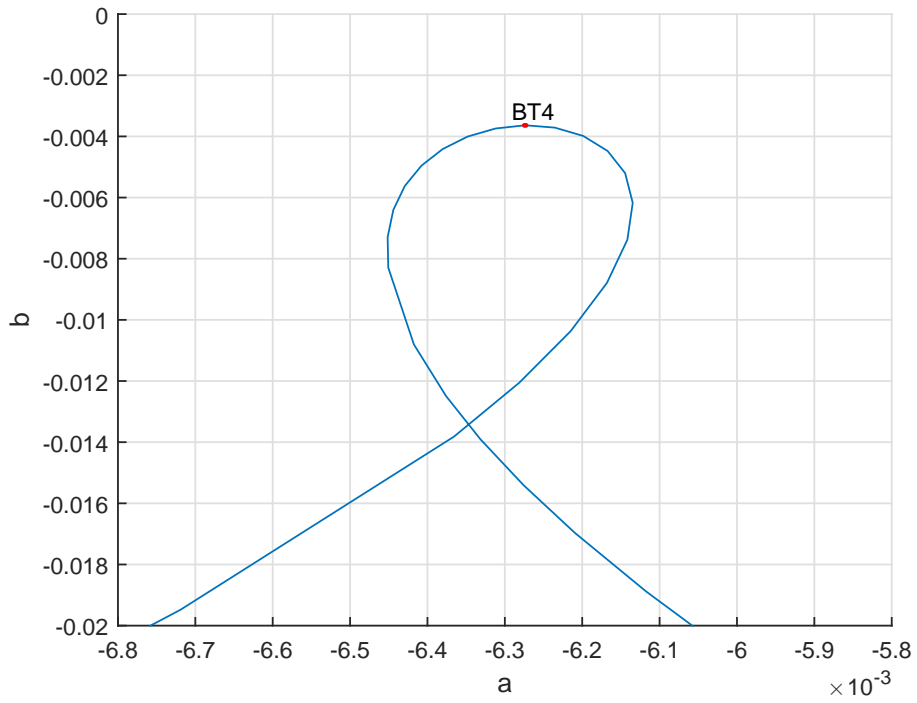


Figure 6.14: Projection of the computed curve of BT bifurcations on the (a, b) -plane.

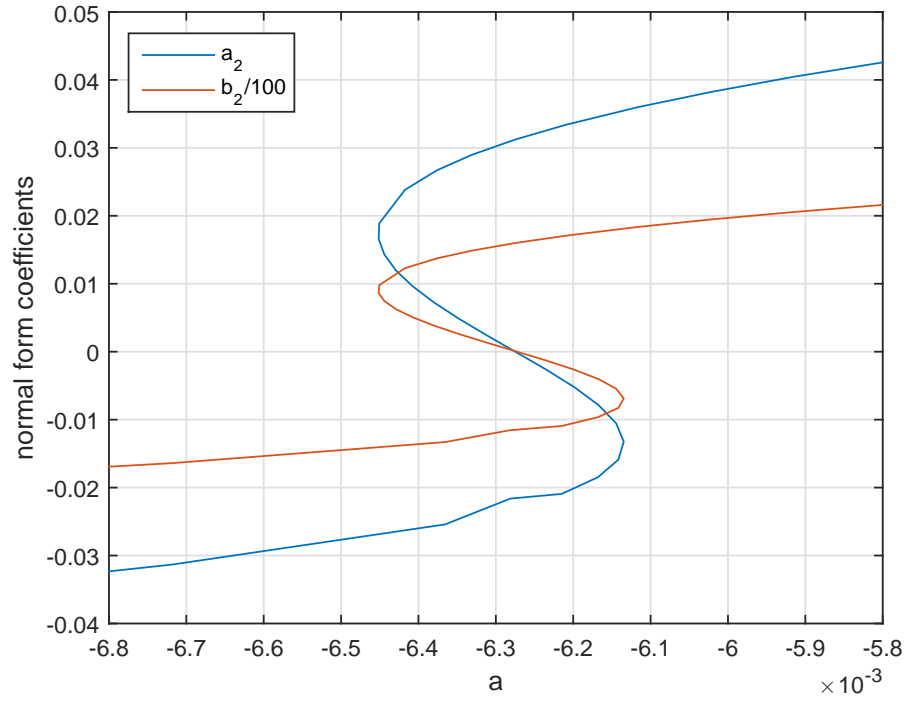


Figure 6.15: The normal form coefficients a_2 and b_2 along the BT curve.

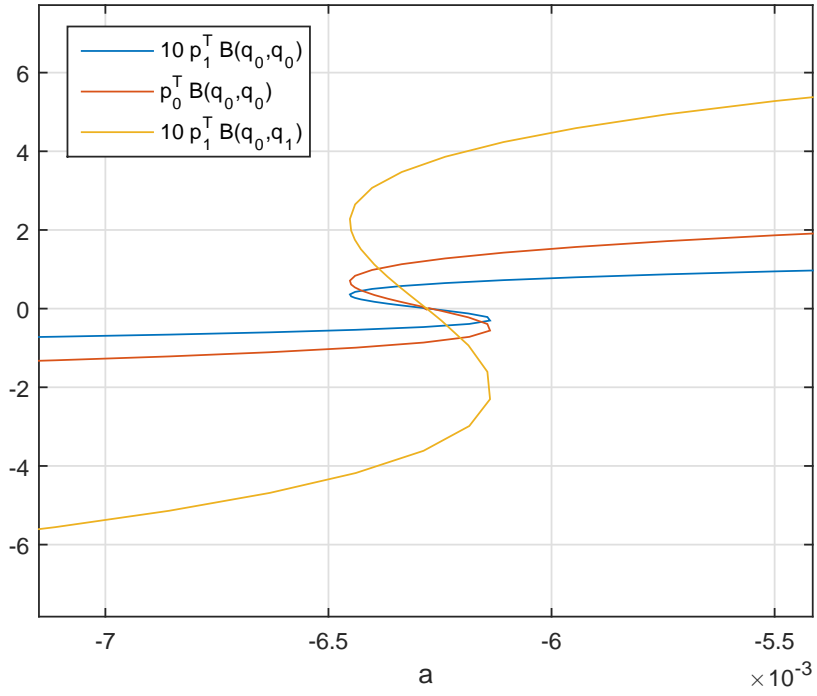


Figure 6.16: Components of the normal form coefficients a_2 and b_2 along the BT curve.

6.1.4 Modifications of the model

In this section we attempt to change the original model of Zohm, such that a complete unfolding of the degenerate BT bifurcation can be observed. In other words, we try to see whether the model considered so far contains an unrealistic symmetry that causes the codimension-4 BT bifurcation. The results in this section have also been verified for $N = 15$, $N = 30$ and $N = 50$.

A possible unnatural symmetry in the model considered so far is that the conductivity $\chi(Z)$ is proportional to the diffusivity $D(Z)$. This symmetry can be destroyed by shifting the conductivity by Z_{S_2} . This leads to a conductivity

$$\chi(Z) = \frac{1}{(\gamma - 1)\zeta} D(Z - Z_{S_2}). \quad (6.2)$$

Note that the original model corresponds to $Z_{S_2} = 0$. For $Z_{S_2} = 2$ the BT bifurcation is continued in q_∞ , b , and a . Still the apparently simultaneous vanishing of both normal form coefficients is observed.

Secondly, we consider a modification of the diffusivity $D(Z)$,

$$D(Z) = D_0 + D_1 \tanh(Z) + D_2 (\tanh(Z))^2. \quad (6.3)$$

Different relations for $D(Z)$ have been used before [25], so it seems reasonable to consider a perturbation of the original function $D(Z)$ proposed by Zohm. For $D_2 = 1$ the BT bifurcation is continued in q_∞ , b and a . Again an apparently simultaneous vanishing of the normal form coefficients a_2 and b_2 is observed.

Finally we consider a different boundary condition for Z at $x = 0$. Instead of requiring that the second derivative of Z is zero as in (4.9), we use a Robin boundary condition

$$\left. \frac{\partial Z}{\partial x} \right|_{x=0} = \frac{Z_0}{\lambda_Z}. \quad (6.4)$$

This boundary condition was also used in [22]. For $\lambda_Z = 1.5$ the BT point has been continued. For $N = 15$, $N = 30$ and $N = 50$ again simultaneous vanishing of both normal form coefficients a_2 and b_2 is observed.

So it can be concluded that all of these modifications do not resolve the apparent simultaneous vanishing of both normal form coefficients, which means that the reasons for the simultaneous vanishing remain unknown.

6.2 Periodic solutions

In this section, we will study the periodic solutions in the model proposed by Zohm. Two slices will be considered. The slice at $a = -0.01$ is relatively 'close' to the degenerate BT bifurcation. The slice at $a = -1$ is further away from the degenerate BT bifurcation. Because the continuation of periodic solutions is computationally demanding, the results have only been computed for $N = 10$ using ('standard' GUI version) MATCONT [6].

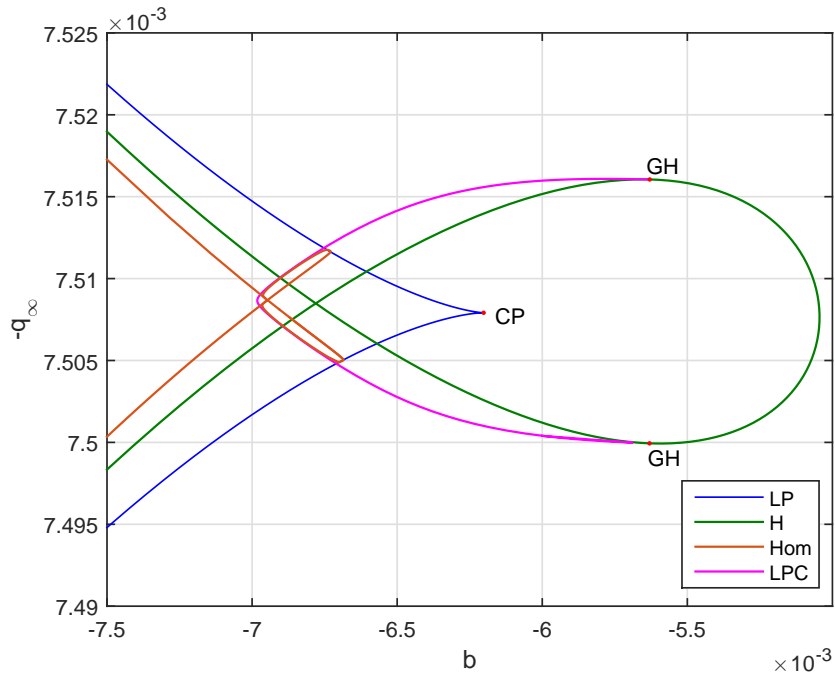
6.2.1 Near the degenerate BT bifurcation at $a = -0.01$

The results of the continuation in the $(b, -q_\infty)$ -plane at $a = -0.01$ are shown in Figure 6.17. Because this slice is relatively close to the codimension-4 degenerate BT bifurcation we expect to recognize much of the curves in parametric portrait in Figure 2.13, Figure 2.14, and Figure 2.15. Note that both GH-points are indeed connected by a curve of LPC-bifurcations, as is also the case in Figure 2.13, Figure 2.14, and Figure 2.15. Inside this loop we can also recognize the typical structure of the homoclinic bifurcations near a codimension-4 degenerate BT bifurcation, as indicated by Figure 6.17b.

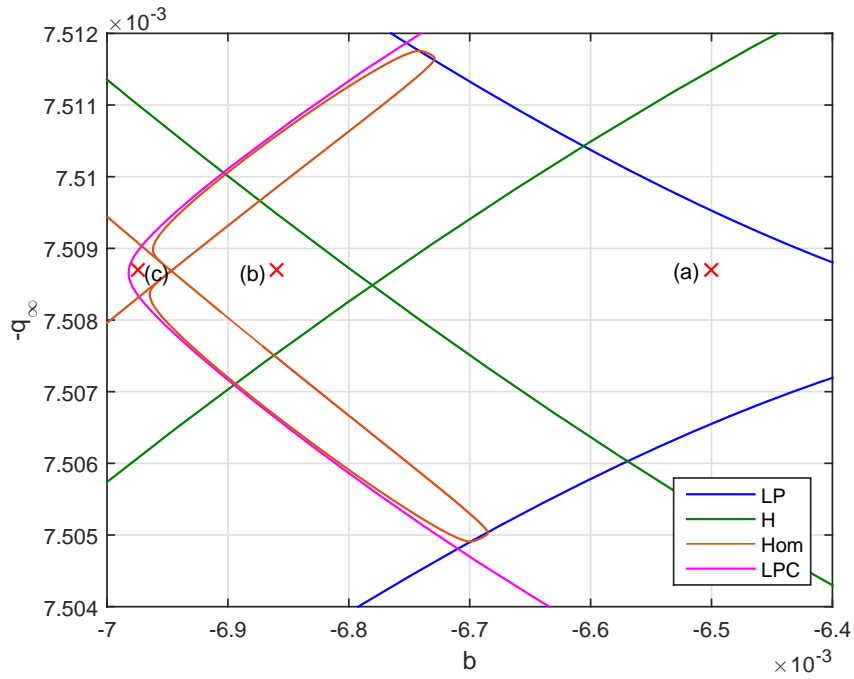
It should be noted that the homoclinic curves were computed by following branches of large amplitude periodic solutions. When plotting these periodic solutions in the (n_0, Z_0) -plane, it seems that the periodic solutions indeed pass (almost) through an equilibrium. Note that this means that the overlap of the Hom and LP bifurcation curves in Figure 6.17b indicates a HSN bifurcation.

Figure 6.18 shows some slices for $b = \text{const}$ in Figure 6.17. These provide more insight about the behavior of periodic solutions near the degenerate BT bifurcation. Figure 6.18a shows the situation right of the two GH bifurcations. Here the (subcritical) Hopf bifurcation generates a stable cycle that disappears again at a second Hopf bifurcation. Figure 6.18b shows the situation just left of the two GH bifurcations. Now the Hopf bifurcations are supercritical meaning that they generate an unstable cycle. This cycle becomes stable at the LPC bifurcation. When moving further to the left in Figure 6.17, we pass a Cusp bifurcation. This does not affect the periodic solutions, so Figure 6.18b still applies. However, between the LP curves there are now three unstable equilibria, as is indicated in Figure 6.19a. A different section appears near the left of the NSH bifurcations. Figure 6.18c shows a slice left of the HSN curves. Figure 6.19b shows three coexisting periodic solution in the (n_0, Z_0) -space in this section. Note that the stable periodic solution surrounds all three equilibria and that the unstable periodic solution surrounds only one equilibrium. The branch of the stable periodic solutions in Figure 6.18c still passes through an LPC bifurcation, but ends in a homoclinic bifurcation now. Also note that this homoclinic is very close to the LPC bifurcation. The branches of the other two (unstable) cycles start at the Hopf bifurcation and end also at a homoclinic bifurcation. Figure 6.18d shows the situation even further to the left. Now homoclinic bifurcations on the branch with stable periodic solutions have disappeared. The two unstable endpoints of the branch now connect. An example of the coexisting stable and unstable periodic solutions is shown in Figure 6.19c. Figure 6.18e shows the situation left of the LPC bifurcation loop. Only the cycles resulting from the Hopf bifurcation remain. These still end at a homoclinic bifurcation.

From a physical point of view, it is particularly interesting to know the domain in which (stable) periodic solutions can be observed. The discussion above showed that this domain is bounded by the LPC curve and the H-curve right of the GH bifurcations. In a small portion of this domain (bounded by the H-curves left of the GH bifurcation) there are also coexisting stable stationary solution(s).



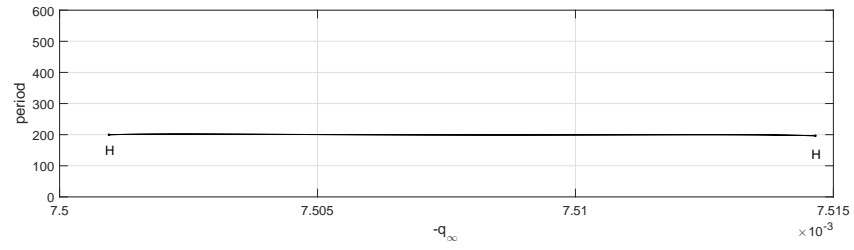
(a) Overview



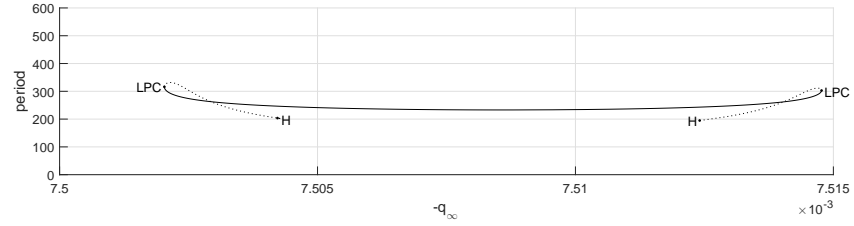
(b) Detailed view.

The points (a), (b) and (c) correspond to the phase portraits in Figure 6.19.

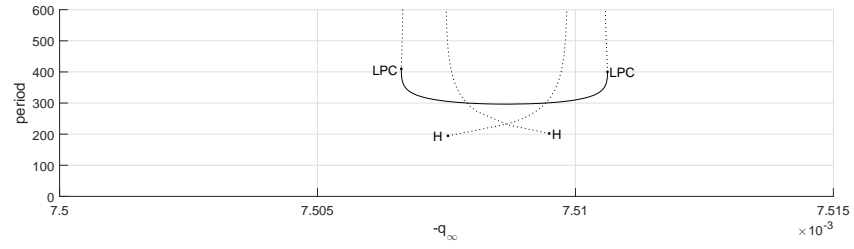
Figure 6.17: Global bifurcation curves at $a = -0.01$



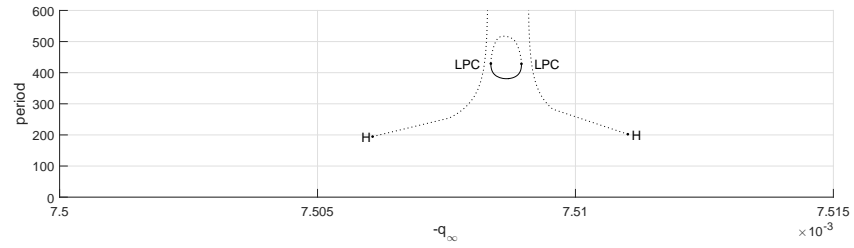
(a) Section at $b = -0.005300$



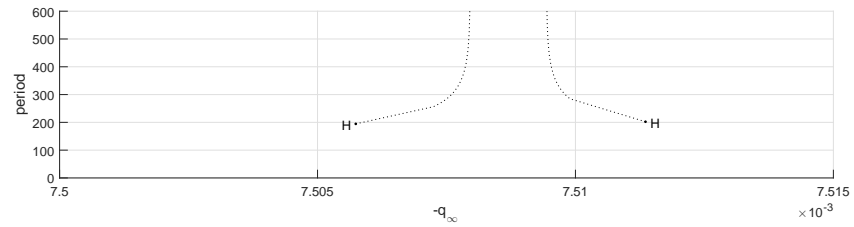
(b) Section at $b = -0.006300$



(c) Section at $b = -0.006860$

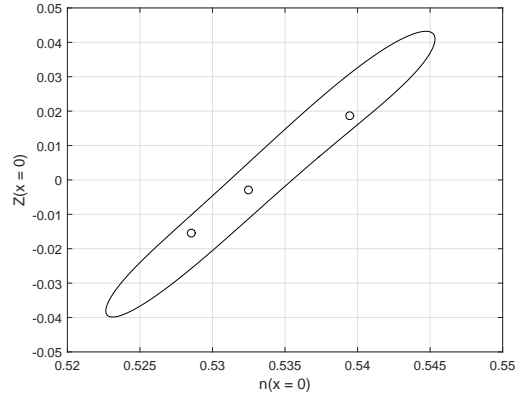


(d) Section at $b = -0.006975$

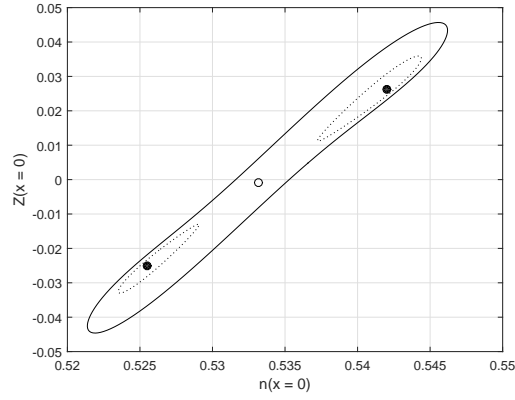


(e) Section at $b = -0.007000$

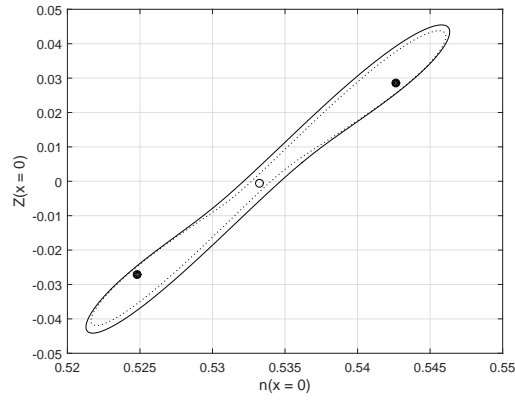
Figure 6.18: Branches of periodic solutions for some values of b at $a = -0.01$. (Stable branches are indicated by solid lines and unstable branches by dotted lines)



(a) At $b = -0.006500$ and $q_\infty = -0.0075087$



(b) At $b = -0.006860$ and $q_\infty = -0.0075087$



(c) At $b = -0.006975$ and $q_\infty = -0.0075087$

Figure 6.19: Some phase portraits at $a = -0.01$.
(Stable periodic solutions are indicated by solid lines, unstable periodic solutions by dotted lines, stable equilibria by a filled dot and unstable equilibria by an open dot)

6.2.2 Far away from the degenerate BT bifurcation at $a = -1$

The value of $a = -1$ is relatively far away from the degenerate BT bifurcation. This can be seen from the parametric portrait in Figure 6.9 in which the two GH points in the H-loop is missing. This means that the bifurcation cannot resemble the one observed in the normal form of the degenerate BT bifurcation in Figure 2.13, Figure 2.14, and Figure 2.15.

Figure 6.20 shows the parametric portrait at $a = -1$ for $N = 10$. As can be seen two curves of PD bifurcations have appeared. Figure 6.21 shows that these PD bifurcations can also be observed for $N = 5$ gridpoints. This suggests that these bifurcations are also present in the PDE model. However, true convergence could not be established due to the long computation times.

Figure 6.22 shows five slices in Figure 6.20 for $b = \text{const}$. Figure 6.22a shows the slice at $b = -0.2$. Here the two supercritical Hopf bifurcations generate a stable cycle. Note that this behavior is still very similar to the behavior observed near the degenerate BT bifurcation in Figure 6.18a. Figure 6.22b shows the appearance of the four PD bifurcations. Figure 6.22c shows the appearance of LPC bifurcations, which suggests that a cusp point of cycles is present between $b = -0.3$ and $b = -0.5$. These LPC bifurcations are not shown in Figure 6.20 because their continuation was not possible due to large computation times. Figure 6.22d shows the slice for $b = -0.7$. Now the cycles become unstable at the PD bifurcation and seem to approach a homoclinic bifurcation. Figure 6.22e shows basically the same situation at $b = -1$, only now the two curves are switched.

The parametric portrait in Figure 6.20 is not complete. One of the questions that remains is how the PD and LPC bifurcations disappear between $b = -0.5$ and $b = -0.7$. Also the period $2T$ cycles appearing at the PD bifurcation have not been continued (again due to the high computational effort).

Figure 6.23, Figure 6.24, Figure 6.25 and Figure 6.26 show the time history and the projection on the (n_0, Z_0) -space of some of the computed periodic solutions. These figures have been obtained by time integration, so all of the cycles that are shown are stable. The parameter values at which the cycles have been computed are also indicated in Figure 6.20.

Figure 6.23 shows a periodic solution inside the PD loop. The time history seems to indicate that this indeed a period $2T$ periodic solution resulting from the PD bifurcation. In the projection on the (n_0, Z_0) -plane, the location of the (unstable) equilibrium near the cycle might suggest homoclinic bifurcations nearby.

Figure 6.24 shows a typical periodic solution that is observed between the two curves of PD bifurcations (which are also observed in continuation in Figure 6.22b and Figure 6.22c). Because the parameters are chosen inside the wedge of LP bifurcations there are now three unstable equilibria. As can be seen two of these equilibria are relatively close to the periodic solution. The time history shows that the periodic solution moves relatively slowly when it is close to these equilibria.

Figure 6.25 shows a periodic solution for parameter values relatively close to the ones used in Figure 6.24. Even when simulating for a very long time interval, the solution does not become completely periodic. The projection on the (n_0, Z_0) -plane shows two possible traces on the left. It seems that the solution picks one of these traces rather randomly, as indicated by the time history. These problems can also be caused by numerical inaccuracies in the ODE solver.

Figure 6.26 shows a solution that seems to be very close to a homoclinic orbit. The equilibrium involved has a complex pair of unstable eigenvalues. The detailed view in Figure 6.26c suggests that the solution indeed leaves the equilibrium via the unstable manifold associated to these eigenvalues.

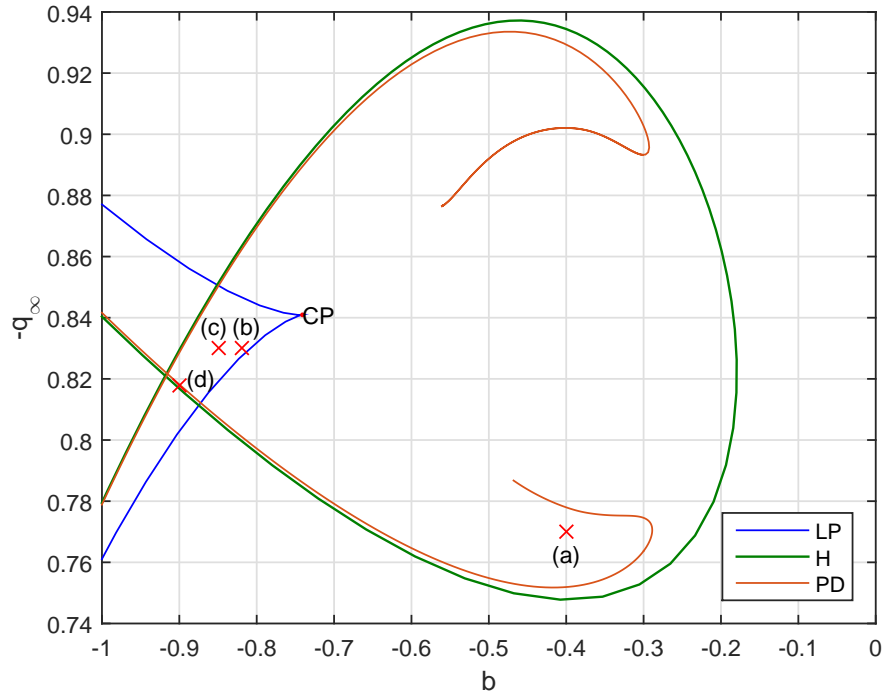


Figure 6.20: Some of the global bifurcations at $a = -1$ for $N = 10$ gridpoints.

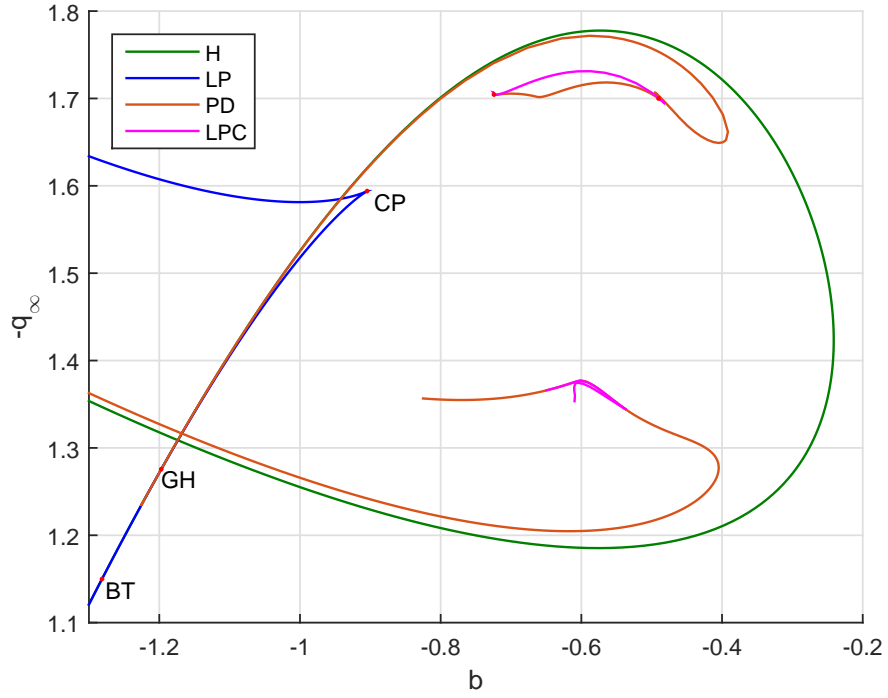
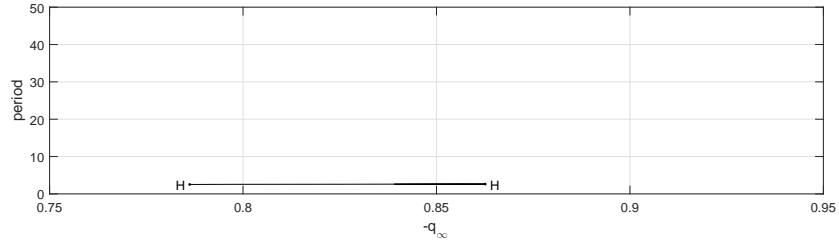
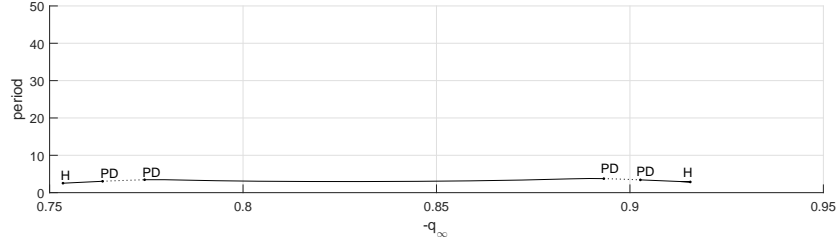


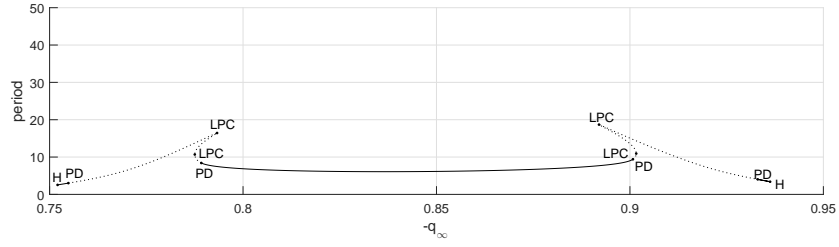
Figure 6.21: Some of the global bifurcations at $a = -1$ for $N = 5$ gridpoints.



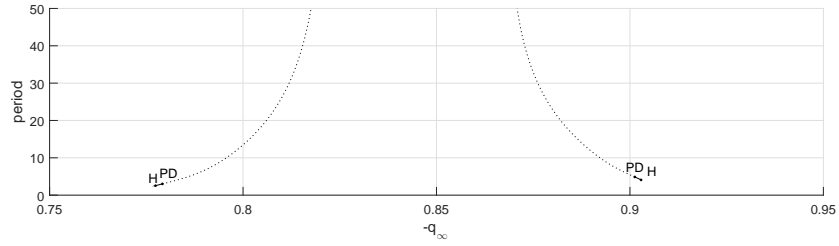
(a) Section at $b = -0.2$



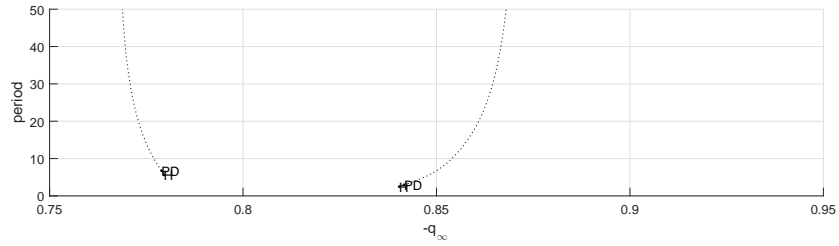
(b) Section at $b = -0.3$



(c) Section at $b = -0.5$

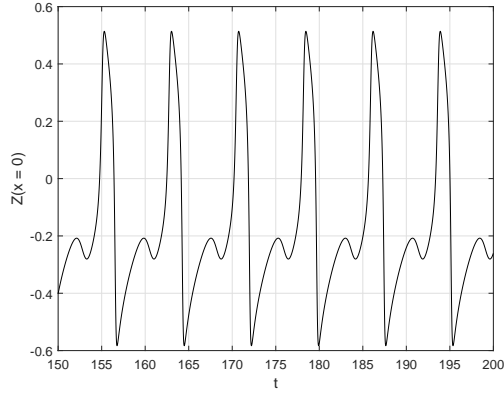


(d) Section at $b = -0.7$

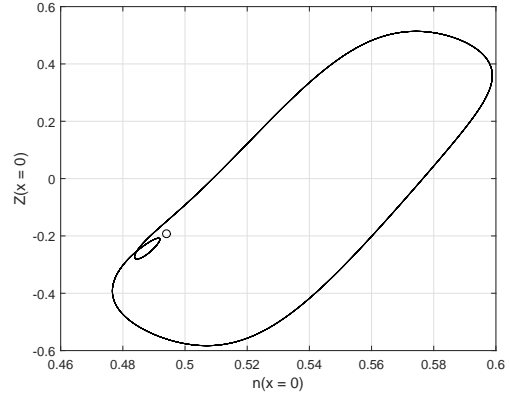


(e) Section at $b = -1$

Figure 6.22: Branches of periodic solutions for some values of b at $a = -1$ for $N = 10$. (Stable branches are indicated by solid lines and unstable branches by dotted lines)

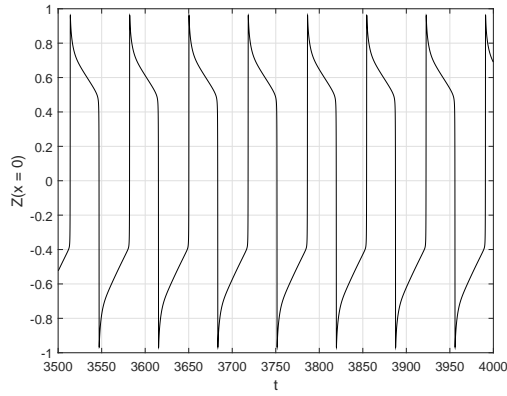


(a) Time history

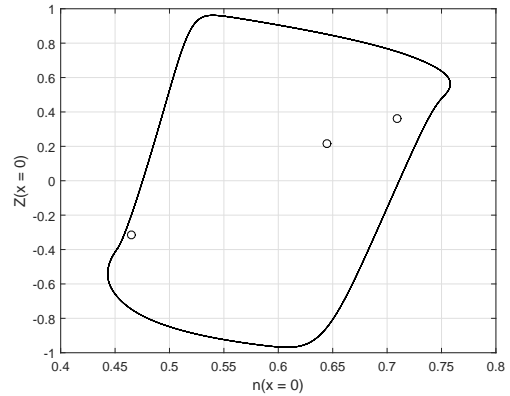


(b) In the (n_0, Z_0) -space

Figure 6.23: The periodic solution at $q_\infty = -0.77$, $b = -0.4$ and $a = -1$.
(The unstable equilibrium is indicated by an open dot)

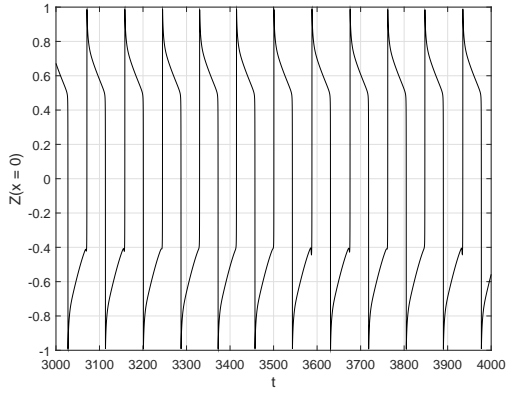


(a) Time history

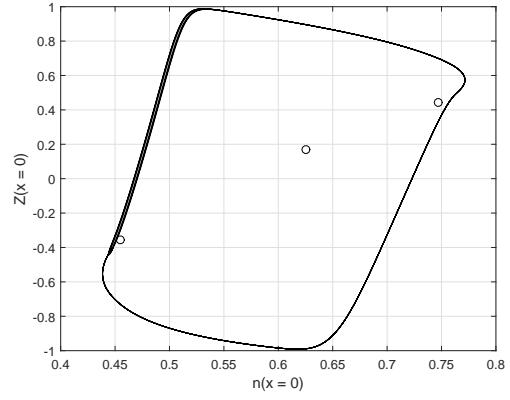


(b) In the (n_0, Z_0) -space

Figure 6.24: The periodic solution at $q_\infty = -0.83$, $b = -0.82$ and $a = -1$.
(The unstable equilibria are indicated by an open dot)

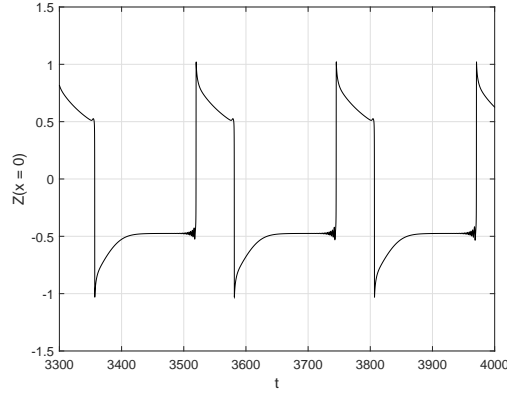


(a) Time history

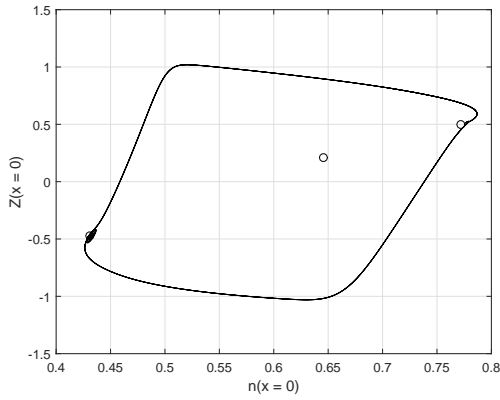


(b) In the (n_0, Z_0) -space

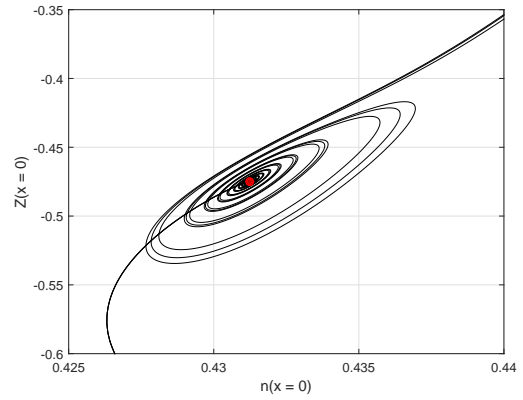
Figure 6.25: The periodic solution at $q_\infty = -0.83$, $b = -0.85$ and $a = -1$.
(The unstable equilibria are indicated by an open dot)



(a) Time history



(b) In the (n_0, Z_0) -space



(c) In the (n_0, Z_0) -space

Figure 6.26: The periodic solution at $q_\infty = -0.818$, $b = -0.9$ and $a = -1$.
(The unstable equilibria are indicated by an open dot)

Chapter 7

Conclusion and outlook

This chapter contains a conclusion of the thesis and an outlook to possible further research.

7.1 Conclusion

Before coming to the main question in this research, first the sub-questions are answered.

Which dynamic behavior can be expected near a degenerate Bogdanov-Takens bifurcation?

As has been explained in Chapter 2, this question can be answered by studying the unfolding of the normal form the bifurcation. For the two codimension-3 degeneracies the 3-parameter unfoldings of the normal form have been extensively studied in literature. The unfolding of the codimension-4 degeneracy has two subcases. The physically most relevant subcase has been studied in the literature too. These unfoldings contained CP, GH and BT bifurcations, as well as NCH and NSH bifurcations. Also the arrangement of the different bifurcation curves can be found from the analysis of the normal forms.

It should be noted that the correspondence between the parameters in the system and the parameters in the unfolding of the normal form is generally not known (only for some very simple cases a correspondence can be obtained). Therefore the normal form analysis does not provide information about how a variation in the physical parameters of the model will affect the dynamic behavior.

What is an accurate and efficient spatial discretization of the model proposed by Zohm?

The aim of the model proposed by Zohm is to explain the dynamics related L–H transition in fusion plasmas. Because the H–mode is the result of the formation of an insulating boundary layer at the edge of plasma, we expect that the spatial discretization must be more accurate near the edge of the plasma. This was also suggested by the shape of the steady-state profiles computed in [25] and [22], which show large gradients in the radial electric field Z near the edge $x = 0$. Indeed, we obtained accurate results with a relatively low number of gridpoints on a nonuniform grid that accumulates near the boundary $x = 0$. The distribution of the grid points was determined by trial and error approach. Also an approach based on the local error was attempted, but did not result in better results.

Both the FVM and FDM have been used to obtain a discretization. The accuracy of both methods has been compared on a variety of grids. The FDM is used because it results in a sparser Jacobian matrix A and the FVM did not show significantly better accuracy.

How can degenerate Bogdanov-Takens bifurcations be found in this model?

The degenerate BT bifurcations that are considered here are of codimension 3 or codimension 4. This means that 3 or 4 parameters are needed to see this bifurcation, which makes it difficult to find the bifurcation by direct simulations in the model. Therefore numerical continuation techniques have been used to find the degenerate BT bifurcations. One of the available software packages is MATCONT.

An obstacle in this approach is that the discretization of a PDE typically results in large system of ODEs. Continuation for large systems of ODEs in MATCONT can be computationally demanding. This problem can be addressed by using CL_MATCONT, which is specially developed for large systems of ODEs. CL_MATCONT only supports the continuations of equilibria, Hopf and LP bifurcations. Additionally, the continuation of BT bifurcations was added to CL_MATCONT. Also some other changes have been made to the code of CL_MATCONT.

Degenerate BT bifurcations can now be found using the following approach. First an equilibrium is continued to find a LP or Hopf bifurcation. Then the LP or Hopf bifurcation is continued to find a BT bifurcation (of codimension 2). This BT bifurcation can then again be continued in three parameters. At each point on the BT curve the normal form coefficients a_2 and b_2 are computed. Degenerate BT bifurcations of codimension 3 are found when one of these coefficients vanishes. Generically both normal form coefficients will not vanish in the same point. This means that one of the (one of the) codimension-3 degenerate BT bifurcations must be continued in four parameters to find a codimension-4 BT. The continuation of degenerate BT bifurcations was not implemented during this project.

Now the main question in the thesis can be addressed.

Does a degenerate BT bifurcations occur in the model proposed by Zohm?

To obtain a better understanding of the dynamics in fusion plasmas, simplified transport models have been formulated [27]. Studying these models provides more insight in the complex dynamics in plasmas. These models have been studied by direct simulation by [25] and [22]. This resulted in the hypothesis that these models contained a degenerate Bogdanov-Takens bifurcation (of codimension 3 or 4). However, this hypothesis was not verified by direct normal form computations.

By numerical continuation of the BT bifurcation in three parameters, it was possible to compute the normal form coefficients a_2 and b_2 along the computed curve. In this way degenerate BT bifurcations were located in Zohm's model. In this way, the hypothesis of [25] was confirmed. However, only the codimension-4 situation where $a_2 = b_2 = 0$ has been observed in all 3-parameter continuations. This seems to indicate that the model contains some hidden symmetry in its quadratic terms which cannot be destroyed using the considered parameters. This also suggests that the codimension-4 degenerate BT bifurcation may not completely unfold by the considered parameters. It should also be noted that the dynamics of Zohm's model are not completely characterized by the presence of this bifurcation. For parameter values relatively far away from the degenerate BT bifurcation very complex dynamics have been observed.

7.2 Outlook

There are some suggestions for future research on the dynamics in Zohm's model.

- Some interesting analytic results have been found in [5]. For example an analytic asymptotic expression for the location of the Hopf bifurcation has been formulated and a possible correspondence between the physical parameters and parameters in the normal form (2.33) has been proposed. However, the accuracy of these expressions has not been validated. These results might also provide further insight in the symmetry responsible for the appearance of the codimension-4 situation.
- In [25] different diffusivity functions have been used, which have a better physical basis than the one used here. It would be interesting to see whether the simultaneous vanishing of a_2 and b_2 still occurs when these functions are used. However one perturbation of $D(Z)$ has already been studied and this still showed the codimension-4 situation. However, the simulations in [25] show that there are choices for $D(Z)$ that will significantly change the bifurcation landscape.
- Also the study of the global bifurcations in the model seems promising. Especially the presence of the Period Doubling bifurcation indicates interesting dynamic behavior far away from the degenerate Bogdanov-Takens bifurcation, which is not completely understood at the moment. It is also natural to expect that homoclinic bifurcations will play an important role here.

There are also some suggestions regarding the numerical continuation.

- More than 90 % of the computation time of the curves of equilibrium, LP, Hopf and BT is now consumed by the evaluation of the Jacobian matrix. This also explains why the use of the parallel computing toolbox significantly speeds up the computation. At the moment the Jacobian matrix is computed using finite differences. This does not exploit the structure that follows from the spatial discretization. Computation time can be reduced (probably significantly) by using the structure that follows from the spatial discretization. Due to the complexity of the system it would be best to introduce to a 'standard' discretization for any (system of) second order PDE as input (as was already done in [21]).
- The study of the bifurcations of limit cycles was limited because CL_MATCONTL does not support the continuation of (bifurcations of) periodic solutions. To study the limit cycles, other numerical methods for large-scale systems will be needed. Eventually it would be very good to have the same continuation options in CL_MATCONT as in CL_MATCONTL. It might even be possible to incorporate CL_MATCONTL completely in CL_MATCONT, so that the user can choose to use the algorithms for large-scale systems by an option.

Appendix A

Approximate steady-state solutions

In this appendix we will show an accurate approximation of a steady-state profile \tilde{Z} in (4.12). When this solution is known the steady-state profiles for \tilde{n} and \tilde{T} follow from (4.10) and (4.11).

When $\tilde{n}(x)$ is approximated by n_0 , (4.12) becomes

$$\begin{aligned} -\mu \frac{\partial^2 \tilde{Z}}{\partial x^2} &= -\frac{T_\infty \Gamma_\infty}{n_0^2} (c_n + c_g) \frac{1}{D(\tilde{Z})} + G(\tilde{Z}) \\ &= \frac{D(Z_0)G(Z_0)}{D(\tilde{Z})} + G(\tilde{Z}). \end{aligned} \quad (\text{A.1})$$

Next the RHS of (A.1) is expanded as a third order Taylor expansion around Z_S . After multiplication by -1 , we obtain an equation of the form

$$\mu \frac{\partial^2 \tilde{Z}}{\partial x^2} = c(\tilde{Z} - Z_L)(\tilde{Z} - Z_2)(\tilde{Z} - Z_3). \quad (\text{A.2})$$

The smallest root is denoted by Z_L . The root that is closest to Z_0 is denoted by Z_2 and the other root by Z_3 . When $2Z_3 < Z_2 + Z_L$, the solution to (A.2) is now given by

$$\tilde{Z}(x) = Z_L + z_3 \frac{q_- + 1}{q_- + e^{kx}} \frac{q_+ + 1}{q_+ + e^{-kx}}, \quad (\text{A.3})$$

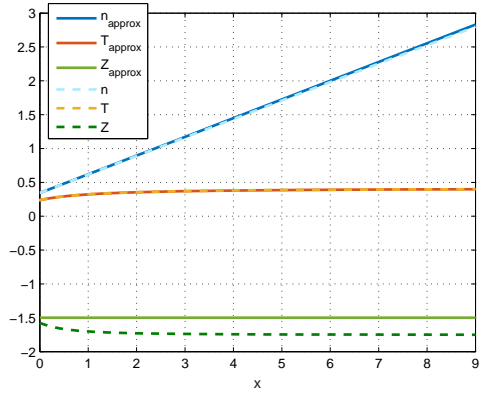
where $z_2 := Z_2 - Z_L$, $z_3 := Z_3 - Z_L$ and

$$\begin{aligned} k &= \sqrt{\frac{c}{\mu} z_2 z_3}, \\ q_\pm &= \sqrt{2z_3 - z_2} \frac{\sqrt{2}\sqrt{2z_3 - z_2} \pm \sqrt{3z_3}}{(\sqrt{2z_3} + \sqrt{z_2})(\sqrt{z_3} + \sqrt{2z_2})}. \end{aligned}$$

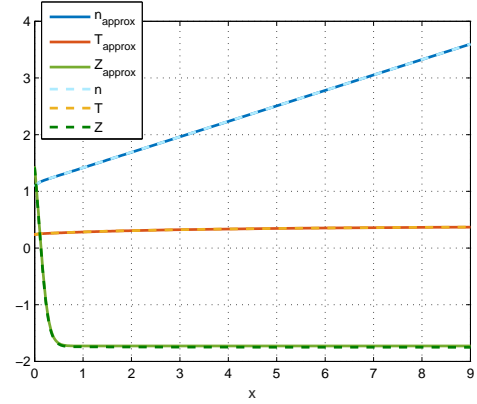
The approximation for \tilde{Z} in (A.3) can now be substituted back in (4.10) to find \tilde{n} . With the solution for \tilde{n} the solution for \tilde{T} can be computed by (4.11).

Figure A.1 shows to approximations computed by the method above. The approximation compared to solution steady-states of the finite difference approximation for $N = 100$. At the standard parameter values in Table 4.1 with $b = -2.5$, equation (4.13) possesses three solutions for Z_0 , namely

$$Z_{01} = -1.5769 \dots \quad Z_{02} = 0.1594 \dots \quad Z_{03} = 1.4227 \dots$$



(a) L-mode profile



(b) H-mode profile

Figure A.1: Analytic approximation of two steady-state profiles at $b = -2.5$

The three roots of (A.2) are

$$Z_L = -1.4991 \dots \quad Z_2 = -0.1715 \dots \quad Z_3 = 2.1956 \dots$$

In Figure A.1a we use the approximation $\tilde{Z} \equiv Z_L$ and the approximation in Figure A.1b is constructed using (A.3).

Appendix B

Discretization

B.1 Finite Difference Formulas

For the endpoints of the grid x_0 and X_N different finite difference formulas apply [13].

$$\frac{\partial n_0}{\partial x} = \varphi_0^{-1} n_0 + \varphi_0^0 n_1 + \varphi_0^1 n_2$$

$$\frac{\partial^2 n_0}{\partial x^2} = \psi_0^{-1} n_0 + \psi_0^0 n_1 + \psi_0^1 n_2$$

$$\frac{\partial n_N}{\partial x} = \varphi_N^{-1} n_{N-2} + \varphi_N^0 n_{N-1} + \varphi_N^1 n_N$$

$$\frac{\partial^2 n_N}{\partial x^2} = \psi_N^{-1} n_{N-2} + \psi_N^0 n_{N-1} + \psi_N^1 n_N$$

It turns out that the expressions for $\psi_0^k = \psi_1^k$ and $\psi_N^k = \psi_{N-1}^k$. The expressions for φ_0^k and φ_N^k are

$$\begin{aligned} \varphi_0^{-1} &= \frac{2h_0 + h_1}{h_0(h_0 + h_1)} & \varphi_0^0 &= -\frac{h_0 + h_1}{h_0 h_1} & \varphi_0^1 &= \frac{h_0}{h_1(h_0 + h_1)} \\ \varphi_N^{-1} &= \frac{h_N}{h_{N-1}(h_N + h_{N-1})} & \varphi_N^0 &= -\frac{h_N + h_{N-1}}{h_N h_{N-1}} & \varphi_N^1 &= \frac{2h_N + h_{N-1}}{h_N(h_N + h_{N-1})} \end{aligned}$$

With the values at the boundary can be solved. The values of Z_0 and Z_N are obtained by solving

$$\frac{\partial^2 Z_0}{\partial x^2} = 0 \quad \frac{\partial Z_N}{\partial x} = 0.$$

With these the values for Z_0 and Z_N the following equations can be solved for n_0, T_0, n_N and T_N

$$\frac{\partial n_1}{\partial x} = \frac{n_1}{\lambda_n} \quad \frac{\partial T_1}{\partial x} = \frac{T_1}{\lambda_T}$$

$$\frac{\partial n_N}{\partial x} = -\frac{\Gamma_\infty}{D(Z_N)} \quad \chi(Z_N) n_N \frac{\partial T_N}{\partial x} = -\frac{\Gamma_\infty T_N}{\gamma - 1} - q_\infty$$

With the values in the boundary the RHS of the following equations can be computed,

$$\begin{aligned}
\frac{\partial n_i}{\partial t} &= D(Z_i) \frac{\partial^2 n_i}{\partial x^2} + \frac{\partial D}{\partial Z} \Big|_{Z=Z_i} \frac{\partial Z_i}{\partial x} \frac{\partial n_i}{\partial x}, \\
\frac{\partial U_i}{\partial t} &= \frac{\partial \chi}{\partial Z} \Big|_{Z=Z_i} \frac{\partial Z_i}{\partial x} n_i \frac{\partial T_i}{\partial x} + \chi(Z_i) \left(\frac{\partial n_i}{\partial x} \frac{\partial T_i}{\partial x} + n_i \frac{\partial^2 T}{\partial x^2} \right) \\
&\quad + \frac{1}{\gamma - 1} \frac{\partial D}{\partial Z} \Big|_{Z=Z_i} \frac{\partial Z_i}{\partial x} T_i \frac{\partial n_i}{\partial x} + \frac{D(Z_i)}{\gamma - 1} \left(\frac{\partial T_i}{\partial x} \frac{\partial n_i}{\partial x} + T_i \frac{\partial^2 n_i}{\partial x^2} \right), \\
\varepsilon \frac{\partial Z_i}{\partial t} &= \mu \frac{\partial^2 Z_i}{\partial x^2} + c_n \frac{T_i}{n_i^2} \frac{\partial n_i}{\partial x} + \frac{c_T}{n_i} \frac{\partial T_i}{\partial x} + G(Z_i).
\end{aligned}$$

B.2 Finite Volume Formulas

The formulas for the Finite Volume discretization become

$$\begin{aligned}
\frac{\partial}{\partial t} \bar{n}_i &= -\frac{\Gamma_i - \Gamma_{i-1}}{h_i}, \\
\frac{\partial}{\partial t} \bar{u}_i &= -\frac{q_i - q_{i-1}}{h_i}, \\
\varepsilon \frac{\partial}{\partial t} Z_i &= \mu \frac{\partial^2 Z_i}{\partial x^2} + (\gamma - 1) c_n \frac{\frac{\partial U_i^{tot}}{\partial x}}{\left(\frac{\partial n_i^{tot}}{\partial x} \right)^3} \frac{\partial^2 n_i^{tot}}{\partial x^2} + \frac{(\gamma - 1) c_T}{\frac{\partial n_i^{tot}}{\partial x}} \frac{\partial}{\partial x} \left(\frac{\frac{\partial U_i^{tot}}{\partial x}}{\frac{\partial n_i^{tot}}{\partial x}} \right) + G(Z_i),
\end{aligned}$$

where

$$\begin{aligned}
\Gamma_i &:= \begin{cases} -\frac{D(Z_0)}{\lambda_n} \frac{\partial n_0^{tot}}{\partial x} & \text{for } i = 0 \\ -D(Z_i) \frac{\partial^2 n_i^{tot}}{\partial x^2} & \text{for } 1 \leq i \leq N - 1 \\ \Gamma_\infty & \text{for } i = N \end{cases}, \\
q_i &:= \begin{cases} -(\gamma - 1) \frac{\chi(Z_0)}{\lambda_T} \frac{\partial U_0^{tot}}{\partial x} - \frac{D(Z_0)}{\lambda_n} \frac{\partial U_0^{tot}}{\partial x} & \text{for } i = 0 \\ -(\gamma - 1) \chi(Z_i) \frac{\partial n_i^{tot}}{\partial x} \frac{\partial^2}{\partial x^2} \left(\frac{U_i^{tot}}{n_i^{tot}} \right) + \frac{\frac{\partial U_i^{tot}}{\partial x}}{\frac{\partial n_i^{tot}}{\partial x}} \Gamma_i & \text{for } 1 \leq i \leq N - 1 \\ q_\infty & \text{for } i = N \end{cases}.
\end{aligned}$$

The values for Z_0 and Z_N are computed in the same way as for the FDM.

B.3 Leading terms in the local error

In this section the leading terms in the local error $R_n^{(1)}(i)$ and $R_n^{(2)}(i)$ in (5.14) will be determined.

First introduce the points

$$\tilde{x}_i = x_i + \frac{1}{3}(h_{i+1} - h_i). \quad (\text{B.1})$$

Now the error in the gridpoints \tilde{x}_i is quadratic [21] [13],

$$\left. \frac{\partial n}{\partial x} \right|_{x=\tilde{x}_i} = \frac{\partial n_i}{\partial x} + \tilde{R}_n^{(1)}(i), \quad (\text{B.2})$$

$$\left. \frac{\partial^2 n}{\partial x^2} \right|_{x=\tilde{x}_i} = \frac{\partial^2 n_i}{\partial x^2} + \tilde{R}_n^{(2)}(i), \quad (\text{B.3})$$

where

$$\begin{aligned} \tilde{R}_n^{(1)}(i) &= \frac{1}{18} \left. \frac{\partial^3 n}{\partial x^3} \right|_{x=\tilde{x}_i} (h_i^2 + h_i h_{i+1} + h_{i+1}^2) + O(h^3), \\ \tilde{R}_n^{(2)}(i) &= \frac{1}{36} \left. \frac{\partial^4 n}{\partial x^4} \right|_{x=\tilde{x}_i} (h_i^2 + h_i h_{i+1} + h_{i+1}^2) + O(h^3). \end{aligned}$$

A second error source is the difference between x_i and \tilde{x}_i . This leads to errors $\hat{R}_n^{(1)}(i)$ and $\hat{R}_n^{(2)}(i)$,

$$\begin{aligned} \hat{R}_n^{(1)}(i) &= \frac{1}{3} \left. \frac{\partial^2 n}{\partial x^2} \right|_{x=\tilde{x}_i} (h_{i+1} - h_i) + O((h_{i+1} - h_i)^2), \\ \hat{R}_n^{(2)}(i) &= \frac{1}{3} \left. \frac{\partial^3 n}{\partial x^3} \right|_{x=\tilde{x}_i} (h_{i+1} - h_i) + O((h_{i+1} - h_i)^2). \end{aligned}$$

Now the total error becomes

$$\begin{aligned} R_n^{(1)}(i) &= \tilde{R}_n^{(1)}(i) + \hat{R}_n^{(1)}(i), \\ R_n^{(2)}(i) &= \tilde{R}_n^{(2)}(i) + \hat{R}_n^{(2)}(i). \end{aligned}$$

B.4 Adaptive grid

The grid will be distributed according to the approach used in CONTENT [21]. The criterion used in this approach is that the error in the first derivative is uniformly distributed. To simplify the notation $y(x, t)$ is introduced as

$$y(x, t) := \begin{pmatrix} n(x, t) \\ U(x, t) \\ Z(x, t) \end{pmatrix}. \quad (\text{B.4})$$

It will be assumed that the grid is so smooth that $h_{i+1} - h_i = O(h^3)$, so that

$$R(\tilde{x}_i) = \frac{1}{18} \left. \frac{\partial^3 y}{\partial x^3} \right|_{\tilde{x}_i} (h_i^2 + h_i h_{i+1} + h_{i+1}^2) + O(h^3) \quad (\text{B.5})$$

By taking the norm and the square root on both sides it follows that $\|R\|^{\frac{1}{2}}$ is (approximately) constant when

$$S(x_i)(x_i - x_{i-1}) = C, \quad (\text{B.6})$$

where C is a positive constant and $S(x)$ is defined as

$$S(x) = \begin{cases} \left\| \frac{\partial^3 y}{\partial x^3}(x) \right\|^{\frac{1}{2}} & \left\| \frac{\partial^3 y}{\partial x^3}(x) \right\|^{\frac{1}{2}} \geq \epsilon \\ \epsilon & \left\| \frac{\partial^3 y}{\partial x^3}(x) \right\|^{\frac{1}{2}} < \epsilon \end{cases}. \quad (\text{B.7})$$

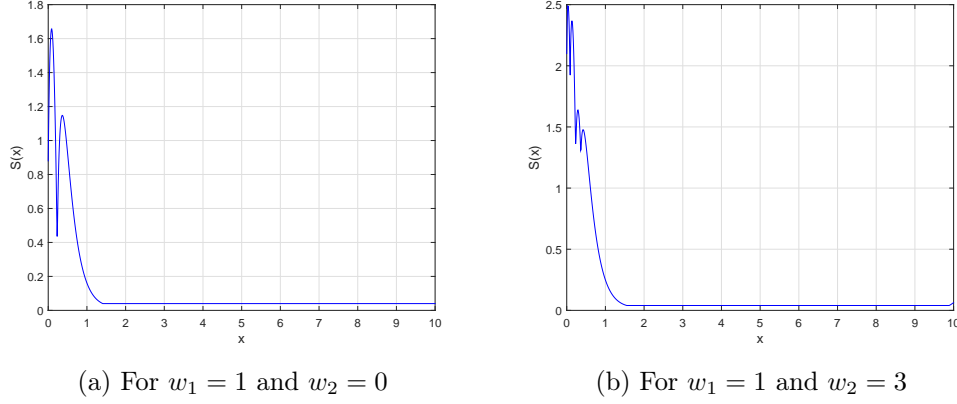


Figure B.1: The function $S(x)$ for different weights w_1 and w_2

By introducing the minimum value ϵ for $S(x)$ it is assured that the grid will not be too unevenly distributed due to the large peak values in $\left\| \frac{\partial^3 y}{\partial x^3}(x) \right\|$.

The criterion (B.6) is implemented as

$$\int_{x_{i-1}}^{x_i} S(x) dx = C = \frac{1}{N} \int_0^L S(x) dx. \quad (\text{B.8})$$

Since $S(x) \geq \epsilon > 0$ it follows that it will always hold that $x_i > x_{i+1}$. Equation (B.8) leads to the following system of $N - 1$ nonlinear equations

$$\begin{aligned} S(x_1)x_1 - S(x_2)(x_2 - x_1) &= 0 \\ S(x_i)(x_i - x_{i-1}) - S(x_{i+1})(x_{i+1} - x_i) &= 0 \\ S(x_{N-1})(x_{N-1} - x_{N-2}) - S(L)(L - x_{N-1}) &= 0 \end{aligned} \quad i = 2, 3, \dots, N - 2, \quad (\text{B.9})$$

that can be solved for x_i for $i = 1, 2, \dots, N - 1$. The endpoints $x_0 = 0$ and $x_N = L$ complete the grid.

The method above can be slightly generalized by also considering the error in the second derivative as

$$R(\tilde{x}_i) = \frac{1}{36} \frac{\partial^4 y}{\partial x^4}(\tilde{x}_i) (h_i^2 + h_i h_{i+1} + h_{i+1}^2) + O(h^3).$$

Based on this result the function $S(x)$ would then be defined as

$$S(x) = w_1 \frac{1}{6} \left\| \frac{\partial^3 y}{\partial x^3}(x) \right\|^{\frac{1}{2}} + w_2 \frac{1}{9} \left\| \frac{\partial^4 y}{\partial x^4}(x) \right\|^{\frac{1}{2}},$$

where w_1 and w_2 are weights.

The derivatives of y are obtained from the profiles in Figure 5.2. From these derivatives $S(x)$ can be computed for different weights w_1 and w_2 . For the weights $w_1 = 1$ and $w_2 = 3$ the function $S(x)$ is much smoother than for $w_1 = 1$ and $w_2 = 0$, as can be seen from Figure B.1.

For the profile $w_1 = 1$ and $w_2 = 0$ the grid x_i can be computed by solving (B.9). The location of the Hopf-bifurcation is not determined by continuation but by direct simulation. The results are collected in Table B.1. Note that the results are worse then for Θ_N^2 .

Table B.1: Location of the Hopf-bifurcation for the adaptive grids

N	$w_1 = 1$ and $w_2 = 0$	$w_1 = 1$ and $w_2 = 3$
30	-1.04	-1.02
50	-0.92	-0.92
100	-0.86	-0.87

Appendix C

Convergence of the spatial discretization

In this appendix it is established that the spatial discretization is fully converged for the results in Section 6.1.

C.1 1-parameter continuation

The curves in Figure 6.1, Figure 6.3, Figure 6.5 and Figure 6.7 have been computed for $N = 15$, $N = 30$, $N = 50$ and $N = 100$ meshpoints. The resulting curves are shown in Figure C.1, Figure C.2, Figure C.3 and Figure C.4. Note that the lines for $N = 30$, $N = 50$ and $N = 100$ can hardly be distinguished. For $N = 15$ some drift in q_∞ can be observed.

Also the position of the critical points and the normal form coefficients in the different figures are given in Table C.1, Table C.2 and Table C.3. It should be noted that the normal form coefficients decrease proportional to $1/N$ when the number of meshpoints N is increased. This is a consequence of the normalization of the eigenvectors.

C.2 2-parameter continuation

Also the fold and Hopf curves in Figure 6.9, Figure 6.11 and Figure 6.12 have been computed for $N = 15$, $N = 30$ and $N = 50$. Because of the convergence that was observed in the 1-parameter continuation, these curves have not been computed for $N = 100$. The resulting curves are shown in Figure C.9 to Figure C.8. The critical points and their normal form coefficients are shown in Table C.4, Table C.5 and Table C.6.

C.3 3-parameter continuation

The convergence of the spatial discretization for the BT curve in Figure 6.14 is shown in Figure C.12. Figure C.13 and Figure C.14 show that the normal form coefficients also vanish simultaneously for lower N . Furthermore it should be mentioned that the points where a_2 and b_2 vanish were located independently. Table C.7 shows the location of both points. It can be observed that their difference is within the specified tolerance of 10^{-5} . Here it should also be noted that accuracy in the computation of a_2 and b_2 is limited due to the computation of the multilinear forms A and B by finite differences. Also the normal form coefficients a_3 and b_3 are given in Table C.7.

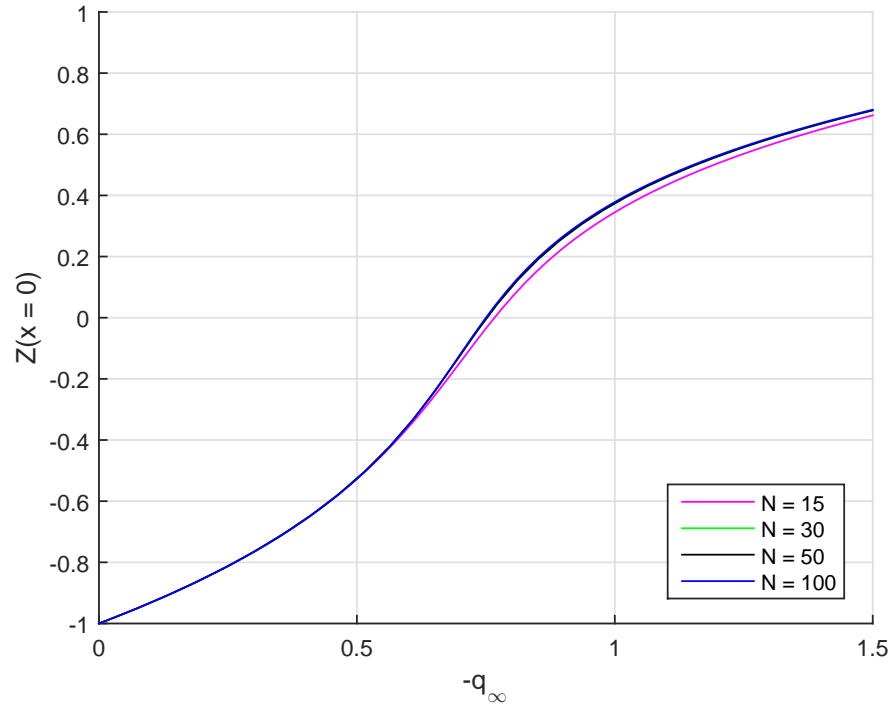


Figure C.1: Convergence in equilibrium continuation in q_∞ at $b = 0$ (see Figure 6.1)

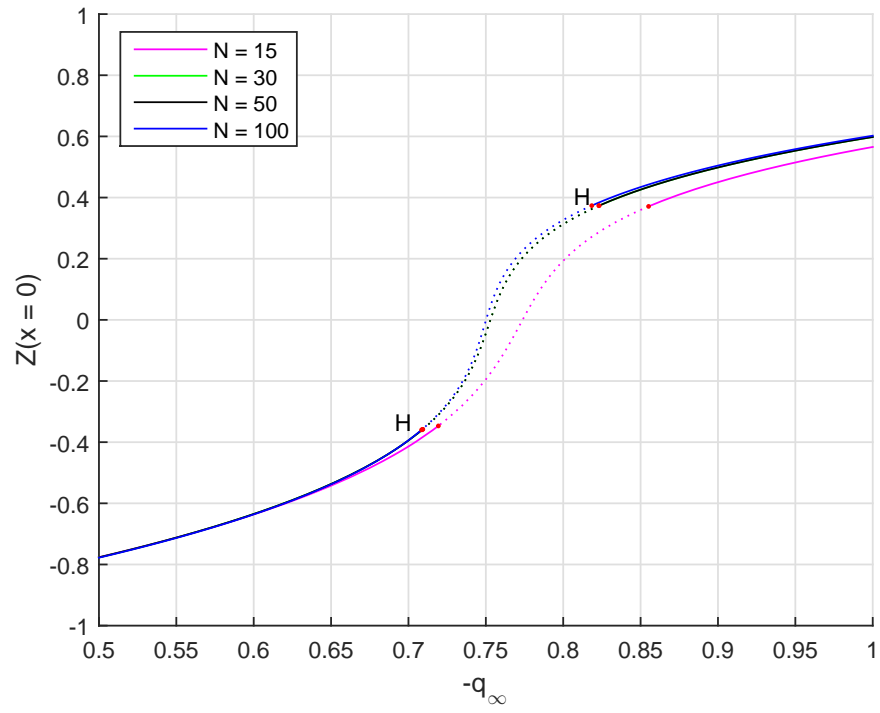


Figure C.2: Convergence in equilibrium continuation in q_∞ at $b = -0.5$ (see Figure 6.3)

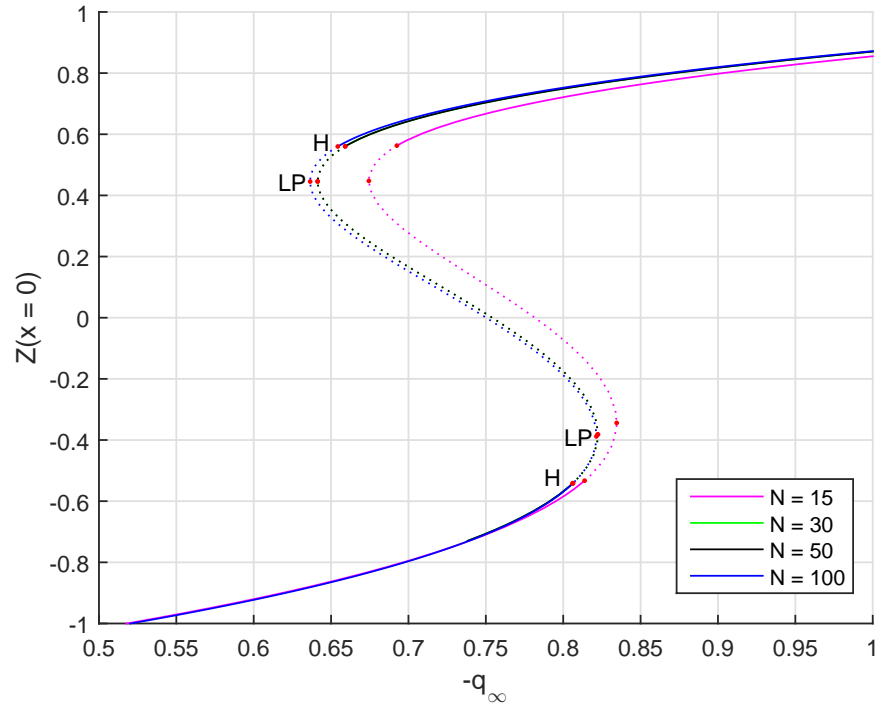


Figure C.3: Convergence in equilibrium continuation in q_∞ at $b = -1$ (see Figure 6.5)

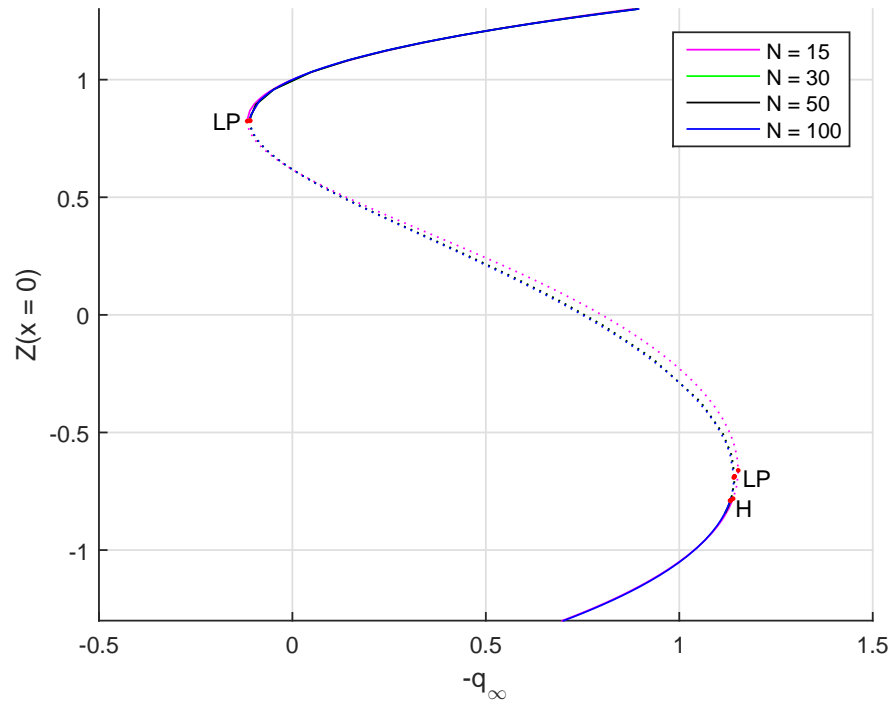


Figure C.4: Convergence in equilibrium continuation in q_∞ at $b = -1$ (see Figure 6.7)

Table C.1: Convergence in critical points in Figure 6.3

N	PT	q_∞	Normal form coefficient
15	H	-0.8551625	$l_1 = -28.76447$
	H	-0.7193132	$l_1 = -30.03397$
30	H	-0.8231123	$l_1 = -13.73104$
	H	-0.7092233	$l_1 = -14.81403$
50	H	-0.8193814	$l_1 = -8.010864$
	H	-0.7085045	$l_1 = -8.675157$
100	H	-0.8184383	$l_1 = -3.977744$
	H	-0.7084780	$l_1 = -4.276498$

Table C.2: Convergence in critical points in Figure 6.5

N	PT	q_∞	Normal form coefficient
15	H	-0.6925140	$l_1 = -66.18729$
	LP	-0.6744180	$a = 0.08264964$
	LP	-0.8345693	$a = 0.09896964$
	H	-0.8138324	$l_1 = -50.20281$
30	H	-0.6591274	$l_1 = -30.35959$
	LP	-0.6413172	$a = 0.06074195$
	LP	-0.8223738	$a = 0.08707586$
	H	-0.8131855	$l_1 = -24.59994$
50	H	-0.6552750	$l_1 = -17.66135$
	LP	-0.6374559	$a = -0.04724536$
	LP	-0.8214824	$a = -0.06852738$
	H	-0.8059749	$l_1 = -14.32953$
100	H	-0.6543287	$l_1 = -8.557108$
	LP	-0.6364789	$a = -0.03347224$
	LP	-0.8214211	$a = -0.04705916$
	H	-0.8061102	$l_1 = -6.944593$

Table C.3: Convergence in critical points in Figure 6.7

N	PT	q_∞	Normal form coefficient
15	LP	+0.1167329	$a = -1.467696$
	LP	-1.152332	$a = -0.2198989$
	H	-1.139124	$l_1 = -87.09703$
30	LP	+0.1100951	$a = 0.8814588$
	LP	-1.142811	$a = -0.1839610$
	H	-1.132585	$l_1 = -42.63467$
50	LP	+0.1094085	$a = -0.6623698$
	LP	-1.142596	$a = -0.1439477$
	H	-1.132763	$l_1 = -24.96721$
100	LP	+0.1092571	$a = -0.4613539$
	LP	-1.142851	$a = -0.1003235$
	H	-1.133148	$l_1 = -11.83338$

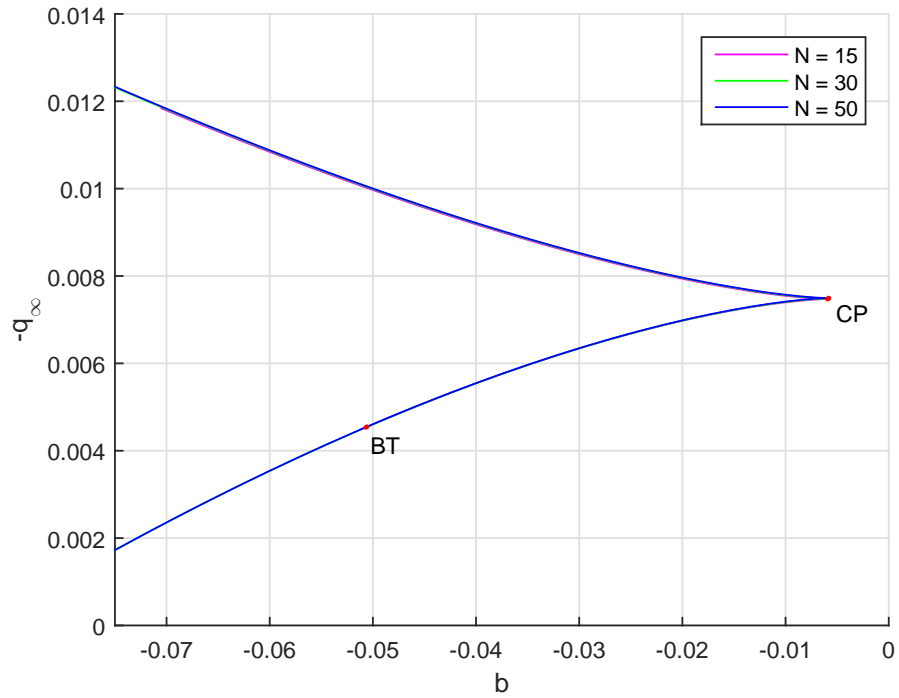


Figure C.5: Convergence in fold continuation at $a = -0.01$ (see Figure 6.11)

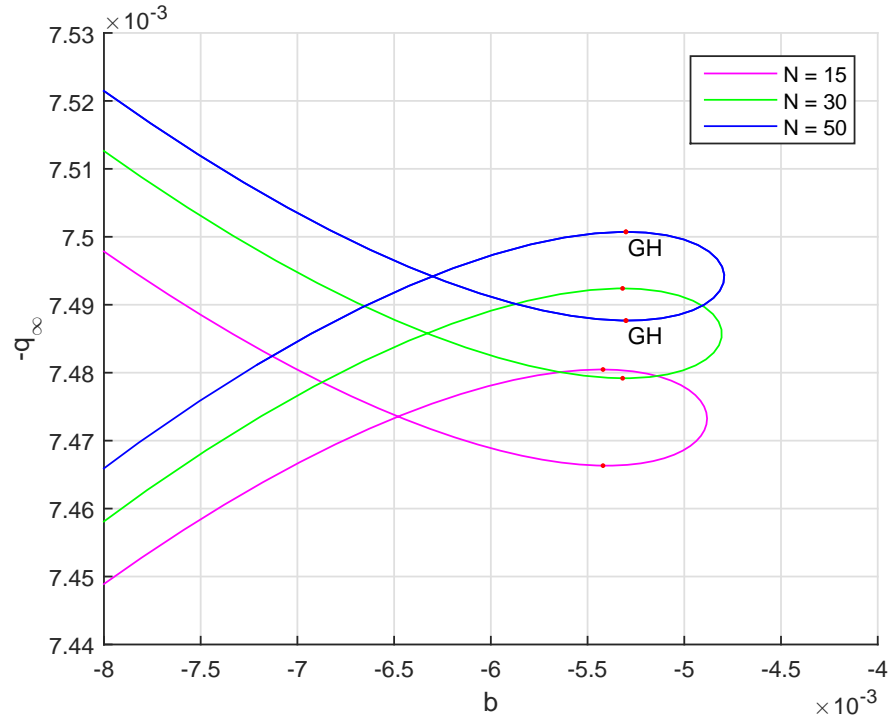


Figure C.6: Convergence in fold continuation at $a = -0.01$ (see Figure 6.11)

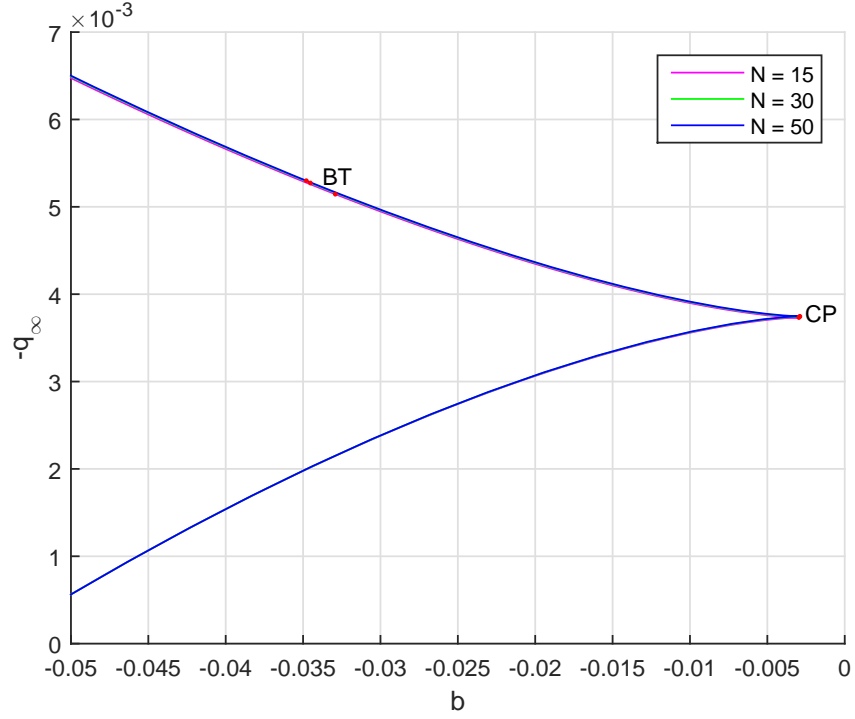


Figure C.7: Convergence in fold continuation at $a = -0.005$ (see Figure 6.12)

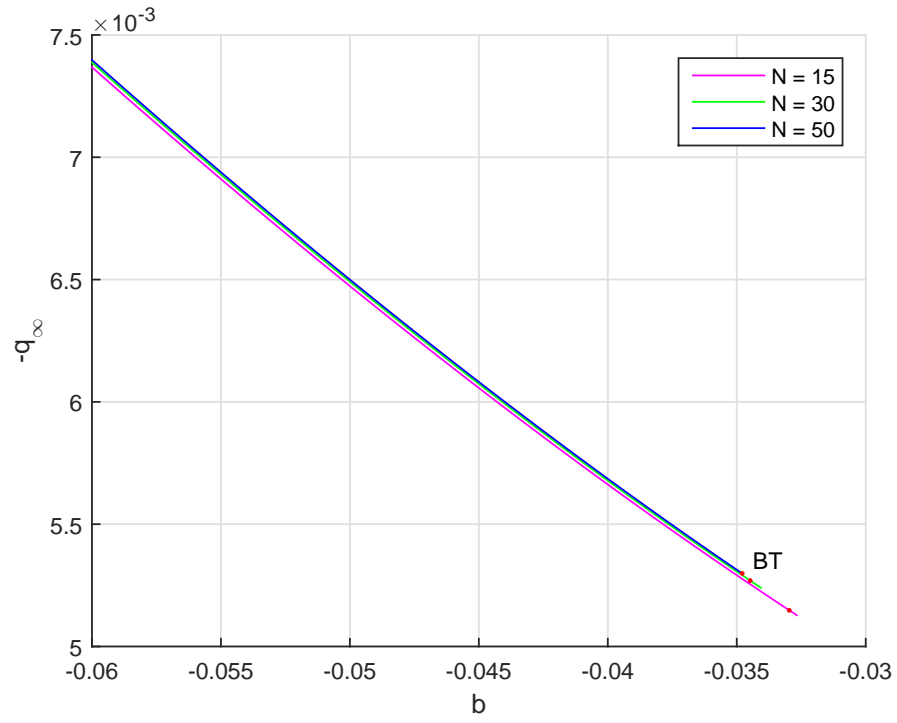


Figure C.8: Convergence in Hopf continuation at $a = -0.005$ (see Figure 6.12)

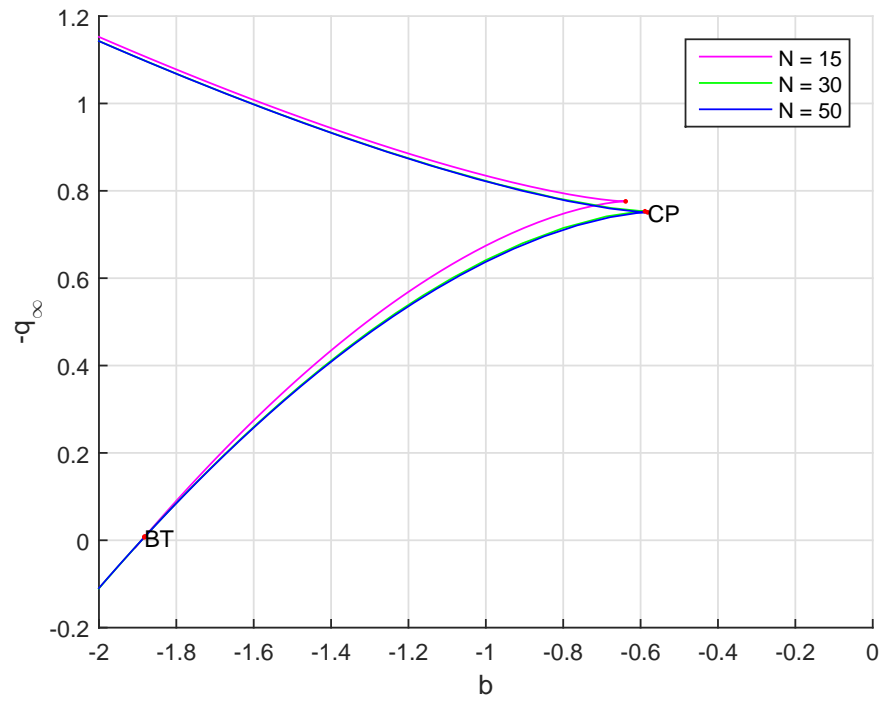


Figure C.9: Convergence in fold continuation at $a = -1$ (see Figure 6.9)

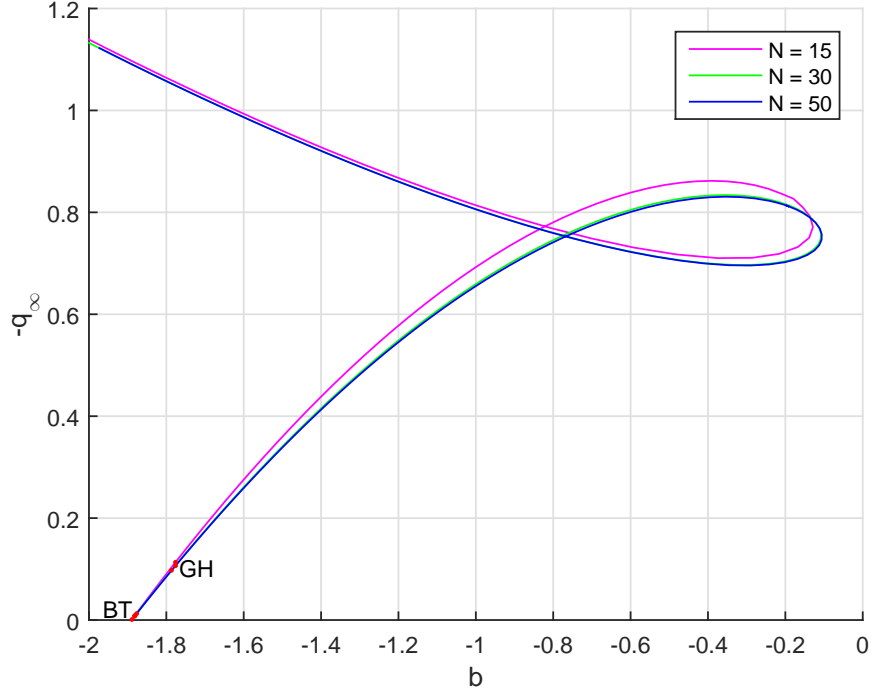


Figure C.10: Convergence in Hopf continuation at $a = -1$ (see Figure 6.9)

Table C.4: Convergence in critical points in Figure 6.9

N	PT	q_∞	b	Normal form coefficient(s)
15	CP	-0.7758755	-0.6386257	$c = 0.02743175$
	BT	-0.008538193	-1.881570	$a_2 = 0.7971415 \quad b_2 = 40.07014$
	GH	-0.1133626	-1.776343	$l_2 = 7.208383 \cdot 10^6$
30	CP	-0.7531555	-0.5886263	$c = 0.01581755$
	BT	-0.007375955	-1.882275	$a_2 = -0.5316517 \quad b_2 = -26.49723$
	GH	-0.09759042	-1.786691	$l_2 = 1.481198 \cdot 10^6$
50	CP	-0.7507218	-0.5816532	$c = 0.009706415$
	BT	-0.007235221	-1.882373	$a_2 = 0.4059355 \quad b_2 = 20.20398$
	GH	-0.1065882	-1.776139	$l_2 = \text{N.A.}$

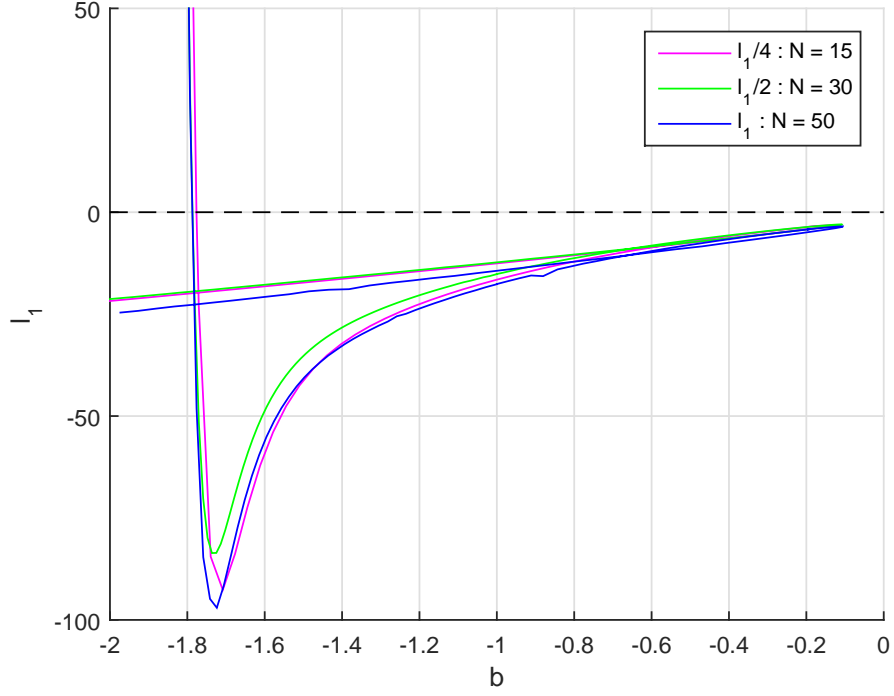


Figure C.11: Convergence in first Lyapunov coefficient along the Hopf curve at $a = -1$ (see Figure 6.10)

Table C.5: Convergence in critical points in Figure 6.11

N	PT	q_∞	b	Normal form coefficient(s)
15	CP	-0.007473152	-0.005946932	$c = 4.952808$
	BT	-0.004502586	-0.05103886	$a_2 = -0.1009003 \quad b_2 = -5.225832$
	GH	-0.007466320	-0.005420168	$l_2 = -1484.474$
	GH	-0.007480471	-0.005420125	$l_2 = -1052.586$
30	CP	-0.007485484	-0.005822102	$c = 2.509074$
	BT	-0.004536370	-0.05066247	$a_2 = 0.07010060 \quad b_2 = 3.635719$
	GH	-0.007479183	-0.005318740	$l_2 = -326.7109$
	GH	-0.007492407	-0.005318975	$l_2 = -256.6530$
50	CP	-0.007493877	-0.005800303	$c = 1.496973$
	BT	-0.004547862	-0.05057939	$a_2 = -0.05383250 \quad b_2 = -2.793096$
	GH	-0.007487669	-0.005301462	$l_2 = -112.0678$
	GH	-0.007500729	-0.005301872	$l_2 = -92.44092$

Table C.6: Convergence in critical points in Figure 6.12

N	PT	q_∞	b	Normal form coefficient(s)
15	CP	-0.003732647	-0.002963097	$c = -14.37414$
	BT	-0.005144738	-0.03291809	$a_2 = 0.09703511 \quad b_2 = 4.872035$
30	CP	-0.003741936	-0.002909136	$c = -6.553103$
	BT	-0.005272808	-0.03452668	$a_2 = -0.06944777 \quad b_2 = -3.491588$
50	CP	-0.003746671	-0.002899559	$c = -3.831075$
	BT	-0.005298753	-0.03479115	$a_2 = 0.05361886 \quad b_2 = 2.695805$

Table C.7: Convergence in located degenerate Bogdanov-Takens points

N	PT	$q_\infty \cdot 10^3$	$b \cdot 10^3$	$a \cdot 10^3$	normal form coefficients
15	BT $_{b_2=0}$	-4.597644	-3.652584	-6.156978	$a_3 = -0.1022540$
	BT $_{a_2=0}$	-4.600210	-3.654456	-6.160398	$b_3 = -7.959728$
30	BT $_{b_2=0}$	-4.680158	-3.639375	-6.253270	$a_3 = -0.04961665$
	BT $_{a_2=0}$	-4.681846	-3.640405	-6.255526	$b_3 = -3.873779$
50	BT $_{b_2=0}$	-4.700368	-3.638099	-6.272594	$a_3 = -0.02935345$
	BT $_{a_2=0}$	-4.702027	-3.639069	-6.274808	$b_3 = -2.292365$

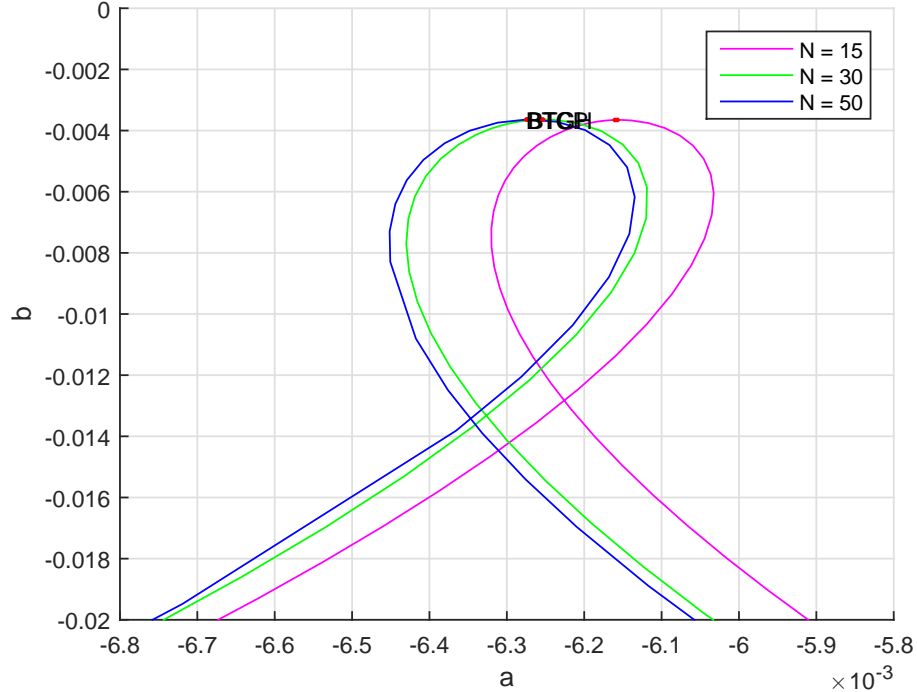


Figure C.12: Convergence in the computed BT-curve.

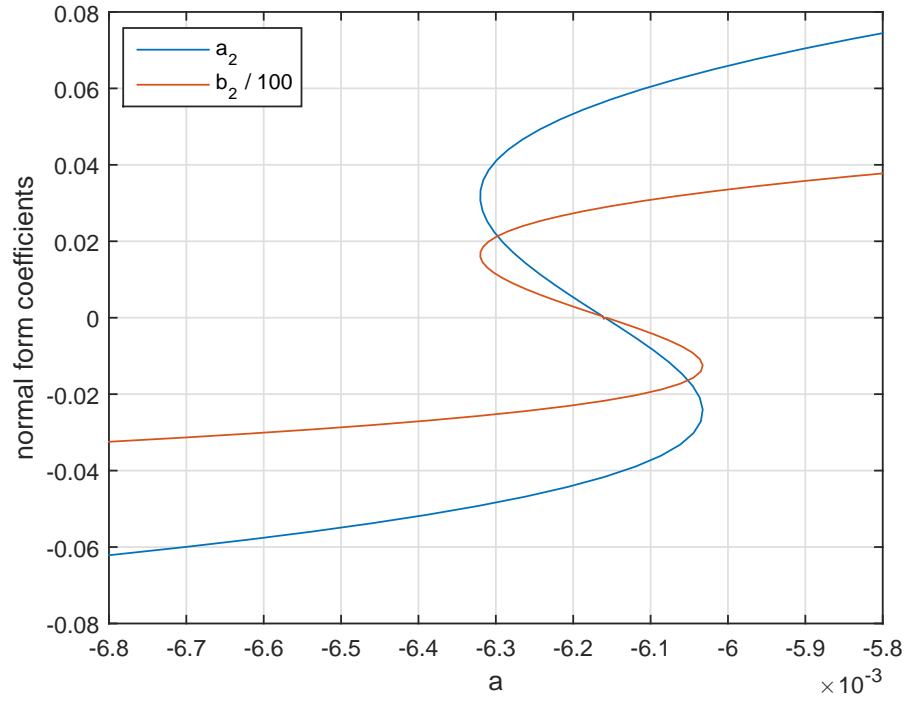


Figure C.13: Normal form coefficients a_2 and b_2 for the BT-curve at $N = 15$.

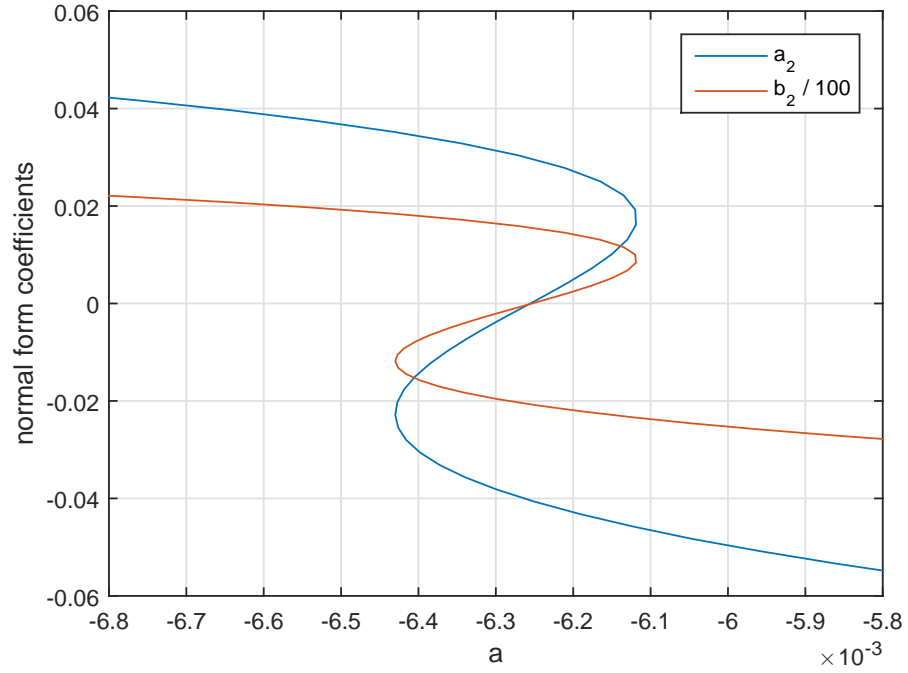


Figure C.14: Normal form coefficients a_2 and b_2 for the BT-curve at $N = 30$.

Bibliography

- [1] V.I. Arnold. *Geometrical Methods in the Theory of Ordinary Differential Equations*, volume 250 of *Grundlehren der mathematischen Wissenschaften*. Springer, 1988.
- [2] W.J. Beyn, A. Champneys, E. Doedel, W. Govaerts, Yu. A. Kuznetsov, B. Sandstede, et al. Numerical continuation, and computation of normal forms. In *Handbook of Dynamical Systems*, 1999.
- [3] D. Bindel, J. Demmel, and M. Friedman. Continuation of invariant subspaces in large bifurcation problems. *SIAM Journal on Scientific Computing*, 30(2):637–656, 2008.
- [4] D. Bindel, M. Friedman, W. Govaerts, J. Hughes, and Yu. A. Kuznetsov. Numerical computation of bifurcations in large equilibrium systems in Matlab. *Journal of Computational and Applied Mathematics*, 261:232–248, 2014.
- [5] H. de Blank. L–h bifurcation structure of reactive-diffusive transport in tokamak plasma. *Notes*, 2015.
- [6] A. Dhooge, W. Govaerts, and Yu. A. Kuznetsov. Matcont: a Matlab package for numerical bifurcation analysis of ODEs. *ACM TOMS*, 29(2):141–164, 2003.
- [7] A. Dhooge, W. Govaerts, Yu. A. Kuznetsov, W. Mestrom, and A.M. Riet. Cl_matcont: a continuation toolbox in Matlab. In *Proceedings of the 2003 ACM Symposium on Applied Computing*, pages 161–166. ACM, 2003.
- [8] J.J. Duistermaat and J.A.C. Kolk. *Multidimensional real analysis I: Differentiation*, volume 86. Cambridge University Press, 2004.
- [9] F. Dumortier, R. Roussarie, and J. Sotomayor. Generic 3-parameter families of vector fields on the plane, unfolding a singularity with nilpotent linear part. the cusp case of codimension 3. *Ergodic Theory and Dynamical Systems*, 7(03):375–413, 1987.
- [10] F. Dumortier, R. Roussarie, J. Sotomayor, and H. Zoladek. *Bifurcations of Planar Vector Fields: Nilpotent Singularities and Abelian Integrals*. Lecture Notes in Mathematics. Springer Berlin Heidelberg, 1991.
- [11] P. Glendinning. Global bifurcations in flows. In *New Directions in Dynamical Systems*, pages 120–149. Cambridge University Press, 1988. Cambridge Books Online.
- [12] W. Govaerts, Yu. A. Kuznetsov, and B. Sijnave. Continuation of codimension-2 equilibrium bifurcations in CONTENT. In *Numerical Methods for Bifurcation Problems and large-scale Dynamical Systems*, pages 163–184. Springer, 2000.

- [13] W.J.F. Govaerts. *Numerical Methods for Bifurcations of Dynamical Equilibria*. SIAM, 2000.
- [14] J. Guckenheimer and Yu. A. Kuznetsov. Bautin bifurcation. *Scholarpedia*, 2(5):1853, 2007. revision nr. 91035.
- [15] J. Guckenheimer and Yu. A. Kuznetsov. Cusp bifurcation. *Scholarpedia*, 2(4):1852, 2007. revision nr. 91186.
- [16] J. Hyman, R. Knapp, and J. Scovel. High order finite volume approximations of differential operators on nonuniform grids. *Physica D*, 60:112 – 138, 1992.
- [17] S.I. Itoh, K. Itoh, A. Fukuyama, and Y. Miura. Edge localized mode activity as a limit cycle in tokamak plasmas. *Phys. Rev. Lett.*, 67:2485–2488, Oct 1991.
- [18] A.I. Khibnik, B. Krauskopf, and C. Rousseau. Global study of a family of cubic Liénard equations. *Nonlinearity*, 11(6):1505, 1998.
- [19] Yu. A. Kuznetsov. *Elements of Applied Bifurcation Theory*, volume 112 of *Applied Mathematical Sciences*. Springer, 1995.
- [20] Yu. A. Kuznetsov. Practical computation of normal forms on center manifolds at degenerate Bogdanov-Takens bifurcations. *International Journal of Bifurcation and Chaos*, 15(11):3535–3546, 2005.
- [21] Yu. A. Kuznetsov, V. Levitin, and A. Skovoroda. Continuation of stationary solutions to evolution problems in content. Technical Report AM-R9611, Centrum voor Wiskunde en Informatica, 1996.
- [22] S. Paquay. Studying bifurcations in proposed l-h transition models using bifurcator. Master's thesis, Eindhoven University of Technology, 2012.
- [23] C. Robinson. *Dynamical systems : Stability, Symbolic Dynamics, and Chaos*. Studies in advanced mathematics. Boca Raton, Fla. CRC Press, 1999.
- [24] U. Stroth, J. Adamek, L. Aho-Mantila, S. Äkäslompolo, C. Amdor, C. Angioni, M. Balden, S. Bardin, L. Barrera Orte, K. Behler, et al. Overview of asdex upgrade results. *Nuclear Fusion*, 53(10):104003, 2013.
- [25] W. Weymiens. *Bifurcation theory of the L-H transition*. PhD thesis, Eindhoven University of Technology, 2014.
- [26] V. de Witte, W. Govaerts, Yu. A. Kuznetsov, and M. Friedman. Interactive initialization and continuation of homoclinic and heteroclinic orbits in matlab. *ACM TOMS*, 38(3):34, 2012.
- [27] H. Zohm. Dynamic behavior of the l-h transition. *Phys. Rev. Lett.*, 72:222–225, Jan 1994.